Raman light scattering study on phonon anomalies in unconventional superconductors

DISSERTATION

zur Erlangung des Grades eines Doktors
der Naturwissenschaften

Mathematisch-Naturwissenschaftliche Fakultät
der Eberhard-Karls-Universität zu Tübingen

vorgelegt von
Martin Rahlenbeck (geb. Müller)
aus Mutlangen

2010

Raman light scattering study on phonon anomalies in unconventional superconductors

DISSERTATION

zur Erlangung des Grades eines Doktors
der Naturwissenschaften

Mathematisch-Naturwissenschaftliche Fakultät
der Eberhard-Karls-Universität zu Tübingen

vorgelegt von
Martin Rahlenbeck (geb. Müller)
aus Mutlangen

2010

Tag der mündlichen Prüfung:	07.12.2010
Dekan:	Prof. Dr. W. Rosenstiel
1. Berichterstatter:	Prof. Dr. R. Kleiner
2. Berichterstatter:	Prof. Dr. B. Keimer

In memoriam

Sir C. V. Raman with an apparatus for inelastic light scattering [Jay89].

Abstract

This work presents a series of detailed temperature-dependent Raman light scattering studies on optical phonons in different unconventional high-temperature superconductors. It divides into three main projects.

The first project presents a study on two molecular-beam-epitaxy-grown films of the electron-doped superconductor $La_{2-x}Ce_xCuO_4$ (LCCO) close to optimal doping ($x \sim 0.08$, $T_c = 29$ K and $x \sim 0.1$, $T_c = 27$ K), that had been the basis of prior transport measurements. The main focus of this project was a detailed characterization and microstructural analysis of the films. Based on micro-Raman spectroscopy in combination with X-ray diffraction, energy-dispersive X-ray analysis, and scanning electron microscopy, some of the observed phonon modes can be attributed to micron-sized inclusions of Cu_2O. In the slightly underdoped film ($x \sim 0.08$), both the Cu_2O modes and others that can be assigned to the LCCO matrix show pronounced softening and narrowing upon cooling below $T \sim T_c$. Control measurements on commercial Cu_2O powders and a comparison to prior Raman scattering studies of other high-temperature superconductors motivate the speculation that proximity effects at the LCCO/Cu_2O interface may be responsible for these anomalies. Experiments on the slightly overdoped LCCO film ($x \sim 0.1$) did not reveal comparable phonon anomalies. (The main results of this project are published under *Rahlenbeck et al.*, Eur. Phys. J. B, **75**, 461 (2010).)

The second project presents a study on superconducting and non-superconducting single crystals of the iron pnictides $BaFe_2As_2$, $SrFe_2As_2$, and $R_{1-x}K_xFe_2As_2$ with R = Ba, Sr (hole-doped) and $BaFe_{2-x}Co_xAs_2$ (electron-doped) with different doping levels, respectively. In the undoped and hole-doped samples a pronounced continuous narrowing of the Raman-active Fe and As vibrations upon cooling below the spin-density wave (SDW) transition T_s is observed. This effect is attributed to the opening of a SDW gap. The electron-phonon linewidths inferred from these data greatly exceed the predictions of *ab initio* density-functional calculations without spin polarization, which may imply that local magnetic moments survive well above T_s. A first-order structural transition accompanying the SDW transition induces discontinuous jumps in the phonon

frequencies and anomalously large splittings of the in-plane modes. These anomalies are continuously suppressed for increasing doping concentrations. The corresponding phonon anomalies in the electron-doped samples are in agreement with a splitting of the structural and SDW transitions in temperature. At the superconducting transition temperature T_c subtle phonon anomalies are observed with a behavior qualitatively similar to that in the cuprate superconductors. (The main results of this project are published under *Rahlenbeck et al.*, Phys. Rev. B, **80**, 064509 (2009).)

The third project presents a study on superconducting and non-superconducting single crystals of the iron chalcogenide systems $Fe_{1+y}Te$ and $Fe_{1+y}Se_xTe_{1-x}$ with different concentrations of Se doping and Fe excess. In undoped $Fe_{1.08}Te$ no phonon anomaly is observed at the transition temperature to long-range antiferromagnetic order T_N that is accompanied with a structural phase transition. On the other hand, Se-doped $Fe_{1.05}Se_{0.42}Te_{0.58}$ and $Fe_{1.08}Se_{0.28}Te_{0.72}$ show a pronounced softening in the phonon frequency of the Fe vibration at the onset temperature of short-range incommensurate spin-fluctuations T_{IC} upon cooling, which largely exceeds the amplitude of the phonon anomalies at the structural and SDW phase transitions in the iron pnictides. The pronounced phonon softening in the iron chalcogenides may indicate a strong spin-phonon coupling, induced by the short-range incommensurate spin-fluctuations. Additional contributions due to the presence of Fe excess cannot be excluded.

Contents

Chapter 1

Introduction

Superconductivity is one of the most active fields in physical research and holds a huge potential for future applications. Superconductivity is a macroscopic quantum phenomenon[1], which appears typically at low temperatures, setting in below a critical temperature T_c. The superconducting state is characterized by two main properties. Below T_c the electrical resistance drops to zero, allowing an electrical current to flow without any dissipation. Secondarily, an external magnetic field is expelled totally out of the superconducting material as long as it stays below the critical magnetic field H_c, exhibiting perfect diamagnetism (Meißner effect). The long-term purpose of research on superconductors is to find materials with higher transition temperatures T_c and to achieve a deeper understanding of the underlying physical mechanism. The dream is superconductivity at room temperature, which would enhance the fields of applications tremendously, like e.g. dissipationless transport of current and magnetic levitation.

The superconducting state is a thermodynamical phase, which is formed by pairing of charge carriers to Cooper pairs with integer total spin, acting as superconducting charge carriers. The ingredients for superconductivity are a Fermi sea and an attractive interaction. The essential pairing mechanism can be of diverse origin. The quasi-bosonic Cooper pairs coherently superpose to a macroscopic wave function $\Psi = \Phi_0 \cdot e^{i\varphi}$ with a common phase φ, very similar to a Bose-Einstein condensation of a gas of bosonic atoms. For an elementary excitation out of the superconducting condensate one has to break at least one Cooper pair into two quasi-particles,

[1] The fundamentals of superconductivity can be looked up e.g. in [Buc04, Tin96].

which costs the "pairing energy" 2Δ. Therefore, the superconducting condensate is separated from its elemental excitation spectrum by a superconducting energy gap of 2Δ centered at the Fermi energy E_F. The symmetry of the superconducting gap depends on the underlying pairing mechanism.

The family of superconducting materials is divided into two main groups. In the conventional superconductors, where superconductivity was discovered [Onn11], the Cooper pairs are weakly coupled spin singlets and the superconducting gap is predominantly isotropic (s-wave symmetry). For this class of superconductors the attractive interaction between the charge carriers is mediated by an interaction with the lattice vibrations (phonons). Magnetic interactions are considered as pair-breaking. The family of conventional superconductors comprises various elements and a large number of metal alloys. A fully microscopical picture for conventional superconductors was formulated within the BCS-theory [Bar57], yielding the characteristic relation $2\Delta/k_BT_c \approx 3.5$ (> 3.5 for strong coupling). The maximal transition temperature described by the BCS theory is supposed to be ~ 40 K [Koe04], what is still highly debated. The highest T_c among conventional superconductors was observed in MgB_2 at 39 K [Nag01].

The second main group of superconductors are the so called unconventional superconductors, which split into a large number of subgroups. The essential characteristic of unconventional superconductivity is at least one broken symmetry in addition to the broken gauge invariance (phase φ), e.g. the rotational symmetry of the superconducting gap, $\Delta = \Delta(\vec{k})$, or a predominant non-phononic pairing mechanism. The largest and most studied subgroup of unconventional superconductors are the cuprates, which become superconducting after doping with holes or electrons. Their discovery in 1986 [Bed86] was a breakthrough on the way to higher superconducting transition temperatures, raising the known transition temperatures quickly up to $T_c > 135$ K (see figure 1.1). Due to the much higher transition temperatures compared to the conventional superconductors, the cuprates were called high-temperature superconductors (HTSC).

The cuprates are layered materials[2] with two-dimensional CuO_2 planes as common structural element, serving as the playground for superconductivity. The interlayer regions serve as charge carrier reservoirs. The observation of superconductivity in copper oxides was surprising, because the undoped parent compounds are strongly-correlated antiferromagnetic (AFM) charge transfer insulators [Arm09]. For increasing doping, the

[2] For details about crystal structure and phase diagram see chapter 4.1.

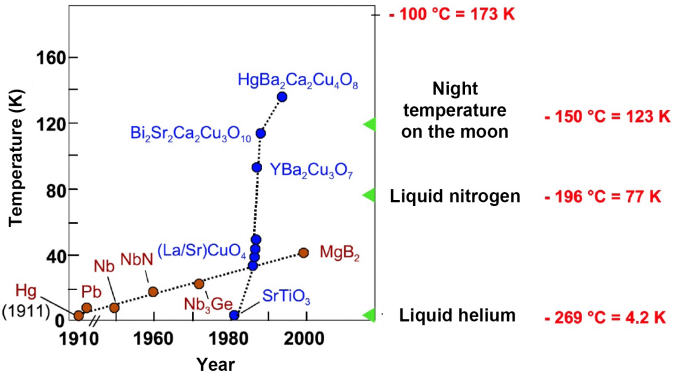

Figure 1.1: Progress in the research for higher superconducting transition temperatures T_c with attention to the cuprate HTSC [Kir96].

AFM order is suppressed and superconductivity can emerge at low temperatures. The mechanism of high temperature superconductivity is not fully understood up to now. However, it was shown that a pure phonon-mediated coupling mechanism cannot explain the high transition temperatures T_c [Wys00]. Motivated by an observation of a magnetic resonance peak in inelastic neutron scattering [RM91], which exclusively appears in the superconducting state, and the proximity to AFM order, a coupling mechanism based on magnetic fluctuations [Sca95] is favored. In agreement with such a scenario, the superconducting gap in the cuprates contains nodes and shows a predominant $d_{x^2-y^2}$-wave symmetry [Tsu00]. Electron-doped cuprate superconductors exhibit substantially lower maximum transition temperatures and a narrower doping range of superconductivity than their hole-doped counterparts. Moreover, the AFM phase appears broader and closer to the superconducting phase. The origin of this asymmetry of the phase diagram is still incompletely understood and highlights the electron-doped cuprates as excellent test systems to study the influence of AFM correlations on superconductivity. However, compared to hole-doping, this class of materials is less studied. As an essential problem, microstructural inhomogeneities and a very complex material physics complicates scientific investigations. The pervasiveness of inclusions and their influence on various physical properties is only beginning to be explored.

At the beginning of 2008, a Japanese group found superconductivity in the iron-based compound LaFeAsOF with $T_c = 26$ K [Kam08], which

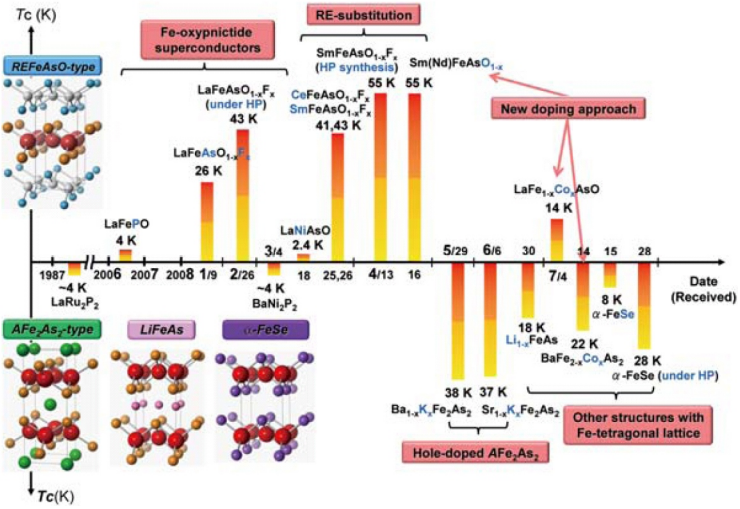

Figure 1.2: Evolution of the superconducting transition temperatures T_c in the iron-based superconductors [Hos08]. The abscissa separates the different compounds into materials with and without oxygen, respectively.

opened a new large group of superconductors, the iron-based superconductors, including different types of crystal structures. An initial rapid increase of the superconducting transition temperatures in related compounds above ~ 55 K, i.e. above the limit of conventional superconductivity of ~ 40 K (see figure 1.2), stimulated a "gold rush" in research on this group of materials, and the iron-based superconductors have been already called second class of high-temperature superconductors [Rot08c], reflecting the hope for a similar strong T_c-increase like in the cuprates. The iron-based superconductors are also layered materials[3], now with quasi-two-dimensional FeAs-sheets as common structural elements, being the playground for superconductivity, like the CuO_2 planes in the cuprates. The phase diagrams of most iron-based superconductors are very similar and strongly reminiscent of the phase diagrams of the cuprates. The ground state of the undoped parent compounds is antiferromagnetic with an AFM spin-density-wave (SDW) order, which is suppressed with doping while superconductivity can emerge. In most cases the magnetic transition

[3]For details about crystal structure and phase diagram see chapter 4.2.

is closely related to a structural transition. As a fundamental difference to the cuprates, the normal state of the iron-based superconductors is metallic and less correlated [Rot08c]. At the moment, different pairing mechanisms for the superconducting state of the iron-based superconductors are under discussion. Several theoretical calculations disfavor a standard phonon-mediated coupling mechanism [Boe10]. The observation of a magnetic resonance peak in the superconducting phase [Chr08], very similar to the one observed in the cuprates, and the close proximity to AFM order points to a similar unconventional pairing mechanism based on magnetic fluctuations. In the iron-based compounds the superconducting gap seems to have an extended $s^{\pm}$-wave symmetry [Maz09]. The comparison between the cuprate and iron-based superconductors, especially in view of the influence of AFM order in superconducting samples, is of special interest.

Raman light scattering is a very powerful spectroscopic probe for studying the physics of unconventional superconductors like the cuprates. In addition, it provides an excellent diagnostic tool to detect inhomogeneities or impurity phases in the crystal structure on a microscopical length scale. It joins the long list of spectroscopic techniques, which all have their own advantages and contribute to display a full picture of the subject of interest. For example, Raman light scattering and infrared spectroscopy are both very sensitive but complementary techniques. The big advantages of Raman light scattering are a very high energy resolution of $\lesssim 0.1$ meV and the possibility to use very small samples. Moreover, it is a technique, which probes the bulk properties with a typical penetration depth of ~ 150 nm as observed for the cuprates. In particular, the study of phonons provides a much useful information. Raman light scattering can detect subtle anomalies in the temperature dependence of optical phonons at structural or electronic phase transitions, providing information about e.g. lattice distortions, changes in the electron-phonon interaction, or even the amplitude anisotropy of the superconducting gap $\Delta(\vec{k})$. In addition, electronic Raman scattering allows a direct study of redistributions and the opening of a gap in the electronic continuum along different directions of the reciprocal space. A disadvantage of the Raman scattering technique is a limitation of the single excitations to the center of the Brillouin zone.

The main goal of this work was to study the influence of magnetic ordering phenomena and the superconducting phase transition on the electronic system of different unconventional superconductors like electron-doped cuprates or iron-based superconductors by Raman light scattering with focus on phonon anomalies. The individual projects are listed:

1. Electronic Raman scattering has yielded valuable information about the magnitude and anisotropy of the superconducting gap $\Delta(\vec{k})$ in electron-doped cuprate superconductors [Blu02, Qaz05], but superconductivity-induced phonon anomalies have thus far not been reported. Epitaxial films of $La_{2-x}Ce_xCuO_4$ (LCCO) exhibit the highest superconducting transition temperature T_c among the main series of electron-doped cuprate superconductors (see chapter 4.1). This work presents a detailed temperature-dependent Raman light scattering study on two molecular-beam-epitaxy-grown films of LCCO with different doping levels close to optimal doping, which had been the basis of prior transport measurements [Wag08a, Wag08b, Mül06]. Since electronic Raman scattering is difficult in films, the focus of this project was put on phonon anomalies at T_c, attempting to gain insight into the superconducting energy gap of LCCO. In addition, a detailed characterization and microstructural analysis of the films was performed by various experimental techniques.

2. The iron-based superconductors exhibit four known types of crystal structures. The largest structure family are the pnictides, which include the oxypnictides and ternary iron arsenides. In contrast to the oxypnictides, large high-quality single crystals are available for the ternary iron arsenides. This work presents a first detailed temperature-dependent Raman light scattering study on different superconducting and non-superconducting ternary iron arsenide single crystals with hole- and electron doping. The main focus was put on phonon anomalies induced by a structural and SDW phase transition and the superconducting phase transition. The experimental results are compared to predictions of *ab initio* density-functional calculations and to related observations in the cuprates.

3. The iron chalcogenide system $Fe_{1+y}Se_xTe_{1-x}$ (FST) belongs to the family of iron-based superconductors. This class of materials shows a similar but less complex crystal structure compared to the iron pnictides with Te/Se instead of As. Due to this simplification, FST is particularly interesting for a comparative study. This work presents a first detailed temperature-dependent Raman light scattering study of superconducting and non-superconducting iron chalcogenide single crystals with different concentrations of Se and Fe excess with focus on phonon anomalies at magnetic transitions. The results are compared to related observations in the iron pnictides.

This thesis is organized as follows:
Chapter 2 presents the basics of Raman light scattering. The measurement techniques used are described in chapter 3. The materials studied are characterized in chapter 4. Chapter 5 contains the results of this thesis, which is summarized in chapter 6.

Chapter 2

Basics of Raman light scattering

2.1 The Raman process[1]

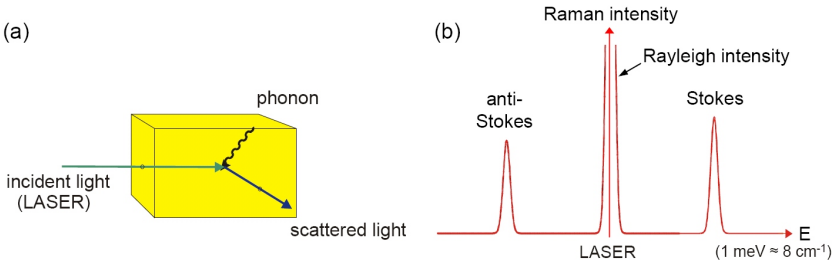

Figure 2.1: (a) Cartoon of the Raman process, (b) simplified Raman spectrum ("LASER" denotes the energy of the exciting laser line).

When light is incident on a solid, most of the light is either reflected, transmitted, or absorbed. Additionally, a lower fraction is scattered into directions different from those described by the macroscopic Fresnel equations. Elastic (Rayleigh) scattering, e.g. by surface defects, conserves the energy of the incident light, while inelastic scattering is combined with an

[1] The details of Raman light scattering can be looked up in [Car83, Car82, Mer00].

energy change due to creation (Stokes) or annihilation (anti-Stokes) of elementary excitations like phonons, magnons, or electronic excitations (see figure 2.1a). Inelastic light scattering is called Raman scattering (Brillouin scattering for scattering by acoustic phonons). The present work mainly focuses on Raman scattering by optical phonons. Due to a $\sim 10^6\times$ weaker inelastic scattering intensity compared to elastic scattering, a laser is required as intense light source. Raman scattering experiments are typically carried out in the visible range. In order to study low energy excitations like phonons ($\sim$ 10 meV) with optical photons ($\sim$ 1 eV) a good resolution and rejection of the reflected and elastically scattered light is required.

For first order Raman processes, including one phonon, one has

$$\hbar\omega_i = \hbar\omega_s \pm \hbar\omega_p \quad \text{(energy conservation)} \tag{2.1}$$

$$\vec{k}_i = \vec{k}_s \pm \vec{q} \qquad \text{(momentum conservation)}, \tag{2.2}$$

where ω_i and ω_s indicate the frequency of incident and scattered light and ω_p the frequency of the phonon and $\vec{k}_i$, $\vec{k}_s$, and $\vec{q}$ the corresponding wave vectors, respectively. $+$ stands for the creation and $-$ for the annihilation of an elementary excitation, respectively. Due to the mass dependence $\omega_p \sim \sqrt{\kappa/m}$ of a harmonic oscillator, where κ is the spring constant, phonons including atoms with higher mass exhibit lower frequencies.

Figure 2.1b shows a simplified Raman spectrum. The strong central peak indicates the elastically scattered laser light. The energy of the exciting laser line determines the origin of the energy axis. As a consequence, the energy values of an elementary excitation do not depend on the absolute energy of the exciting light, in contrast to luminescence phenomena. In case of experimental imperfections, e.g. roughness of the sample surface, the elastic peak can become very strong, dominating the Raman spectrum. The energies of an elementary excitation involved in a Stokes or anti-Stokes process are symmetrically displaced from the origin with positive and negative energy values, respectively. Since the anti-Stokes process requires a finite population of thermally excited states, the anti-Stokes intensity depends strongly on temperature and is very weak at low temperatures. In order to maximize the intensity, the focus was put on the Stokes process. The background of the Raman spectrum contains contributions from electronic single particle excitations, phonons, and magnons [Ulr].

For the frequency of the incident laser light one has

$$\omega_i = \frac{|\vec{k}_i| n}{c}, \tag{2.3}$$

where c is the speed of light and n is the dispersion index ($n \approx 1$ for scattering in air). Due to the steep dispersion relation of light, photons in the optical range carry only relatively small momenta, corresponding to wave vectors $|\vec{k_i}| \sim 10^{-3}$ Å^{-1} that are $10^2 - 10^3$ times smaller compared to typical reciprocal space vectors $\vec{G}$ in a crystal lattice. Therefore, in first order Raman processes only phonons near the Brillouin zone (BZ) center (Γ point) with $|\vec{q}| \approx 0$ ($\vec{k_i} - \vec{k_s} \approx 0$) can be detected . Because of the very small momentum transfer in combination with the Pauli principle, elementary electronic excitations are only possible close to the Fermi energy. On the other hand, second order Raman processes, including two phonons with $\vec{q_1} + \vec{q_2} \approx 0$, can probe the phonon density of states in the whole BZ.

Due to the high mass of the atoms in a crystal lattice, direct coupling of light to phonons is negligible [Mar71]. On the other hand, light couples strongly to electric dipole moments [Hay78], leading classically to an oscillating electric dipole density. Note that the dominant electric dipole moments are induced by excitations of electrons across energy bandgaps (interband transitions) by the exciting laser light [Pin83]. In the classical picture the inelastic light scattering process can be understood as a modulation of the oscillating electric dipole density by the elementary excitations [Pin83]. The modulation is described by derivatives of the electrical susceptibility with respect to the elementary excitation (see 2.1.1). In a quantum mechanical picture inelastic light scattering is described via virtual photon-electron and electron-phonon interactions (see 2.1.2).

2.1.1 Semi-classical description

Since $|\vec{k_i}| << |\vec{G}|$, the electric field $\vec{E_i}(\vec{r}, t) = \vec{E}_{i,0} \cos(\vec{k_i} \cdot \vec{r} - \omega_i t)$ ($\vec{r}$ vector in real space, t time) of the incident light is approximately constant within a crystal unit cell (dipole approximation). In an isotropic solid $\vec{E_i}$ induces a macroscopic polarization $\vec{P}$ (electric dipole density) according to

$$\vec{P} = \varepsilon_0 \chi \vec{E_i} = \varepsilon_0 \chi E_i \hat{e}_i, \tag{2.4}$$

where ε_0 is the dielectric constant, χ the electrical susceptibility, containing microscopic information about phononic contributions, and $\hat{e}_i$ the unit vector of the electric field, respectively. In harmonic approximation a lattice vibration has the form $\vec{u}(\vec{r}, t) = \vec{u}_0 \cos(\vec{q} \cdot \vec{r} - \omega_p t)$, where $\vec{u}$ describes the displacement of the atoms from their average position. Due to the much lower mass of the electrons compared to the nuclei, the electrons

follow nearly instantaneously the much slower motion of the nuclei (Born-Oppenheimer or adiabatic approximation). If the amplitude of the lattice vibration $\vec{u}_0$ is small compared to the lattice constants, one can expand

$$\chi = \chi_0 + \frac{\partial \chi}{\partial \vec{u}}|_0 \cdot \vec{u}(\vec{r},t) + \frac{\partial^2 \chi}{\partial \vec{u}^2}|_0 \cdot \vec{u}^2(\vec{r},t) + \dots \ . \tag{2.5}$$

χ_0 describes the electrical susceptibility without phononic contribution, while $\frac{\partial \chi}{\partial \vec{u}}\vec{u}$ describes the modulation of the electrical susceptibility by the phonon. $\frac{\partial \chi}{\partial \vec{u}}$ corresponds to first order Raman processes, including one phonon. $\frac{\partial^n \chi}{\partial \vec{u}^n}$ corresponds to Raman processes of higher orders, e.g. $\frac{\partial^2 \chi}{\partial^2 \vec{u}}$ including 2 phonons. By inserting equation (2.5) into equation (2.4) and ignoring orders higher than first order Raman processes, one obtains

$$\vec{P}(\vec{r},t) = \left[\chi_0 + \frac{\partial \chi}{\partial \vec{u}}\vec{u}(\vec{r},t)\right]\vec{E}_i(\vec{r},t) \tag{2.6}$$

$$= \chi_0 \vec{E}_i(\vec{r},t) + \left(\frac{\partial \chi}{\partial \vec{u}}\vec{u}(\vec{r},t)\right)\vec{E}_i(\vec{r},t). \tag{2.7}$$

The first term describes oscillations of the macroscopic polarization, which are in phase with the incident radiation, corresponding to elastic scattering. The second term includes frequency shifts due to lattice vibrations, describing inelastic light scattering. For the inelastic part one has

$$\vec{P}_{in}(\vec{r},t) = \left(\frac{\partial \chi}{\partial \vec{u}}\vec{u}(\vec{r},t)\right)\vec{E}_i(\vec{r},t) \tag{2.8}$$

$$= \frac{1}{2}\frac{\partial \chi}{\partial \vec{u}}\vec{u}_0\vec{E}_{i,0}\left[\cos\left(\left(\vec{k}_i + \vec{q}\right)\cdot\vec{r} - \left(\omega_i + \omega_p\right)t\right) + \cos\left(\left(\vec{k}_i - \vec{q}\right)\cdot\vec{r} - \left(\omega_i - \omega_p\right)t\right)\right]. \tag{2.9}$$

The first cos-term describes phonon annihilation (anti-Stokes process), while the second cos-term describes phonon creation (Stokes process). Note that in second order Raman processes the frequencies of the scattered phonons are shifted from the frequency of the incident light by $\pm\omega_1 \pm \omega_2$, where ω_1 and ω_2 are the frequencies of the two phonons involved [Yu01].

In general, $\frac{\partial \chi}{\partial \vec{u}}$ is a third rank tensor with components determined by the symmetries of the scattering medium and the lattice vibration [Hay78, Pin83]. By introducing a unit vector $\hat{u}$ parallel to the atomic displacement of the lattice vibration, one can define the second rank tensor

$$R = \frac{\partial \chi}{\partial \vec{u}}|_0 \cdot \hat{u}. \tag{2.10}$$

R is the so-called Raman tensor. Since χ contains the full symmetry of the lattice, R reflects the symmetry of the lattice distortion by the phonon.

For the radiation energy emitted per unit time into a space element $d\Omega$ of an electric dipole $\vec{M}$ oscillating with a frequency ω_s one has [Car82]

$$\frac{dW_s}{d\Omega} = \frac{\omega^4}{(4\pi)^2 \varepsilon_0 c^3} |\hat{e}_s \cdot \vec{M}|^2 \tag{2.11}$$

where $\hat{e}_s$ is a unit vector representing the polarization of the scattered light. For a number of dipoles $\vec{M}$ oscillating coherently in a volume V one has $\vec{M} = V\vec{P}$. Note that in Raman light scattering the different atoms scatter incoherently, leading to a term only linear in V [Car82]. Inserting equation (2.5) into (2.11) and dividing by the energy of the incident light per unit time $W_i = \varepsilon_0 c E_i^2$, yields the differential scattering cross section

$$\frac{d^2\sigma}{d\Omega d\omega} = \frac{V}{(4\pi)^2} \cdot \left(\frac{\omega_s}{c}\right)^4 \cdot \left| \hat{e}_s \cdot \frac{d\chi}{d\vec{u}} \cdot \hat{e}_i \right|^2 \cdot \left\langle \vec{u}^2 \right\rangle \ , \tag{2.12}$$

where $\left\langle \vec{u}^2 \right\rangle$ represents the thermodynamical average over the atomic displacements. For the total energy of a harmonic oscillator one has

$$E_{HO} = M\omega_p^2 \left\langle \vec{u}^2 \right\rangle = \hbar\omega_p \left[n + \frac{1}{2} \right] \text{ with } n = \frac{1}{e^{\frac{\hbar\omega}{k_B T}} - 1}, \tag{2.13}$$

where the last expression is the corresponding quantum mechanical value. n is the Bose-Einstein statistical factor. By reorganizing, one obtains

$$\left\langle \vec{u}^2 \right\rangle = \frac{\hbar}{2M\omega_p} \left[2n + 1 \right]. \tag{2.14}$$

This equation contains Stokes and anti-Stokes processes. In order to separate both contributions one can use second-quantization [Car82]

$$\text{Stokes } \langle uu^\dagger \rangle = \quad \langle n|u|n+1\rangle\langle n+1|u^\dagger|n\rangle = \frac{\hbar}{2\omega_p M}(n+1) \tag{2.15}$$

$$\text{anti} - \text{Stokes } \langle u^\dagger u \rangle = \qquad \langle n|u^\dagger|n-1\rangle\langle n-1|u|n\rangle = \frac{\hbar}{2\omega_p M} n \ . \tag{2.16}$$

For the Stokes process one obtains the final equation

$$\frac{d^2\sigma}{d\Omega d\omega} \sim \frac{V}{(4\pi)^2} \cdot \left(\frac{\omega_s}{c}\right)^4 \cdot \left| \hat{e}_s \cdot \frac{d\chi}{d\vec{u}} \cdot \hat{e}_i \right|^2 \cdot \frac{\hbar}{2\omega_p} \left[n + 1 \right], \tag{2.17}$$

while for the anti-Stokes process the term $[n+1]$ has to be replaced by n.

The differential scattering cross section is directly proportional to the measured Raman intensity I, i.e. the scattering efficiency, yielding

$$I \sim |\hat{e}_s \cdot R \cdot \hat{e}_i|^2 . \tag{2.18}$$

The Raman intensity depends on the polarization of incident and scattered light and on the symmetry of the Raman tensor (see 2.1.4). By changing the polarization geometry (selection rules), one can probe the components of R and the symmetries of the phonon. In order to indicate the different polarization geometries, here, the Porto notation l(ij)m is used, where l and m denote the direction of incident and scattered light and (ij) their polarization, respectively. For example, z(xy)z corresponds to incident and scattered light propagating along the crystallographic c axis with polarization along the crystallographic a and b axis, respectively. For time reversal symmetric processes, e.g. Raman scattering at phonons, l(ij)m=l(ji)m.

By comparing equation (2.15) and (2.16) one obtains for the ratio between the Raman intensities for Stokes and anti-Stokes processes

$$\frac{I_{\mathrm{Stokes}}}{I_{\mathrm{anti-Stokes}}} = \frac{n+1}{n} = e^{\frac{\hbar\omega}{k_B T}} . \tag{2.19}$$

Both intensities become equal only for large temperatures. For T→0 the anti-Stokes intensity goes to zero, while the Stokes intensity remains nonzero. Therefore, the intensity ratio between Stokes and anti-Stokes can be used for an estimation of the temperature of the scattering medium.

2.1.2 Quantum mechanical description

A major aspect, which requires quantum mechanics and cannot be described in the classical picture, is resonant Raman light scattering. If the energy of the incident or scattered light coincides with the energy of a real electronic transition, the Raman intensity becomes tremendously large.

In quantum mechanics inelastic light scattering is typically described in third order time dependent perturbation theory. The Hamilton operator for scattering from phonons considers two types of perturbation terms:

$$H = H_0 + H_{ER} + H_{EP}, \tag{2.20}$$

where H_0 is the Hamilton operator of the unperturbed system, H_{ER} describes the electron-photon and H_{EP} the electron-phonon interaction.

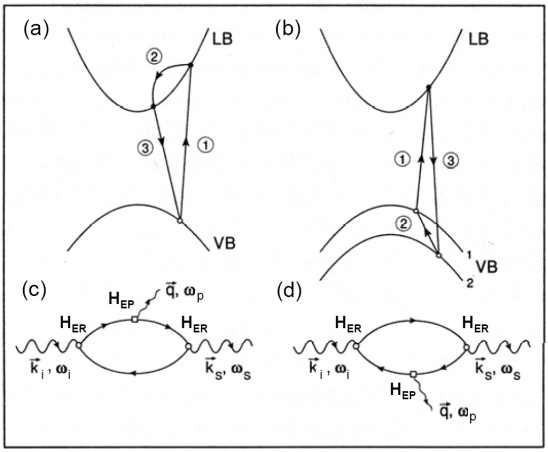

Figure 2.2: First-order Stokes-Raman processes: (a) two-band scattering process (intra-band scattering), (b) three-band scattering process (inter-band scattering), and (c)+(d) corresponding Feynman diagrams [Pin83].

The scattering process is separated into three virtual steps. Figure 2.2a shows a typical two-band scattering scenario (intra-band scattering):

1. An incident photon excites an electron across the band gap, creating an electron-hole pair (H_{ER}). The excited state can be real or virtual.

2. The excited electron is scattered into another real or virtual intermediate state, while creating or absorbing a phonon (H_{EP}).

3. The excited electron falls back into the ground state and recombines with the hole by emitting a photon (H_{ER}).

While momentum conservation must be satisfied for each interaction step, energy conservation holds only for the whole scattering process. Note that the small momentum transfer between the intermediate states is provided by the photon and the initial state is equal to the final state. Phononic processes are symmetric under time reversal. Therefore, the three interaction steps can take place in arbitrary order, leading to $3! = 6$ possible permutations. In addition, the corresponding hole processes have to be included. Beside two-band processes, scattering scenarios with multiple bands are possible. Figure 2.2b shows a three-band scattering scenario (inter-band scattering). Each process contributes six permutations.

Figure 2.2c + d show the corresponding Feynman diagrams of the two- and three-band scattering scenarios, respectively. The dots represent the different interaction vertices. By applying Fermis's golden rule together with perturbation theory on each vertex, one obtains for the transition matrix element of the two-band scattering scenario of an electron:

$$W_{s,i} \sim \sum_{\alpha,\beta} \left\{ \frac{\langle i|H_{ER}|\beta\rangle\langle\beta|H_{EP}|\alpha\rangle\langle\alpha|H_{ER}|i\rangle}{(E_\beta - \hbar\omega_s)(E_\alpha - \hbar\omega_i)} + 5 \text{ permut.} \right\}, \qquad (2.21)$$

where α and β represent the two intermediate states, respectively. By summing over all possible scattering channels one obtains for the total differential scattering cross section for Stokes processes [Car83]

$$\frac{d^2\sigma}{d\Omega d\omega} \sim V(\frac{\omega_s}{c})^4 \frac{\omega_i}{\omega_s} \cdot [n+1] \cdot \sum_{s,i} |W_{s,i}|^2 \, \delta(\hbar\omega_i - \hbar\omega_s - \hbar\omega_p), \qquad (2.22)$$

where $\delta(E)$ is the delta function guaranteeing energy conservation.

If the energy of the incident or scattered light coincides with a real bandgap of an electron-hole excitation, the denominator in equation (2.21) becomes zero. In this case the transition matrix element goes to infinity and the scattering cross section, i.e. the Raman intensity, becomes large at particular photon energies. This scenario is called resonant Raman light scattering. The resonant enhancement of the Raman intensity can be used, e.g., to study and identify the magnitude of electronic bandgaps.

2.1.3 Electronic Raman scattering

The electronic single particle excitations divide into resonant inter-band and non-resonant intra-band transitions. In HTSC the electronic bandgaps are relatively large ($\sim$ 1 eV). Therefore, the main contribution to electronic Raman scattering in these materials comes typically from intra-band transitions near the Fermi energy. In materials with a high number of free charge carriers, one expects only a weak intensity of the electronic signal due to screening effects. In contrast, nearly all HTSC show a relatively large and constant Raman background intensity up to energies of $\sim$ 1 eV in the normal state [Rez91, Sta90]. The nature of this background intensity is still not completely clarified. Strong redistributions of the background intensity at T_c (see below) suggest an electronic origin [Ein96, Hac89].

For electronic Raman scattering the differential scattering cross section has the form [Kle83]

$$\frac{\partial^2\sigma}{\partial\Omega\partial\omega} \sim \frac{\omega_s}{\omega_i} r_0^2 S(\vec{q},\omega) \tag{2.23}$$

$$\text{with } S(\vec{q},\omega) = \sum_f |\langle f|\rho_q|i\rangle|^2 \, \delta(\hbar\omega - \hbar\omega_f + \hbar\omega_i) \tag{2.24}$$

where ρ_q is the electronic-density-fluctuation operator and $r_0 = e^2/mc^2$ is the classical Thomson radius of an electron. S is the so called dynamical structure factor, representing the power spectrum of all possible density fluctuations. By the use of the fluctuation-dissipation theorem [Pin66], S can be related to the imaginary part of a density-density response function. In case of a generalization to Raman light scattering one obtains

$$S(\vec{q},\omega) = -\frac{\hbar}{\pi}\,[n+1]\,\chi''(\vec{q},\omega), \tag{2.25}$$

where χ'' is the imaginary part of the effective Raman response function. S is directly proportional to the measured Raman intensity. Due to the Bose factor $[n+1]$, the electronic background of the Raman spectrum is expected to be strongly temperature-dependent for energies $\hbar\omega < kT$. However, in most cuprates S was found to be independent of temperature and energy [Sta90] and, therefore, the energy and temperature dependence of χ'' was suggested to compensate that of the Bose factor [Hey91]. In order to study possible redistribution effects in the electronic background, one has to get rid of the Bose dependence in the Raman intensity by dividing S by the Bose factor. Note that the background intensity contains additional contributions from magnons and higher order phonon processes [Ulr].

At the superconducting phase transition, the electronic background intensity shows characteristic redistributions in energy, depending on the symmetry of the superconducting gap and the polarization geometry [Ein96]. Figure 2.3 shows the normalized electronic background intensity of a Raman spectrum of the HTSC $YBa_2Cu_3O_7$ (YBCO) at different temperatures below T_c for the z(x'x')z polarization configuration. Note that the superconducting gap of YBCO has d-wave symmetry and Δ_0 denotes the maximum of the gap function. For energies $E < 2\Delta_0$ the electronic background intensity is reduced, because only a limited number of electronic states are available, while at $E = 2\Delta_0$ all Cooper pairs can be broken, yielding an enhanced Raman scattering efficiency ("coherence peak" in the electronic density of states) compared to the normal state. For $E >> 2\Delta_0$

the electronic background intensity approaches the normal state limit. For a gap with d-wave symmetry, the "coherence peak" is broad and depends on the polarization geometry [Ein96] (see 2.1.4), while for s-wave superconductors the "coherence peak" appears always close to $E = 2\Delta_0$ with nearly no electronic excitations at lower energies [Mon90, Kle84].

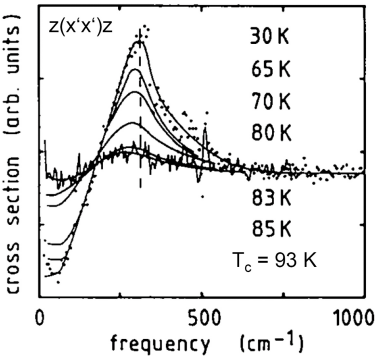

Figure 2.3: Temperature dependence of the normalized electronic background intensity in $YBa_2Cu_3O_7$ [Hac89]. (x' corresponds to a polarization parallel to the ab-plane, but rotated by 45° with respect to the c axis.)

2.1.4 Selection rules and symmetry

When equation (2.18) is different from zero for a particular mode for at least one polarization configuration, the mode is called Raman-allowed or Raman-active, while it is called Raman-forbidden or Raman-inactive otherwise [Mer00]. All of the materials studied in this work contain a center of inversion. In the presence of inversion symmetry, the even modes ($R_{ij} = R_{ji}$) are Raman-allowed, while the odd modes ($R_{ij} = -R_{ji}$) are Raman-forbidden [Mer00]. For infrared (IR) allowed modes, carrying a dipole moment and coupling directly to light, it is just vice versa [Mer00]. For inversion symmetry, Raman and IR experiments are complementary techniques. Note that single atomic displacements carry a dipole moment and, therefore, for an even mode one needs at least two atoms vibrating with a phase difference of π. In an ideal crystal lattice exceptions from these selection rules are only allowed for excitations that are not invariant under time-reversal symmetry [Mer00]. However, in the presence of lattice disorder, Raman forbidden modes can become Raman active [Car00]. In

A	*symmetric under rotation about principle axis by 90°*
B	*anti-symmetric under rotation about principle axis by 90°*
E	*in-plane mode*
$_g$	*symmetric under inversion (even mode)*
$_u$	*anti-symmetric under inversion (odd mode)*
$_1$	*generally arbitrary to distinguish*
$_2$	*symmetric with respect to other rotations*

Table 2.1: Symbols characterizing the irreducible representations and symmetries of phonons and scattering geometries (Mulliken notation).

$$\underset{\mathrm{A}_{1g}}{\begin{pmatrix} xx & 0 & 0 \\ 0 & xx & 0 \\ 0 & 0 & zz \end{pmatrix}} \quad \underset{\mathrm{B}_{1g}}{\begin{pmatrix} xx & 0 & 0 \\ 0 & -xx & 0 \\ 0 & 0 & 0 \end{pmatrix}} \quad \underset{\mathrm{E}_{g}}{\begin{pmatrix} 0 & 0 & xz \\ 0 & 0 & 0 \\ zx & 0 & 0 \end{pmatrix}} \quad \underset{\mathrm{E}_{g}}{\begin{pmatrix} 0 & 0 & 0 \\ 0 & 0 & xz \\ 0 & zx & 0 \end{pmatrix}}$$

Table 2.2: Irreducible representations of the Raman tensor in a tetragonal perovskite crystal structure with space group 4/mmm (D_{4h}), which correspond to the Raman-allowed optical modes in this structure [Hay78].

case of resonant Raman light scattering the resonant forbidden modes can become even much stronger than the resonant allowed modes [Mer00].

A general classification of the different lattice vibrations can only be given in terms of group theory [Hay78]. For phonons with $|\vec{q}| \approx 0$ all involved atoms are vibrating in-phase in the different unit cells of the crystal lattice. Therefore, it is sufficient to consider only the symmetries of a single unit cell. The atomic dislocations leave only a part of the symmetries of the unit cell undistorted. As a consequence, the different vibration patterns can be attributed to the different irreducible representations of the point group of the crystal lattice, resulting from each of the non-equivalent occupied sites in the unit cell (site symmetries). The number of non-degenerate vibrations corresponds to the number of symmetry operations in the unit cell, while the total number of vibrations is given by $3s$, where s is the number of atoms per unit cell. Note that $3s$ divides into $(3s-3)$ optical modes and 3 acoustic modes. Table 2.1 gives an overview of the typical symbols characterizing the irreducible representations and symmetries (Mulliken symbols), while table 2.2 lists the irreducible representations of the Raman tensor R in a tetragonal perovskite crystal structure with

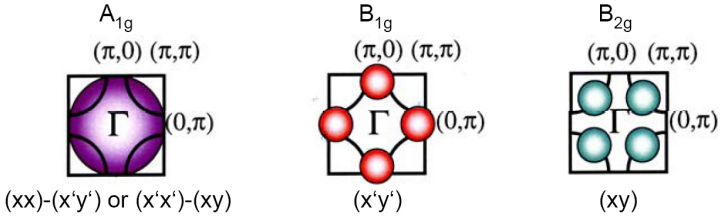

Figure 2.4: Weighted and averaged integration areas for electronic Raman scattering plotted on a simplified Fermi surface with corresponding observable polarization configurations for cuprate HTSCs [LeT06].

space group 4/mmm (D_{4h}), which correspond to the Raman-allowed optical modes in this structure [Hay78]. A list of all possible Raman tensors and site symmetries for the different space groups is given in [Rou81]. By choosing appropriate polarization geometries according to equation 2.18 one can selectively choose the different phonons and different symmetries.

Related selection rules can be derived for all elementary excitations. In electronic Raman scattering the different polarization configurations can be used to selectively probe in average specific parts of the Fermi surface, e.g. the $\vec{k}$-dependence of the superconducting gap $\Delta(\vec{k})$. Figure 2.4 shows the different integration areas together with the corresponding observable polarization configurations or symmetry in a cuprate HTSC. For example, for a d-wave gap the "coherence peak" appears at higher/lower energies for B_{1g} and B_{2g} symmetry, respectively [Ein96]. Note that the collected Raman intensity is proportional to the square of the gap function and, therefore, only sensitive to the amplitude, but insensitive to the phase.

2.2 Phonon interactions

A phonon is characterized by its frequency, linewidth, integrated intensity, and lineshape. The standard temperature dependence of optical phonons is dominated by the phonon-phonon interaction (see 2.2.1). Deviations from this behavior are called phonon anomalies, containing information about the physics of the material studied. A possible origin of phonon anomalies are phase transitions, e.g. the opening of a gap in the electronic continuum, to be described in the context of electron-phonon interaction (see 2.2.2).

2.2.1 Phonon-phonon interaction

In harmonic approximation the different phonons are considered to be stable and independent of each other. However, in a real crystal the phonons can collide, decay, or merge, leading to a finite lifetime and a frequency shift with respect to the pure harmonic description (quasi-harmonic modes). It has been shown that the main contribution to a finite phonon lifetime comes from phonon decay into other phonons [Cow68]. Note that the phonon lifetime τ is related to the phonon linewidth Γ through the energy-time uncertainty relation, according to $\Gamma \sim 1/\tau$. Since the phonon interaction probability depends on the probability for excited phononic states, the lifetime of a particular phonon changes with temperature. For higher temperatures the number of possible phonon decay channels is higher, leading to shorter lifetimes, i.e. a broadening of the phonon linewidths.

In order to include phonon-phonon interactions quantitatively, one can expand the interatomic potential up to the lowest-order terms beyond the harmonic approximation (anharmonic terms) [Cow68]. The changes in the phonon lifetime and frequency due to the anharmonic interactions are described by the phonon self-energy $\Sigma(\omega_0) = \Delta(\omega_0) + i\Gamma(\omega_0)$ [Men84, Cow68], where ω_0 is the frequency of the pure harmonic phonon. The real part of the phonon self-energy $\Delta(\omega_0)$ determines the phonon frequency, while the imaginary part $\Gamma(\omega_0)$ determines the corresponding linewidth, respectively. For the frequency of the quasi-harmonic mode one has [Men84]

$$\omega_p = \omega_0 + \Delta(\omega_0). \tag{2.26}$$

$\Delta(\omega_0)$ and $\Gamma(\omega_0)$ are related by the Kramers-Kronig relation [Mar62].

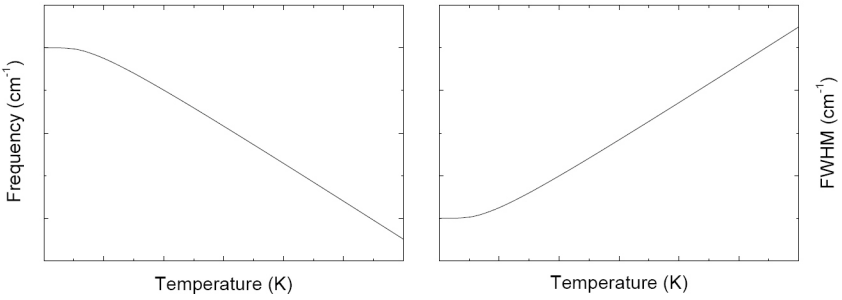

Figure 2.5: Temperature dependence of the frequency and FWHM of an optical mode according to phonon anharmonicity (see text for details).

Combinations of the different acoustic and optical phonon branches provide the most important decay channels for optical phonons [Men84]. In a simplified picture the decay of an optical phonon can be described by a symmetric decay into two acoustic phonons of the same branch with identical energy $E = \omega_0/2$ and opposite momenta (Klemens decay) [Kle66]. For simplification, in the present work, a symmetric anharmonic phonon decay into two product modes was assumed, which leads to the following expressions for the phonon frequency ω_{ph} and corresponding linewidth Γ_{ph} (FWHM = full width at half maximum) [Men84, Had98]:

$$\omega_{ph}(T) = -A\left(1 + \frac{2a}{exp(\hbar\omega_0/2k_BT) - 1}\right) + \omega_0,$$
$$\Gamma_{ph}(T) = \Gamma_a\left(1 + \frac{2a}{exp(\hbar\omega_0/2k_BT) - 1}\right) + \Gamma_b,$$

where A and Γ_a are positive constants and a corrects for terms arising from nonsymmetric phonon decay processes. Γ_b represents an additional temperature-independent linewidth contribution, e.g. due to scattering by impurities [Had98]. The terms in brackets account for the phonon occupation probability in the thermal equilibrium according to Bose statistics, where the factor 2 accounts for the decay into two phonons. For an overview, figure 2.5 shows the typical temperature dependence of ω_{ph} and Γ_{ph} due to phonon anharmonicity according to equation (2.27) and (2.27). Due to the conservation of spectral weight (sum rule), the corresponding integrated intensity is temperature independent in the ideal case.

2.2.2 Electron-phonon interaction

In addition to phonon anharmonicity, a phonon can decay into electronic excitations by the electron-phonon interaction, leading to an additional contribution to the phonon lifetime and a renormalization of the phonon frequency. Thereby, the phonon can only interact with the electronic states, if phonon and electrons have roughly the same energy and the same symmetry. In a superconducting material the electronic system exhibits a large redistribution in the electronic density of states (see figure 2.3), leading to changes in the number of electronic decay channels. Only phonons with energies $E_p \geq 2\Delta(\vec{k})$ are able to interact with the electrons, contributing to Cooper pair breaking. Thereby, the number of decay channels for phonons with $E_p \gtrsim 2\Delta$ is increased (see figure 2.3), leading to shorter

phonon lifetimes, i.e. broadening of the phonon linewidth. On the other hand, for phonons with $E_p < 2\Delta_0$ in s-wave superconductors the number of decay channels is strongly reduced, leading to longer phonon lifetimes, i.e. narrowing of the phonon linewidth. For d-wave superconductors the presence of nodes in the gap function together with the averaging over certain areas in $\vec{k}$-space (see 2.1.4) allows pair breaking even for phonons with $E_p < 2\Delta_0$ leading to shorter lifetimes, i.e. broadening, for all $E_p \sim 2\Delta$.

The electron-phonon coupling is qualitatively described by an additional contribution to the phonon self-energy (see 2.2.1) [Zey90, Nic93, Dev94]. In order to describe phonon self-energy anomalies, induced by the opening of a gap in the electronic continuum, one considers changes in the electron-phonon contribution to the phonon self-energy at the phase transition, while neglecting other contributions. Note that this theory has been established based on hole-doped HTSC and corresponding experimental observations are widely consistent with this theory [Bak09]. Figure 2.6 shows the real and imaginary parts of the phonon self-energy in the superconducting state of the d-wave superconductor $YBa_2Cu_3O_7$ below T_c, corresponding to frequency and linewidth renormalizations, respectively.

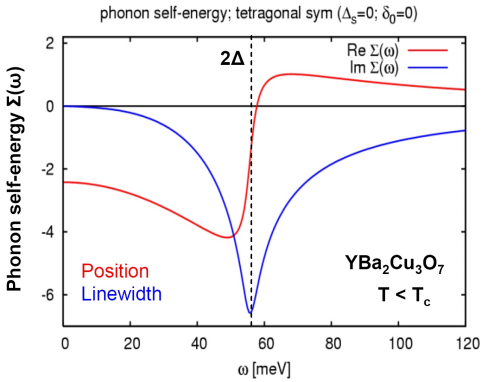

Figure 2.6: Real and imaginary part of the phonon self-energy in the cuprate HTSC $YBa_2Cu_3O_7$ (d-wave symmetry) below T_c [Man]. (The corresponding functions for the normal state above T_c are taken as zero.)

While the imaginary part of the phonon self-energy is negative both for $E < 2\Delta$ and $E > 2\Delta$, the corresponding real part changes its sign from negative to positive at $E = 2\Delta$. This means that optical phonons with energies above (below) 2Δ are expected to show a hardening (soft-

ening) and broadening below T_c. Deviations from this behavior are predicted only close to 2Δ [Zey90]. A typical frequency renormalization in $YBa_2Cu_3O_7$ between T_c and the lowest temperature is ~ 6 cm^{-1}. The phonon renormalizations are strongest for energies close to 2Δ and depend on the electron-phonon coupling of the specific mode under consideration. Due to the electron-phonon interaction one expects an increase in the integrated phonon intensity below T_c according to [Had99]

$$I_p = \left[\sqrt{I_p^0} + \frac{V}{\omega_{el} - \omega_p}\sqrt{I_{el}}\right]^2 , \tag{2.27}$$

where I_p and I_p^0 are the integrated intensities of the coupled and bare phonon, I_{el} and ω_{el} the integrated intensity and maximum position of the "coherence peak", and V the electron-phonon coupling constant, respectively. For a more detailed intensity consideration see [Mis99].

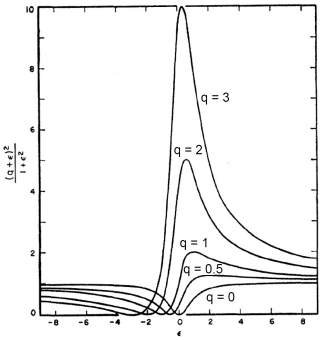

Figure 2.7: Natural Fano lineshapes for different values of the asymmetry parameter q [Fan61]. The maxima and minima, shifted from the center, correspond to constructive and destructive interference, respectively.

The interference of discrete phononic and continuous electronic Raman scattering in the presence of electron-phonon coupling leads typically to asymmetric phonon lineshapes with a so-called Fano profile (see figure 2.7) [Fan61, Hey91]. The asymmetry parameter $q \sim 1/(V\rho)$ reflects the strength of the electron-phonon coupling V and the number of electronic decay channels for the phonon ρ. Changes in the phonon self-energy can lead to changes in q. For $q > 10$ and $q = 0$ the Fano peak is nearly indistinguishable from a Lorentzian. Note that the Fano profile can be suppressed due to additional linewidth contributions, like e.g. structural defects.

Chapter 3

Measurement techniques

For the Raman measurements two different setups were used. In order to maximize the effective spectral resolution and to include the low energy excitation range $E < 100$ cm^{-1} a "macro" setup was available. For higher spatial resolution, e.g. in inhomogeneous or very small samples, and a higher intensity yield, a "micro" setup was used. Due to small optical penetration depths (~ 150 nm) compared to the thickness of the samples studied, all measurements were carried out in a backscattering geometry.

3.1 "Macro"-Raman setup

The central unit of the "macro" setup was a DILOR XY triple grating spectrometer. Figure 3.1 shows a picture of the "macro" setup in use, while figure 3.2 gives a simplified overview about the optical path. The spectra were taken in a quasi-backscattering geometry, as indicated in figure 3.2, with the incident laser light quasi-parallel to the direction normal to the sample surface. The sample was slightly tilted out of the parallel line in order to block the ideally reflected light. A smaller tilt angle resulted in a higher Raman intensity. For excitation a 5 W Ar^+/Kr^+ mixed-gas laser was used, which provided 13 different laser lines (see table 3.1).

Ar^+	454.5, 457.9, 465.8, 472.7, 476.5, 488.0, 496.5, 501.7, 514.5
Kr^+	520.8, 530.9, 568.2, 647.1

Table 3.1: Laser lines in nm provided by an Ar^+/Kr^+ mixed-gas laser.

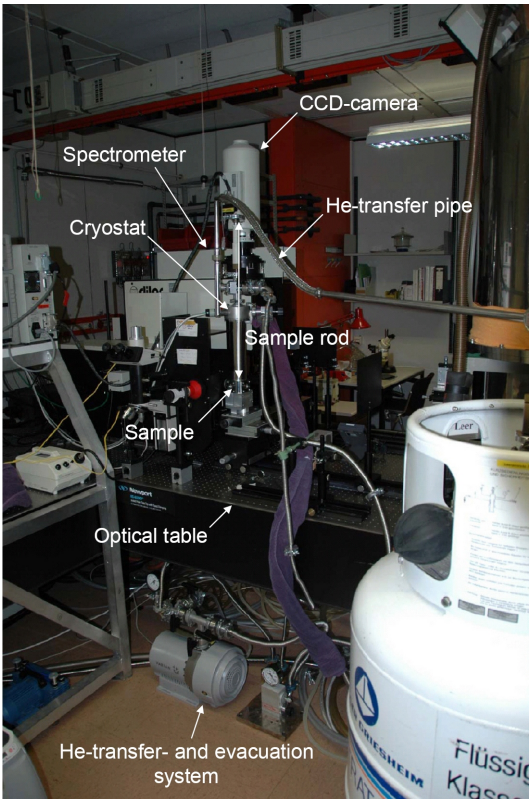

Figure 3.1: "Macro" setup for Raman light scattering.

The incident laser beam was linearly polarized by a double refractive prism. In order to rotate the polarization axis a Fresnel-rhombus was used. Beyond the major amplified laser line a laser contains additional weaker plasma lines at slightly different wavelengths due to additional optical transitions. In order to suppress these plasma lines appropriate plasma filters with narrow transmitting bandwidths for each laser line were used. Several pinholes further enhanced the beam quality by a lateral contraction of the beam diameter and a suppression of stray light, caused by non-ideal transmission and reflection, e.g. at mirrors. The full optical setup was seated on a vibration-damped optical table. Finally, the laser beam was focussed by a 40 mm-diameter lens (focal length $f = 60$ mm) to a ~ 100 μm diameter

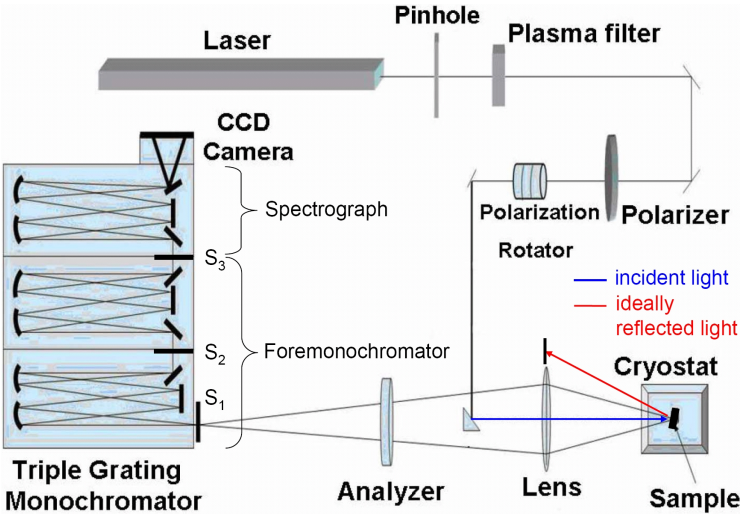

Figure 3.2: Optical path in "macro" setup for Raman light scattering. S_1, S_2, and S_3 indicate the entrance and intermediate slits, respectively.

spot on the sample surface. In order to avoid sample heating through the laser beam the incident power on the sample was kept below 10 mW. For measurements at low temperatures the samples were mounted in a vertical helium-flow cryostat as shown in figure 3.1. A temperature controller with a heater allowed an exact temperature setting. The lowest temperature provided by the "macro"-cryostat was 10 K. The samples were mounted on a copper holder at the end of a metallic sample rod. For different temperatures the samples were shifted vertically due to thermal length changes of the sample rod. In order to measure always at the same position, the Raman signal was monitored by a camera and the sample position was corrected if necessary. The cryostat was provided with optical suprasil glass windows. In order to avoid reflections from the glass, the cryostat was slightly rotated, similar to the sample for quasi-backscattering.

In contrast to light reflexion, where the direction of the reflected light is strongly limited by the direction of the incoming light and the angle to the scattering medium, having regard to surface roughness and bulk inhomogeneities, the inelastically scattered light is distributed in all directions. The part of the inelastically scattered light to be analyzed was collected by the same 40 mm-diameter lens, which was used before the scattering

process to focus the laser beam on the sample surface (see figure 3.2), now focusing on the entrance slit S_1 of the triple grating spectrometer.

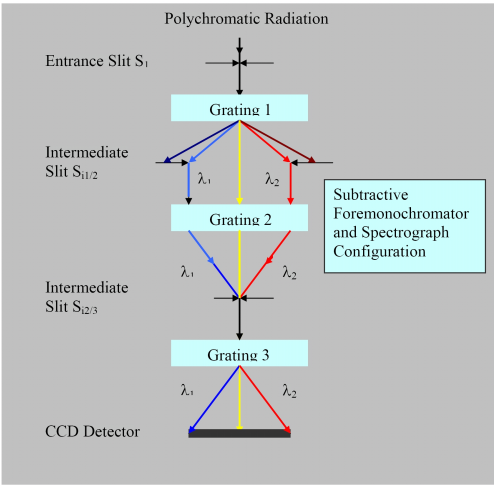

Figure 3.3: Optical diagram of DILOR XY triple grating spectrometer in subtractive foremonochromator and spectrograph configuration [Hor].

In order to select a particular polarization from the inelastically scattered light, a polarizing foil was used as analyzer. In order to yield highest Raman intensity, the samples were oriented in a way that the light entered the spectrometer in vertical direction (see appendix A). In spite of stray light reduction by pinholes and blocking the ideally reflected light by quasi-backscattering, the collected light still contains elastically scattered stray light at the energy of the incident laser light, e.g. due to rough sample surfaces. The corresponding Raman intensity is usually several orders of magnitude larger than the inelastically scattered Raman signal and therefore has to be suppressed. In the triple grating spectrometer the first two gratings can be used for stray light reduction (subtractive mode).

The triple grating spectrometer basically consisted of a series of three holographic gratings with 1800 lines/mm with two intermediate slits S_2 and S_3 in addition to the entrance slit S_1 (see figure 3.2). The three slits could be closed in vertical direction. In the present Raman study the triple grating spectrometer was exclusively used in the subtractive mode[1].

[1] In the additive mode the three gratings work as three coupled spectrographs, yield-

S_1	S_2	S_3
300 μm	2000 μm	300 μm

Table 3.2: Slit parameters for triple grating spectrometer.

Due to the finite size of the slits, physical signals exhibit a Gaussian broadening after detection. In the subtractive mode slit S_3 determined the resolution of the spectrometer [Dil]. Closing the slits increased the resolution at the expense of Raman intensity (see appendix A). Here, $S_1 = S_3 = 300$ μm was used (instrumental resolution ~ 4 cm^{-1} (FWHM)).

In the subtractive configuration (see figure 3.3) the first two gratings build the so-called foremonochromator, which works as a bandpass filter, while the last grating acts as spectrograph. The incoming polychromatic light is dispersed by the first grating and sent onto the intermediate slit S_2. By appropriate adjustment of the dispersed light relative to slit S_2, the slit cuts the major part of the elastically scattered light at the energy of the incident light, while allowing the inelastically scattered light with only slightly different energies to pass. In this way, for low stray light intensities an analysis of the Raman signal down to ~ 5 cm^{-1} is possible. The exact accessible measurement range, which is not overshadowed by residual stray light, depends on the studied sample, especially on the quality of the sample surface. After the intermediate slit S_2 the light is re-dispersed and sent onto the intermediate slit S_3. The last grating acts as spectrograph, which disperses the light on the detector. The dispersion angle is energy-dependent and increases for higher wavelengths, yielding a higher resolution in the red compared to the blue. For the detection of the Raman signal a charge-coupled device (CCD) camera with 2048×2048 pixels was used as multichannel detector. The partition of the different photon energies to the different CCD pixels determined the sampling rate of the optical signals. Note that the partition width is determined by the number of CCD pixels and the distance between slit S_3 and the CCD camera. A higher sampling rate of the "macro" setup compared to the "micro" setup was the main reason for the higher effective resolution[2]. In order to reduce the electronic noise, the CCD camera was nitrogen-cooled. Due to variations in the spectrometer adjustment by variations of the room temperature, a temperature-stabilizing air-conditioning system was used.

ing an enhanced resolution for a narrowed energy range (no stray light reduction).

[2]The "macro" and "micro" setups achieved sampling rates of ~ 2.1 points/cm^{-1} and ~ 0.6 points/cm^{-1} for 514.5 nm and 532.0 nm laser excitation, respectively.

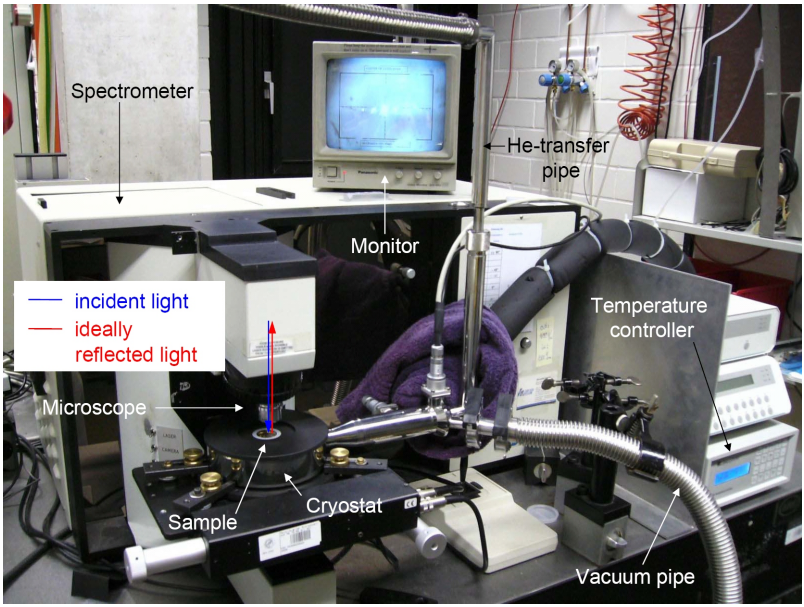

Figure 3.4: "Micro" setup for Raman light scattering.

3.2 "Micro"-Raman setup

The central unit of the "micro" setup was a JobinYvon LabRam single grating spectrometer. Figure 3.4 shows a picture of the "micro" setup in use. In this setup configuration the incident laser beam was focussed through an appropriate microscope objective on the sample surface. For the Raman experiments three different microscope objectives with different magnifications were available. For the objectives and corresponding approximate spot sizes see table 3.4. For excitation the 532.0 nm line of a frequency doubled Nd:YAG laser and the 632.8 nm line of a He^+/ Ne^+-mixed gas laser were used (see table 3.3). In order to avoid sample heating through the laser beam the incident laser power was kept below 1.5 mW.

Nd:YAG	532.0 nm
He^+/ Ne^+	632.8 nm

Table 3.3: Laser lines used in "micro" setup for Raman light scattering.

Objective	10x	20x	50x
Spot size	~ 15 μm	~ 8 μm	~ 3 μm

Table 3.4: Microscope objectives with corresponding spot size diameters at the focal length in "micro" setup for Raman light scattering.

In the "micro" setup the spectra were taken in an ideal backscattering geometry with the incident and reflected light parallel to the direction normal to the sample surface. In this way, both the reflected and scattered light was collected together by the same microscope objective, which was used before the scattering to focus the laser beam on the sample surface. The reflected and elastically scattered light was suppressed by the use of a razor edge filter. A polarizer and analyzer system comparable to the one used in the "macro" setup allowed symmetry dependent measurements. For excitation with the He^+/ Ne^+-mixed gas laser a plasma filter was added. After passing the entrance slight of the spectrograph, the inelastically scattered polychromatic light was dispersed by a single holographic grating with 1800 lines/mm. The diameter of the entrance slit S determined the resolution of the spectrometer. Here, S = 200 μm was used (instrumental resolution ~ 2 cm^{-1} (FWHM)). For the detection of the Raman signal a Peltier-cooled CCD camera was used. Due to the shorter optical path and the more focussed incident beam with smaller focal length compared to the triple grating spectrometer in the "macro" setup, the "micro" setup yielded a considerably higher Raman intensity. However, due to the use of the razor edge filter, the measured Raman spectra were cut below ~ 50 cm^{-1}, while stray light partly overshadowed the spectra for $\sim 50 - 100$ cm^{-1}, not allowing a detailed study of the low energy excitation range of $E < 100$ cm^{-1} with the "micro" setup.

For low-temperature measurements the samples were mounted on the cold finger of a horizontal helium-flow cryostat with an optical suprasil glass window. In order to provide a good thermal contact, the samples were fixed with silver paste. A temperature controller with a heater allowed an exact temperature setting. The lowest achievable temperature was ~ 5 K. Due to the horizontal orientation of the samples, thermally induced length changes of the sample holder did not result in substantial movements of the samples perpendicular to the incident light. The exact focus of the laser beam in vertical direction was corrected for different temperatures. The focus and measuring position were controlled by a camera.

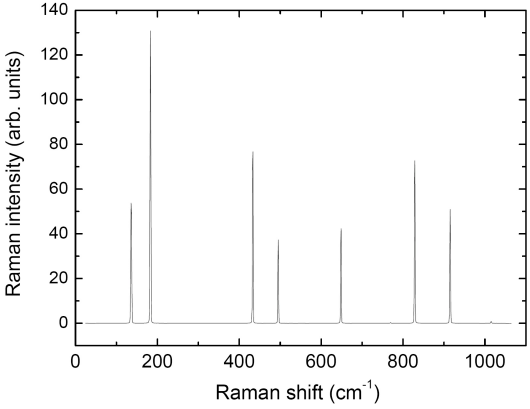

Figure 3.5: Neon calibration spectrum for 0 $cm^{-1} \mathrel{\widehat{=}} 632.8$ nm.

3.3 Data analysis

3.3.1 Data acquisition

For each Raman spectrum an additional calibration spectrum of a nearby argon or neon line was measured in order to determine the precise frequency and linewidth of the different phonons in the studied samples. Figure 3.5 shows a neon calibration spectrum for 0 $cm^{-1} \mathrel{\widehat{=}} 632.8$ nm. Due to variations in the room temperature, which affect the adjustment of the spectrometer, the measured frequencies can shift non-intrinsically in time. However, the sharp argon and neon lines are precisely documented in literature [Cro72]. By comparing the experimentally determined positions of the lines with the documented frequencies, these variations can be re-corrected. By averaging over calibration spectra before and after a Raman scan the correcting precision was enhanced. In order to avoid random frequency shifts due to different positioning of the calibration lamps[3], the lamps were fixed at the same position within a series of Raman scans.

Like all experimental quantities the Raman signal is affected by white statistical noise. In order to reduce the noise in a Raman spectrum, the scattered light was collected and averaged over a certain measuring time t.

[3]Different positioning of the calibration lamps leads to a different zig-zag of the collected light inside the spectrometer, incorrectly pretending a frequency shift.

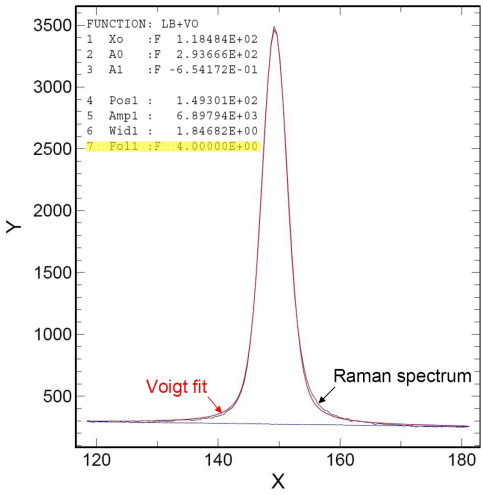

Figure 3.6: Phonon mode (see text for details) fitted to a Voigt profile (X = Raman shift (cm^{-1}), Y = Raman intensity (arb. units). FOL1 indicates the Gaussian folding width corresponding to the spectrometer resolution.

According to the theory of statistical physics, one has [Dem08]

$$\text{Noise} \sim \frac{1}{\sqrt{t}}.$$

Raman spectra typically show additional spikes, due to cosmic rays or natural radioactivity. In order to suppress the spikes, the total measuring time was split in a number of independent accumulations of shorter time.

3.3.2 Fitting

For fitting the in-house software `DATLAB` was used. In the absence of Fano-like asymmetries, the phonon peaks were fitted to Voigt profiles, which result from a convolution of symmetric Lorentzian phonon line shapes with the Gaussian shaped instrumental resolution, according to the relation

$$y(x) = \int_{-\infty}^{\infty} g_n(\tau) \cdot f(x-\tau) d\tau,$$

where $f(x)$ and $g(x)$ represent the Lorentzian and Gaussian profiles, respectively, yielding the broadened Voigt profile $y(x)$. Figure 3.6 shows a

Cu_2O mode obtained from a slightly underdoped LCCO film (see chapter 4.1) fitted to a Voigt profile. FOL1 indicates the Gaussian folding width corresponding to the spectrometer resolution. Since the argon and neon calibration lines exhibit intrinsic symmetric Lorentzian lineshapes with very small linewidths, their experimental lineshapes are dominated by the Gaussian broadening. As a consequence, the calibration lines were fitted to pure Gaussians, yielding a measure of the spectrometer resolution.

In order to obtain a reliable comparison of different Raman spectra within a series of scans, e.g. at different temperatures, the folding width was kept constant. In addition, constant or similar background sections of the Raman spectra were selected. The integrated intensity of a phonon fitted to a Voigt profile was estimated by $I = \text{Amplitude} \times \text{FWHM}$[4].

3.4 Experimental errors

In the following all relevant experimental errors, which appeared during the Raman experiments, are listed. The combinations of the different errors were the basis for the estimated error bars in the experimental results.

- Lower limit for the error bars in frequency, FWHM, and integrated intensity of optical modes given by `DATLAB` fitting errors
- Shifts in energy due to thermally induced spectrometer drift ~ 0.2 cm^{-1} (mainly corrected by argon and neon calibration spectra)
- Fluctuations in phonon intensity for different temperatures mainly due to slight variations in measuring position and focus $\sim 5 - 10\%$ (strongly sample dependent)
- Estimated error for the temperature determination ~ 1 K
- Possible sample heating through the laser beam ~ 5 K (if sample heating was observed, the temperature was corrected)

[4] For a pure Gaussian profile this estimation is exact up to a constant factor.

Chapter 4

Studied materials

4.1 Epitaxial films of the electron-doped cuprate superconductor $La_{2-x}Ce_xCuO_4$

4.1.1 General aspects of electron-doped cuprates

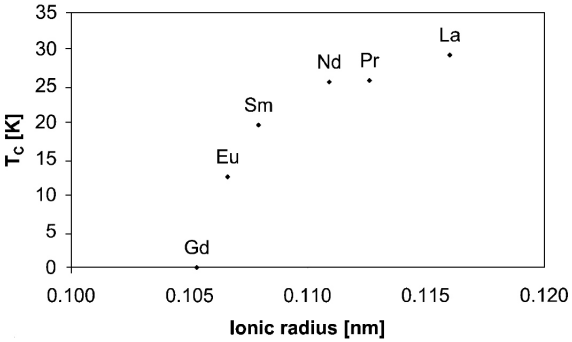

Figure 4.1: Superconducting transition temperatures T_c for different lanthanide rare earth substitutions (Ln) in $Ln_{2-x}Ce_xCuO_4$ [Nai00].

The main series of electron-doped cuprate superconductors has the general chemical formula $Ln_{2-x}Ce_xCuO_4$, where Ln = La, Pr, Nd, Sm or Eu [Tsu05]. The compounds with the larger lanthanide (Ln) ions ex-

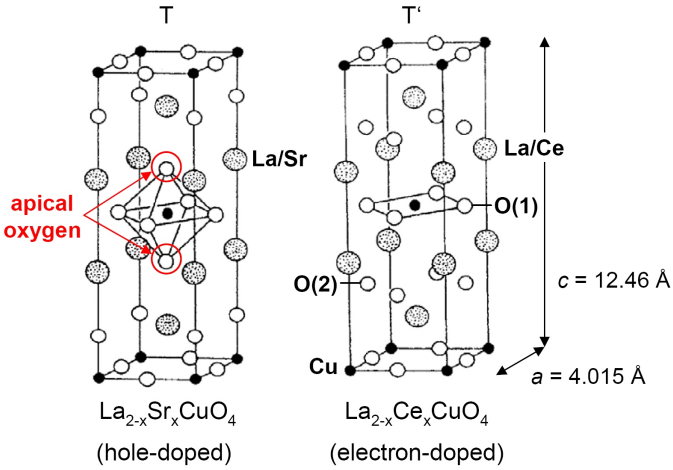

Figure 4.2: T-structure of LSCO and T'-structure of LCCO [Tok89]. (a and c are the lattice constants of LCCO at optimal doping, O(1) and O(2) mark different crystallographic positions of oxygen in the unit cell.)

hibit the higher superconducting transition temperatures T_c, as shown in figure 4.1. $La_{2-x}Ce_xCuO_4$ (LCCO) exhibits the highest critical temperature among this series of electron-doped cuprate superconductors with $T_c^{max} \sim 30$ K [Nai00, Kro08]. Electron-doping is induced by substitution of La^{3+} for Ce^{4+}, which introduces electrons into the CuO_2 planes [Tak89]. LCCO crystalizes in the so-called T'-structure, which does not include apical oxygen ions, in contrast to the T-structure of the hole-doped counterparts of the Ln_2CuO_4 family, like e.g. $La_{2-x}Sr_xCuO_4$ (LSCO) or $Ba_{2-x}Sr_xCuO_4$ (BSCO) [Nai00]. The T-structure of hole-doped LSCO and the T'-structure of electron-doped LCCO are shown in figure 4.2. Both structures are layered perovskites with one CuO_2 layer per unit cell. The single CuO_2 plaquets are oriented in a corner-sharing configuration. The interlayers serve as charge carrier reservoirs and donators for the CuO_2 layers, stabilizing the crystal structure. The crystallographic ground state of both structures is tetragonal with space group $I4/mmm(D_{4h}^{17})$ [Tho91].

The stability of the T'-structure depends strongly on the radius of the lanthanide ions [Nai00]. For larger lanthanide radii the T'-structure is increasingly affected by strain, leading to a boundary for a stable T'-structure between La and Pr [Nai00]. Thus, the T'-structure of LCCO

is unstable in bulk form[1], but can be stabilized by epitaxial growth on $SrTiO_3$ (STO) substrates [Nai00]. Due to a significant lattice mismatch between STO ($a = 3.905$ Å) and T-La_2CuO_4 ($a \sim 3.8$ Å), epitaxial growth of La_2CuO_4 on STO suppresses the T-structure and favors the better matching T'-structure ($a = 4.015$ Å for optimally doped LCCO) [Nai00], where a denotes the corresponding in-plane lattice constants. The out-of-plane lattice constant c of LCCO decreases monotonically for increasing Ce doping, while a stays more or less constant [Nai00]. Depending on the growth conditions, LCCO films on STO substrates can also crystallize in the T-structure for $x \lesssim 0.6$ [Nai02], but superconductivity is observed only in the T'-structure [Nai02, Tsu06]. Due to a large difference of c for T ($c \sim 13.15$ Å) and T' ($c = 12.46$ Å at optimal doping) at room temperature, c can be used easily for phase identification [Nai00, Tsu02]. While the T-structure is susceptible to orthorhombic distortions, no structural instability is reported for LCCO. However, for compounds with heavier lanthanides (Eu and higher) the T'-structure becomes also increasingly affected by lattice instabilities [Alv96, Vig97], e.g. Eu_2CuO_4 shows a structural distortion from tetragonal to orthorhombic at ~ 170 K [Vig97].

The electron-doped cuprates show a complex materials physics. It has been found, for instance, that an elaborate annealing process under reducing conditions during crystal growth is essential to stabilize superconductivity in the T'-structure [Tok89, Arm09]. The annealing is believed to remove interstitial apical oxygen [Nai00], i.e. T-structure residuals that serve as additional hole-dopants for the CuO_2-planes [Tsu02]. The interplay of electron- and hole-doping appears to be complicated. It has been shown, for instance, that higher electron-doping via higher Ce concentrations cannot compensate for excess oxygen [Arm09]. In addition, the T'-structure is susceptible to further microstructural inhomogeneities. The annealing procedure in bulk single crystals of $Nd_{2-x}Ce_xCuO_4$ (NCCO), one of the most widely studied electron-doped cuprates, generates a small amount of an epitaxially intergrown impurity phase [Man04]. Similar observations have been reported for some epitaxial thin films of $Pr_{2-x}Ce_xCuO_4$ (PCCO) grown by pulsed-laser deposition [Rob09]. Recent muon spin rotation (μSR) experiments on NCCO films indicate that the crystallographic top layers of the films tend to form an oxidized AFM secondary phase [Lue]. Furthermore, wide variations in the transport characteris-

[1] Superconducting T'-LCCO bulk material was only found in a quasi-stable configuration for a very limited doping-range with poor crystallinity and a broad superconducting transition at T_c, stabilized by the smaller Ce^{4+} ions compared to La^{3+} [Yam94].

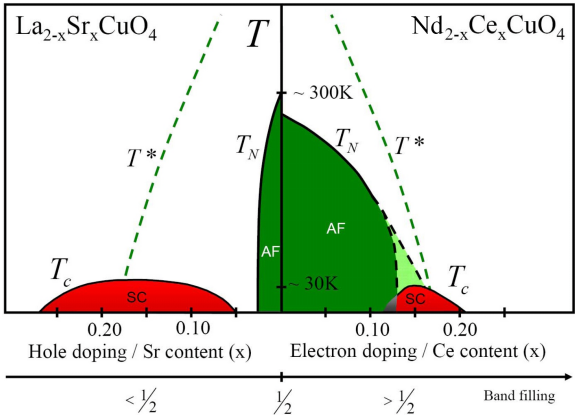

Figure 4.3: Joint phase diagram of hole-doped LSCO and electron-doped NCCO. The light green area reflects the uncertainty in the extent of the AFM phase and the possible coexistence with superconductivity [Arm09]. (T_N and T^* indicate the Néel temperature and the approximate extent of the pseudogap phase on both sides of the phase diagram, respectively.)

tics of thin films of closely related or even nominally identical materials [Dag07, Wag08b, Mül06] also suggest, at least partly, a possible microstructural origin. As an advantage for studies on LCCO compared to other electron-doped cuprates, the lanthanide ion Ln = La is non-magnetic.

The phase diagrams of electron-doped NCCO and hole-doped LSCO are shown in figure 4.3. Central features of both kinds of doping are an AFM phase, which gets continuously suppressed for increasing doping level, while superconductivity can emerge at low temperatures. The AFM order is induced by superexchange interactions of the static Cu^{2+} spins via fully occupied O^{2-} orbitals [And87]. The most striking difference between the electron- and hole-doped cuprates is an asymmetry of their phase diagrams with respect to zero doping. On the hole-doped side the superconducting phase exhibits a broad dome-like shape with no overlap to the AFM phase, which gets suppressed within $x \sim 0.02$. The electron-doped cuprate superconductors of the LCCO type exhibit a substantially lower maximum transition temperature $T_c^{max} \lesssim 30$ K (see figure 4.2) and a narrower doping range of superconductivity than their hole-doped counterparts (e.g. $YBa_2Cu_3O_7$ with $T_c \sim 93$ K). The AFM phase in the electron-doped compounds seems to be more robust with respect to doping and ex-

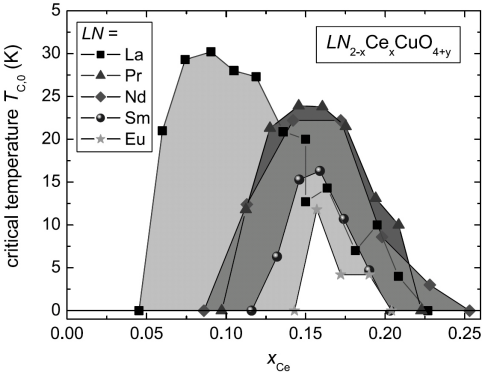

Figure 4.4: Critical temperatures as function of doping for electron-doped cuprate superconductors of chemical formula $Ln_{2-x}Ce_xCuO_4$ [Tsu05].

hibits probably at least a small area of coexistence with superconductivity as indicated by the grey area in figure 4.3. Note that in a recent theoretical study the differences between hole- and electron-doping have been attributed to differences in the electronic correlation strengths [Web10]. On the other hand, an oxidized AFM secondary phase at the crystallographic top layers, as observed in NCCO films, might mimic a broadened AFM phase in the phase diagram of the electron-doped cuprates [Lue].

For both kinds of doping the normal state is characterized by an anomalous metallic and probably non-Fermi liquid state around optimal doping. One of the best known properties of this anomalous state is a linear temperature dependence of the electrical resistivity $\rho(T)$ found in many hole-doped cuprates near optimal doping [Arm09]. Note that for a conventional metal one has $\rho(T) \sim T^2$ [Arm09]. In contrast to the hole-doped compounds, most electron-doped cuprates show a quadratic behavior of $\rho(T)$ over an anomalously wide temperature range near optimal doping [Arm09]. T^* denotes the onset of the so-called "pseudogap", which describes a variety of partial spectral weight reductions in excitation spectra that have been partly associated to antiferromagnetism [Arm09]. The origin of the "pseudogap" phenomena is still highly debated and might be different for the electron- and hole-doped cuprates. In the electron-doped cuprates one has to distinguish between a low-energy "pseudogap" of the order of the superconducting gap Δ [Dag05] and a high-energy "pseudogap" Δ^* that extends over a wider energy range at considerably higher energies, as found

by angle-resolved photoemission spectroscopy (ARPES) [Arm01, Mat07] and optical spectroscopy [Ono01, Zim05] on underdoped NCCO. Both T^* and the magnitude of Δ^* were found to decrease with increasing doping level [Mat07, Dag05], cutting the superconducting phase close to optimal doping [Zim05]. In the superconducting regime of NCCO, $\Delta^* \sim 100$ meV $\gg \Delta$ [Mat07]. It is under discussion, if the pseudogap is a precursor to superconductivity [Nor05] or represents a second competing order parameter [Alf03].

Figure 4.4 shows the critical temperatures of the main series of electron-doped cuprate superconductors $Ln_{2-x}Ce_xCuO_4$ (Ln = La, Pr, Nd, Sm, Eu) as a function of doping. Note that the superconducting gap in the electron-doped cuprate superconductors has a predominant $d_{x^2-y^2}$-wave symmetry with the gap maxima shifted to the nodal directions compared to hole-doping [Mat05, Blu02]. The superconducting state in LCCO is stable over a wider doping range ($0.05 < x < 0.22$) than in the other electron-doped compounds, like e.g. NCCO, with a strong T_c-increase upon underdoping. The maximum transition temperature ($T_c^{max} \sim 30$ K) is found at the lower doping level $x \sim 0.09$ compared to $x \sim 0.15$ for NCCO [Kro08, Tsu05, Saw02]. For comparison, optimal doping in hole-doped LSCO was also found at $x \sim 0.15$ [Yam98]. For compounds with smaller lanthanide ions the doping range of the superconducting phase becomes increasingly smaller, while the maximal T_c decreases [Kro08].

4.1.2 Sample characterization

Name	**x**	**STO**	**k**	T_{red}	t_{red}	T_c
315S	~ 0.08	bicrystal	~ 0.53	578 K	100 min	~ 29 K
501T	~ 0.1	tetracrystal	$\gtrsim 0.5$	559 K	90 min	~ 27 K

Table 4.1: Studied LCCO samples. (STO = corresponding $SrTiO_3$ substrates (see text for details), cation ratio k = $Cu^{2+}/(La^{3+}+Ce^{4+})$, T_{red} = annealing temperature, t_{red} = annealing time (according to [Wag08a]).)

In table 4.1 the two superconducting electron-doped LCCO films, which have been used for the Raman experiments, are listed with their characterizing parameters T_c and Ce concentration x. Both films had been the basis of prior transport experiments [Wag08a, Wag08b, Mül06]. For comparison the previously used sample names are added. Both films had

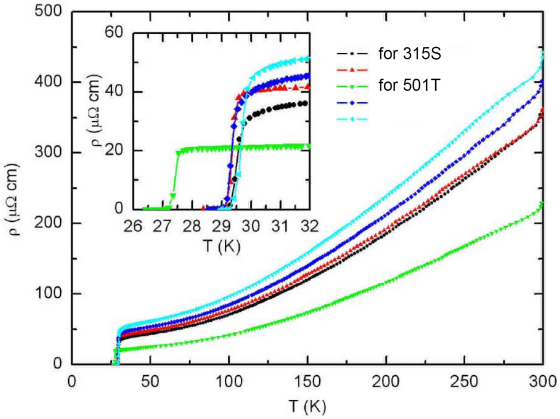

Figure 4.5: Electrical resistivity vs. temperature characteristics of LCCO test films [Wag08a]. The black and green curves correspond to samples with identical growth conditions as used for the films 315S and 501T, respectively. (The three red and blue curves correspond to further slightly underdoped LCCO films that have not been used for Raman experiments.)

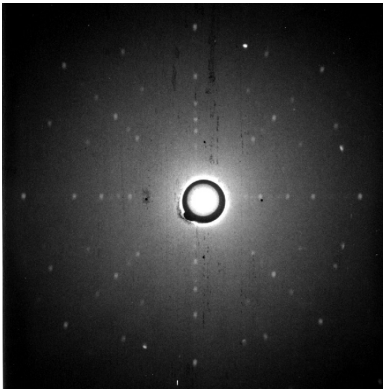

Figure 4.6: Laue XRD image of oriented sample 315S.

a thickness of $\sim$ 900 nm. The films had been deposited epitaxially on quadratic (001)-oriented $SrTiO_3$ (STO) substrates (edge length = 10 mm, thickness = 1mm), yielding c-axis oriented films, in two independent fabrication runs using MBE from ultrapure metal sources, as described elsewhere [Wag08a, Nai00]. Finally, both films were annealed in vacuum at 578°C for 100 minutes and 559°C for 90 minutes, respectively, in order to remove residual apical oxygen [Wag08a]. A STO bicrystal and a STO tetracrystal were used as film substrates, respectively. The bicrystal was formed by a symmetric 24° *tilt*-grain boundary with the tilt axis along the (001)-direction (see figure 4.7). The tetracrystal contained three similar 30° grain boundaries (for the film geometry see [Che03]). The use of non-single-crystalline substrates was due to the prior use of the LCCO films for transport measurements. Via the epitaxial growth of LCCO on STO, the grain boundaries in the STO substrates were transmitted to the LCCO films [Wag08a]. The purpose of this transmittance was to create Josephson grain boundary junctions. For the Raman measurements LCCO film areas away from the grain boundaries with well-defined crystal axes were used.

The Ce concentrations in the LCCO films were adjusted to $x \sim 0.08$ (corresponding to electron concentrations slightly less than optimum doping) and $x \sim 0.1$ (slightly overdoped) by exact control of the gas flux rates and use of inductively coupled plasma - atomic emission spectroscopy (ICP-AES) [Wag08b, Gre01]. The slightly under- and overdoped samples exhibited cation ratios k = $Cu^{2+}/(La^{3+}+Ce^{4+})$ of $\sim$ 0.53 and $\gtrsim$ 0.5, respectively [Wag]. Note that the highest superconducting transition temperatures T_c in LCCO films for optimal doping were achieved with a slight excess of copper (copper rich films) [Wag08a]. Electrical resistivity measurements on LCCO test films, which had been fabricated under identical growth conditions, revealed $T_c \sim$ 29 K and 27 K, respectively [Wag08a] (see figure 4.5). The widths of the resistive transitions at T_c were below 1 K for both films. After growth, the quality of the films had been examined by standard X-ray diffraction (XRD) [Wag08a]. XRD intensity plots with linear scaling suggested a T'-single phase for both films [Wag08a]. A detailed XRD refinement analysis of the LCCO films is shown in chapter 5.1.1. For sample orientation Laue XRD was used (see figure 4.6).

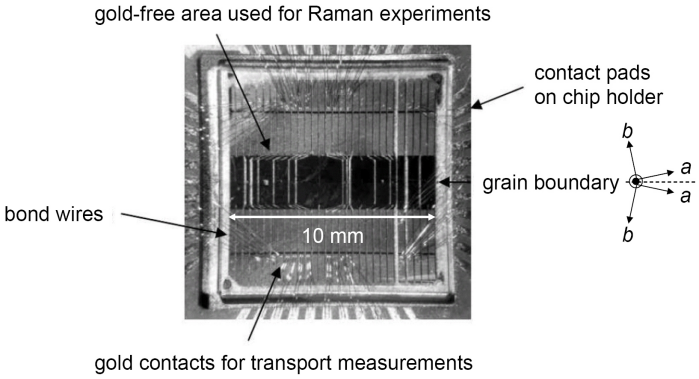

Figure 4.7: Microstructured LCCO film comparable to sample 315S in chip holder ready for grain boundary tunneling experiments. (a and b indicate the in-plane crystal axes on both sides of the grain boundary.)

Details about LCCO film geometries

In order to use the LCCO films for transport experiments, they were microstructured to superconducting-quantum-interference-devices (SQUIDs) with different geometries by photolithography [Wag08a, Mül06]. Figure 5.1.1 shows a microstructured LCCO film comparable to sample 315S ready for transport experiments. As shown previously [Mül06], the grain boundaries in the LCCO films act as Josephson junctions that can be used for transport tunneling experiments. For the transmittance of the desired structures to the LCCO films, non-focussed argon-ion-etching was used. Due to short junction problems during the photolithography process [Mül06], the lithography procedure was repeated 1-2 times, yielding step-like film edges close to the structures in the film area. In the central areas of the LCCO films, which contain the grain boundaries, a gold top layer was removed. Gold contacts on top of the LCCO films on both sides of the grain boundaries were used for 4-point-measurements. The gold-free areas away from the grain boundaries were used for the Raman experiments.

4.2 $R_{1-x}K_xFe_2As_2$ (R = Ba, Sr) and and $Ba(Fe_{1-x}Co_x)_2As_2$

4.2.1 General aspects of pnictide superconductors

The iron-based superconductors exhibit four main classes of crystal structures typified by LaOFeAs (1111), $BaFe_2As_2$ (122), LiFeAs (111), and FeTe (11). All classes are layered materials with corner-sharing square-planar sheets of Fe^{2+} as common structural element, very similar to the Cu^{2+} squares within the CuO_2 planes in the cuprates. The group of iron-based pnictides divides into the oxypnictides (1111), containing oxygen atoms, and the ternary iron arsenides (122) without oxygen. Historically, after first reports on $LaO_{1-x}F_xFeAs$ with critical temperatures of $T_c = 26$ K [Kam08] and 43 K under pressure [Tak08], the transition temperatures raised quickly up to 56 K in related compounds [Wan08, Wu09b]. LaOFeAs crystallizes in the ZrCuSiAs-type crystal structure (structure on the left in figure 4.8) consisting of alternating LaO^+ and $FeAs^-$ layers with two $FeAs^-$ layer per unit cell. In LaOFeAs, superconductivity is usually induced by substitution of F^- for O^{2-}, introducing electrons into the $FeAs^-$ layers. It was recently shown that hole doping by substitution of La^{3+} for Sr^{2+} can also induce superconductivity, showing a $T_c = 25$ K [Wen08].

More recently the second class of pnictide superconductors, crystallizing in the $ThCr_2Si_2$-type crystal structure with identical $FeAs^-$ layers (2/unit cell) compared to the (1111) compounds, were discovered (structure on the right in figure 4.8) [Rot08b]. The ternary iron arsenide $BaFe_2As_2$ (BFA) becomes superconducting after substitution of K^+ for Ba^{2+} with $T_c = 38$ K at optimal doping $x \sim 0.4$–0.5 [Rot08b, Che09c]. This system is a hole-doped superconductor. Isostructural compounds with Ca ($T_c = 20$ K) [Wu08], Eu ($T_c = 32$ K) [Jee08], and Sr ($T_c \sim 38$ K) [Che08, Saw08] instead of Ba followed soon thereafter. A first example of electron doping in a ternary iron arsenide was achieved by substitution of Co^{3+} for Fe^{2+} in $BaFe_2As_2$ with $T_c = 22$ K [Sef08]. In contrast to the oxypnictides, large high-quality single crystals are available for the ternary iron arsenides.

The $ThCr_2Si_2$-type crystal structure is tetragonal at room temperature with space group I4/mmm (D_{4h}^{17}) [Roz81]. Central structural units are the quasi-two-dimensional $FeAs^-$-sheets, controlling the magnetic and superconducting properties of the system [Maz09]. Thereby, Fe^{2+} and As^{3-} form a tetrahedron, where As^{3-} is located in the center of the Fe^{2+}-squares, alternately shifted above and below along c-direction [Kre08]. As

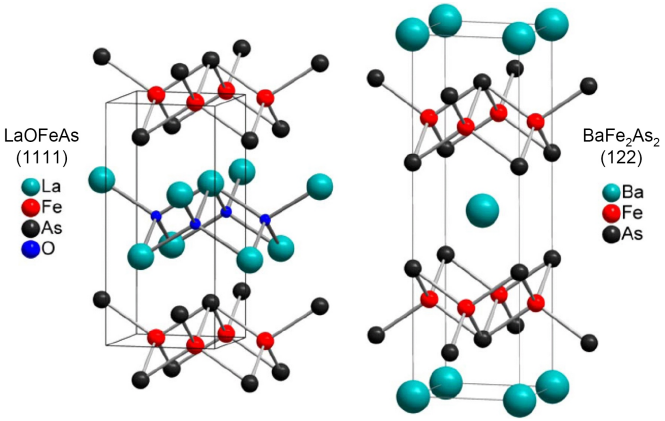

Figure 4.8: Crystal structures of LaOFeAs and $BaFe_2As_2$ [Teg08].

a consequence, the direct Fe-Fe exchange interaction is enhanced [Yil09a]. The FeAs-sheets are very similar to the Cu_2O planes in the cuprates, but exhibit a little more three-dimensional character. It was found that the As-Fe-As bond angle in the pnictides systematically decreases with doping, i.e. the distance between Fe^{2+} decreases while the tetrahedra are elongated along c-direction, showing highest T_c for the ideal tetrahedral angle of 109.5° [Rot08a]. This observation reflects a very sensitive interplay between the lattice and the electronic properties. Moreover, the exact c-axis position of As^{3-} controls the interactions between the Fe^{2+} ions and appears to be crucial for the magnetic properties [Yil09a]. Note that the spins being essential for the magnetic properties in the iron-based superconductors come from the Fe^{2+} sites [Hua08]. At the moment it is under discussion, if the spins show Pauli-paramagnetism (itinerant picture) at room temperature [Rot08b] or are more localized to the Fe sites [Bro10].

Figure 4.9 shows the phase diagram of $Ba_{1-x}K_xFe_2As_2$ (BKFA). The phase diagrams of the ternary iron arsenides and the oxypnictides appear to be very similar. Common features of the undoped ternary iron arsenide parent compounds are a structural phase transition from the high-temperature tetragonal to a low-temperature orthorhombic phase (space group Fmmm [Rot08c]) and a transition to a commensurate AFM spin-density wave (SDW) order [Hua08]. The structural transition was found to be induced by the magnetic ordering [Yil09a]. As shown by several

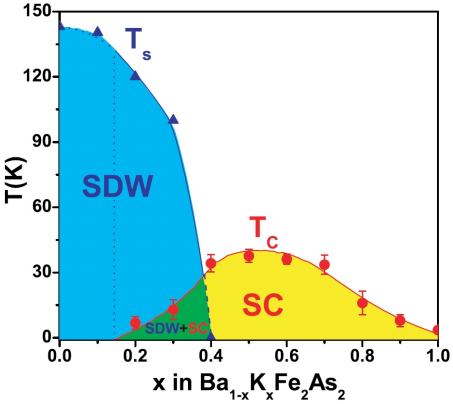

Figure 4.9: Phase diagram of BKFA [Che09c]. T_s denotes the transition temperature of a combined structural and SDW transition. The green color signifies an area, where the SDW and superconductivity (SC) coexist.

authors, the structural transition in the ternary iron arsenides tends to be of first order [Hua08, Ni08, Kre08]. However, there are also some reports about a more second-order-like behavior, e.g. in BFA [Rot08c, Wil09].

The SDW order is an AFM many-body ground state of metals [Dre08], that sets in below a temperature T_s, where the density of "itinerant" charge carriers with spin $\uparrow$ or $\downarrow$ exhibits a sinusoidal modulation according to

$$\rho_{\uparrow,\downarrow}(\mathbf{r}) = \frac{1}{2}\rho_0(\mathbf{r})[1 \pm \sigma_0 \cos(\mathbf{Q} \times \mathbf{r})],$$

where $\mathbf{r}$ is a vector in real space, σ_0 is the amplitude, and $\mathbf{Q}$ the wavevector of the SDW. Note that in the iron pnictides the modulated spin density might be localized around the Fe sites [Lee10, Bro10]. In general, the wavelength of the SDW $\lambda = 2\pi/\mathbf{Q}$ is incommensurate with the lattice parameters. For the iron pnictides two different models for the SDW order are under discussion. While in a fully itinerant picture the magnetic order results from a nesting between hole and electron Fermi surfaces [Don08], a local superexchange mechanism considering a competition between nearest and next-nearest neighbor interaction, via the off-plane As^{3-} ions, provides an alternative explanation [Yil09a]. In figure 4.10b the magnetic structure of undoped BFA, as determined from neutron scattering, is shown [Hua08]. The SDW order shows a commensurate collinear stripe-type spin configuration with the iron magnetic moments aligned antiferromagnetically along

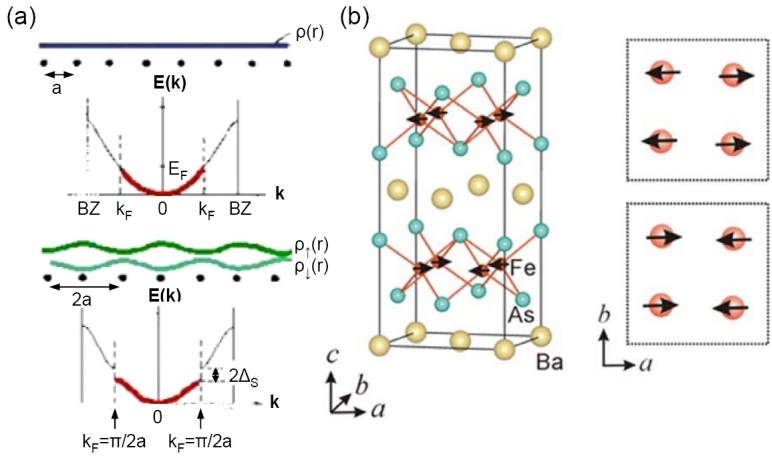

Figure 4.10: (a) Cartoon of a spin-Peierls transition in 1D [Dre08]: A sinusoidal spin modulation inside a half-filled electronic band with periodicity $2a$ (green lines) implies an additional periodicity inside the Brillouin zone (BZ) with periodicity $\pi/2a$, leading to band crossings (degeneracy) at $k_F = \pi/2a$. This degeneracy is lifted by the formation of electronic bandgaps $2\Delta_S$ at the Fermi energy E_F; (b) magnetic structure of the SDW state in undoped BFA as determined from neutron scattering [Hua08].

the a and c axes, and ferromagnetically along the b axis [Hua08]. The spatial modulation of the electron spin density implies an additional superstructure, which leads to an opening of a SDW gap at E_F, that largely affects the Fermi surface [Hu08]. The SDW order can be regarded as "3D analog" to a Peierls transition in 1D (see figure 4.10a), where a gap in the electronic density of states is formed by repulsion of crossing bands (lifting degeneracy) inside the Brillouin zone due to additional periodicity.

While for electron-doped LaOFeAs and $Ba(Fe_{1-x}Co_x)_2As_2$ (BFCoA) the structural and SDW phase transitions were found at slightly different temperatures with $T_{structural} > T_{SDW}$ [Lue09, Les09], they seem to appear at a same temperature T_s in hole-doped BKFA [Che09c]. A similar behavior is expected for $Sr_{1-x}K_xFe_2As_2$ (SKFA). Undoped BFA and $SrFe_2As_2$ (SFA) show both transitions at $T_s \sim 140$ K and $T_s \sim 203$ K, respectively [Rot08c, Teg08, Sun09]. Doping with electrons or holes suppresses $T_{SDW,s}$ and induces superconductivity at low temperatures. Note that the superconducting gap in the iron-based superconductors seems to have

an extended $s^{\pm}$-wave symmetry [Maz09]. At the moment it is under discussion, if doping is essential for superconductivity to provide optimal charge carrier concentrations inside the $FeAs^{-}$ sheets or is just important to suppress the SDW order [Mit09]. Note that in hole-doped BKFA the doping substitution appears between and in electron-doped BFCoA inside the Fe^{2+}-sheets. Isovalent substitution of P^{3-} for As^{3-} in $BaFe_2As_2$ (no change of charge carrier concentration) induces superconductivity up to 30 K [Jia09]. In hole-doped RFe_2As_2 (R = Ba, Sr) strong indications exist for a distinct doping range where the superconducting and SDW phases coexist. In the coexistence regime of underdoped BKFA, there is evidence for a weaker structural transition at T_s without macroscopic change in the crystal symmetry, but with an increase in microstrains that was attributed to a magnetically induced lattice softening in combination with electronic phase separation [Ino09]. Magnetic fluctuation are present also in superconducting samples that do not exhibit SDW order [Lyn09].

4.2.2 Sample characterization

Batch	**Sample**	**Flux**	**x**	T_c	$T_{\mathrm{SDW},s}$
G12	$SrFe_2As_2$	Sn	-	-	$\sim$ 202 K
G30	$BaFe_2As_2$	self	-	-	$\sim$ 138 K
G23	$BaFe_2As_2$	Sn	-	-	"$\sim$ 100 K"
G15	$Sr_{1-x}K_xFe_xAs_2$	Sn	$\sim$ 0.15	$\sim$ 29 K	$\sim$ 178 K
G07	$Ba_{1-x}K_xFe_xAs_2$	Sn	$\sim$ 0.28	$\sim$ 29 K	$\sim$ 75 K
G41	$Ba_{1-x}K_xFe_xAs_2$	self	$\sim$ 0.32	$\sim$ 38.5 K	-
G53	$Ba_{1-x}K_xFe_xAs_2$	self	$\sim$ 0.32	$\sim$ 38.5 K	-
G64	$BaFe_{2-x}Co_xAs_2$	self	$\sim$ 0.08	$\sim$ 5 K	$\sim$ 109 K
G33	$BaFe_{2-x}Co_xAs_2$	self	$\sim$ 0.13	$\sim$ 25 K	-

Table 4.2: Studied ternary iron arsenide samples. (G12, G30, G23 = undoped; G15, G07 = underdoped; G41, G53 = optimally doped; G64 and G33 = underdoped and optimally doped, respectively.)

In table 4.2 the different superconducting and non-superconducting ternary iron arsenide samples, which have been used for the Raman experiments, are listed together with their characterizing parameters T_c, $T_{\mathrm{SDW},s}$, and doping concentration x. For comparison the previously used internal batch numbers are added. All samples had been grown by the flux-growth

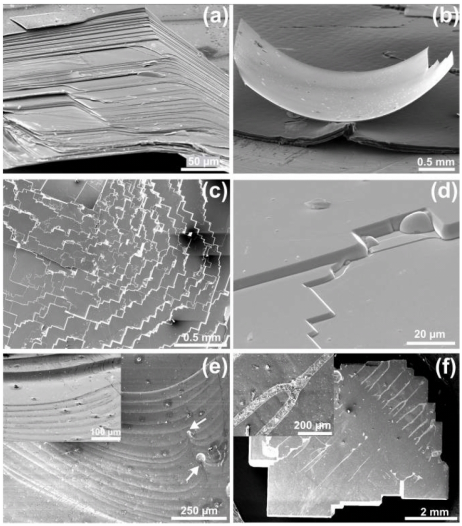

Figure 4.11: Composition of characteristic SEM images of ternary iron arsenide samples, showing (a) multilayer steps, (b) a winded sheet of a single crystal, (c)+(d) macrosteps, and (e)+(f) tin inclusions [Sun09].

method using tin flux or self-flux as described in [Wan09, Sun09, Par09]. Figure 4.11 shows a composition of characteristic scanning-electron-microscopy (SEM) images, taken from test samples out of the different batches. All samples exhibited a thin platelet-like morphology. As typical crystal habit, they showed multilayer steps, winded shapes of single crystal sheets, and macrosteps [Sun09]. In case of tin flux growth, tin inclusions were present, in particular between different layers. The experiments were performed on thin platelet-like single crystals with the crystallographic c-axis perpendicular to the plane surface. The typical sample dimensions were $\sim 1-2$ mm in-plane with a thickness of $\sim 20-50$ μm. Straight edges along the in-plane crystal axes provided ideal lines for sample orientation. The average chemical composition was determined by energy-dispersive X-ray (EDX) and inductively coupled plasma spectroscopy, respectively. The error bars of the averaged doping concentrations were $\gtrsim 10$ %.

The superconducting transition temperature T_c and the transition temperatures of the structural and SDW transitions in the different ternary iron arsenide samples were determined for the main part by a decrease in

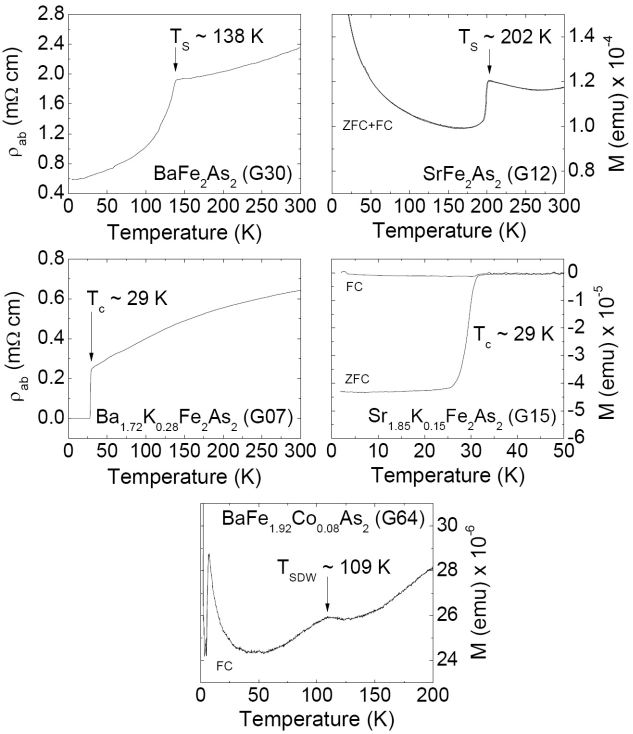

Figure 4.12: In-plane resistivity of BFA and BKFA single crystals determined by standard four-probe method and field-cooled (FC) and zero-field-cooled (ZFC) magnetization (M) of SFA, SKFA, and BFCoA in magnetic fields of 10 kOe, 10 Oe, and 5 kOe applied along the crystallographic c-axis.

the in-plane resistivity ρ_{ab} and the magnetization M, respectively, according to previous experiments [Rot08c, Sun09, dlC08]. Thereby, the decrease in the magnetization at the SDW transition is explained by the AFM ordering. Note that a corresponding decrease in the resistivity in LaOFeAs was first attributed to the SDW transition [Don08], while it was later attributed to the structural transition [dlC08]. Figure 4.12 shows a selection of characterization measurements on non-superconducting BFA (G30) and SFA (G12) and superconducting BKFA (G07), SKFA (G15), and BFCoA (G64) samples. For BKFA (G07) the SDW transition temperature T_s was determined by neutron-scattering and muon-spin-rotation experiments on samples from the same batch [Par09]. For further characterization measurements of the studied samples see [Sun09, Sun, Par]. The characterization measurements on BFA (G30), SFA (G12), BKFA (G07), SKFA (G15), and BFCoA (G33) were carried out on samples from the same batches as used for the Raman experiments, while for BFCoA (G64) the identical sample was used. For BFA (G30) and SFA (G12) the anomalous decreases in ρ_{ab} and M were observed at identical temperatures [Sun09], suggesting combined structural-SDW transitions at T_s. In optimally doped BKFA and BFCoA the structural and SDW transitions are suppressed.

A recent report on undoped BFA pointed out that T_s depends on the solvent used for flux-growth and can shift to lower temperatures for tin flux growth compared to self-flux growth [Sun09]. The exact temperature shift apparently depends on the local tin concentration. Since resistivity and magnetization measurements are averaging over the whole sample, these techniques can not give a precise local indication for T_s. The Raman data of the used BFA (G23) sample (tin flux grown) suggest a local $T_s \sim 100$ K at the measuring position of the Raman experiment (see chapter 5.2).

The superconducting transitions in the ternary iron arsenide samples appeared sharp. The diamagnetic signal of SKFA (G15) at T_c, for instance, is characterized by an onset of 32 K, a midpoint of 29 K, and a $10-90$ % width of 4 K. Similar data were previously reported for BKFA (G07) [Par09].

4.3 $Fe_{1+y}Se_xTe_{1-x}$

4.3.1 General aspects about $Fe_{1+y}Se_xTe_{1-x}$

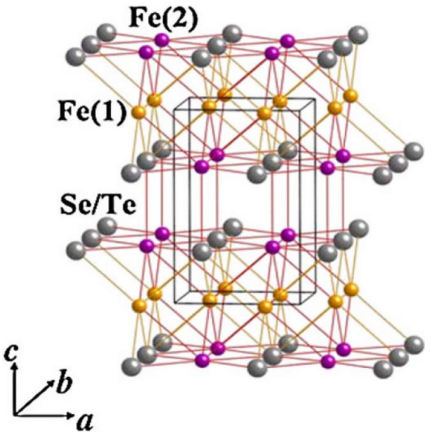

Figure 4.13: Crystal structure of FST at room-temperature [Bao09]. The Fe(1) and Se/Te sites are fully occupied according to stoichiometry. The interstitial Fe(2) sites are partially occupied by iron excess (y > 1).

The iron chalcogenide system $Fe_{1+y}Se_xTe_{1-x}$ (FST) constitutes a small group out of the large family of iron-based superconductors. As an experimental advantage, FST contains no arsenic and is therefore less toxic. FST is particularly interesting for a comparison to the ternary iron arsenides, because of a simpler crystal structure. Figure 4.13 shows the crystal structure of FST at room-temperature, which is tetragonal with space group $P4/nmm$ (PbO-type) [Li09]. In the FST system the stoichiometric iron atoms fully occupy the Fe(1) sites, while excess iron (y > 0) can be located at the interstitial sites between the Se/Te atoms denoted by Fe(2) [Bao09]. The quasi-two-dimensional sheets build by the Fe(1)-Se/Te atoms are isostructural to the $FeAs^-$ sheets in the iron pnictides [Bao09], but stacked along the c-axis without any spacing layers. Therefore, the FST system can be regarded as the prototype of the different iron-based superconductors. In particular, due to the similar crystal structures of FST and the iron pnictides, both material systems are expected to show similar Fermi surfaces with correspondingly similar physical properties [Sub08].

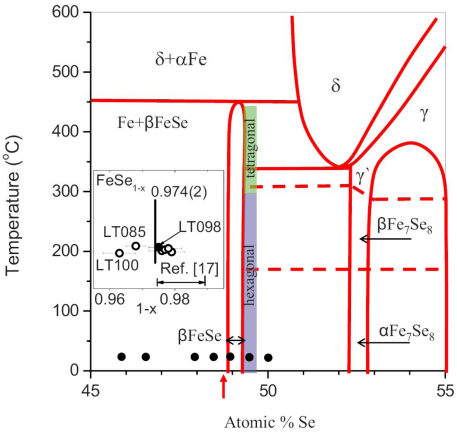

Figure 4.14: Phase diagram of the Fe-Se system [Pom09]. The red arrow indicates the center of a small superconducting composition window.

The FST system shows a complex material physics. Among the iron chalcogenides, superconductivity was firstly found in non-stoichiometric tetragonal $FeSe_{1-x}$ with $T_c \sim 8$ K, where Se deficiency seems to be essential for the formation of superconductivity [Hsu08]. Note that the tetragonal form of FeSe is called β-phase and only the β-form becomes superconducting [McQ09][2]. By applying high pressure, T_c can be enhanced up to ~ 27 K [Miz08]. The superconducting regime was determined to be located in a very small composition window centered at Se ~ 0.974 [Pom09]. Figure 4.14 shows a composite phase diagram of the Fe-Se system. The center of the small superconducting window (Se ~ 0.974) is denoted by the red arrow inside the region for a stable β-phase. Slightly different starting compositions of Fe and Se away from the superconducting composition ratio (filled black points) were found to lead to superconducting β-$FeSe_{1-x}$ with a Se content close to ~ 0.974 (open black points) plus additional phases like pure Fe, α-FeSe, or Fe_7Se_8 [Pom09]. In the absence of Te, the Fe(1) atomic site seems not to be occupied by excess iron [Pom09]. β-FeSe shows a structural phase transition from the high-temperature tetragonal to a low-temperature orthorhombic phase at $\sim 70-100$ K [Mar08, Pom09].

By substituting Te for Se, T_c can be increased up to $\sim 14-15$ K at room pressure [Sal09, Yeh08], while FeTe without Se does not become su-

[2] The β-phase of FeSe was sometimes incorrectly called α-phase [McQ09]. α-FeSe is a hexagonal stoichiometric modification (NiAs-type) that is not superconducting.

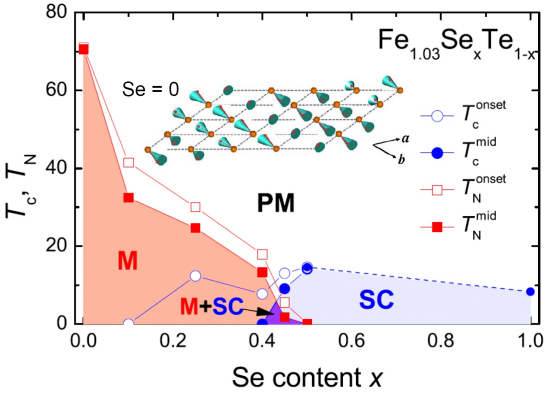

Figure 4.15: Phase diagram of $Fe_{1.03}Se_xTe_{1-x}$ (M = magnetic, PM = paramagnetic) [Kha09]. The inset shows the AFM order in β-FeTe [Bao09].

perconducting [Kha09]. Since Se^{2-} and Te^{2-} have the same valence, the Te substitution does not directly change the charge carrier density, but modifies the band structure [Fan08]. For the compounds including Te, excess iron occupies the Fe(2) sites of the crystal lattice without indication for non-stoichiometric (Se,Te)-deficiency as determined from neutron and X-ray powder diffraction [Bao09, Li09]. The exact amount of excess iron y seems to play an important role in the physical details. Undoped $Fe_{1.03}Te$ exhibits a combined structural-SDW phase transition [Li09] of first order at $T_N \sim 70$ K to a commensurate (incommensurate) AFM order with a tetragonal-to-monoclinic (tetragonal-to-orthorhombic) transition for $y \lesssim 0.1$ ($y \gtrsim 0.1$), respectively [Li09]. In the inset of figure 4.15 the AFM order of $Fe_{1+y}Te$ is shown. Despite similar Fermi surfaces, the AFM order in $Fe_{1+y}Te$ is completely different from the SDW state in the iron pnictides [Li09], showing a sinusoidal SDW order with an in-plane propagation vector that is rotated by 45° going along the diagonal direction of the Fe squares. A SDW gap is not observed [Xia09, Che09b].

Figure 4.15 shows the phase diagram of $Fe_{1.03}Se_xTe_{1-x}$. For increasing Se concentrations the structural transition is rapidly suppressed and not observed for Se > 0.1 [Sal09], while the SDW order turns into quasi-static short-range incommensurate spin fluctuations (transition temperature T_{IC}) [Wen09] that are suppressed more slowly with doping. On the other hand, superconductivity can emerge at low temperatures. For

Se $\sim 0.4 - 0.5$ there seems to be a small area of coexistence of the magnetic short-range fluctuations with superconductivity [Kha09, Bao09]. The iron excess in the Fe(2) sites is expected to be strongly magnetic [Zha09]. As a consequence, the coupling between the local Fe(2) moments with the Fe(1) squares might be able to mediate the short-range magnetic fluctuations, possibly accounting for the differences in the magnetic order compared to the iron pnictides [Liu09, Zha09]. For higher amounts of iron excess, T_c is reduced in favor of the short-range magnetic fluctuations [Liu09]. While $FeSe_{0.974}$ is metallic, for increasing amounts of Te doping [Yeh08] or iron excess in FST [Fan08] a more semiconducting behavior is observed.

4.3.2 Sample characterization

Batch	Sample	Group	Growth	T_c	$T_{N,\mathrm{IC}}$
21	$Fe_{1.08}Te$	Lin	Bridgman	-	~ 66 K
30	$Fe_{1.08}Se_{0.28}Te_{0.72}$	Lin	Bridgman	~ 9 K	~ 40 K
42	$Fe_{1.05}Se_{0.42}Te_{0.58}$	Ganin	Flux	~ 10 K	~ 40 K

Table 4.3: Studied iron chalcogenide samples.

Table 4.3 lists the three iron chalcogenide samples that have been used for the Raman experiments together with their internal batch numbers. The samples were grown in different crystal growth groups by Bridgman and flux techniques as indicated in column 3 and 4. The Bridgman technique is described in [Liu10] and the flux technique in [Tam10, Gre09]. The three samples were platelet-like single crystals with the crystallographic c-axis perpendicular to the plane surfaces. Sample 21 was Se-free and non-superconducting, while sample 30 (from same batch as used in [Tam10]) and sample 42 were superconducting with different Se concentrations and slightly different amounts of iron excess. The average chemical compositions were determined by EDX and, additionally, in sample 30 by refinement of X-ray powder diffraction data obtained from samples of the same batch [Liu]. The superconducting transition temperatures T_c were determined by magnetization measurements. Figure 4.16b shows corresponding magnetization data of sample 42, showing an onset of the diamagnetic signal of ~ 10 K, a midpoint of ~ 7.5 K, and a 10 - 90 % width of ~ 5 K.

The determination of the magnetic transitions in the different iron chalcogenide samples was difficult. While the phase transition to long-

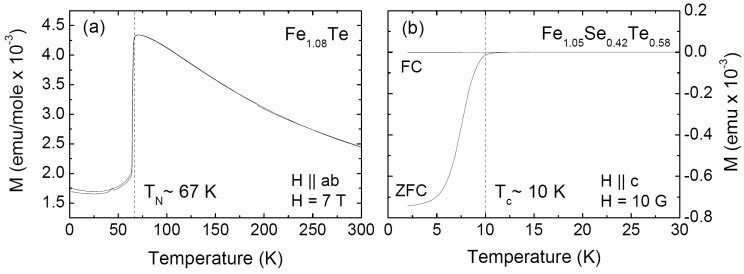

Figure 4.16: (a) Cooling and heating curves of the magnetization (M) of $Fe_{1.08}Te$ in a magnetic field of 7 T applied along the crystallographic a-axis. The dashed line indicates the AFM transition at $T_N \sim 67$ K. (b) Field-cooled (FC) and zero-field cooled (ZFC) magnetization (M) of $Fe_{1.05}Se_{0.42}Te_{0.58}$ in a magnetic field of 10 Oe applied along the crystallographic c-axis. The dashed line indicates the superconducting $T_c \sim 10$ K.

range AFM order in the Se-free $Fe_{1.08}Te$ sample is clearly observed in the magnetization by a sharp decrease at $T_N \sim 67$ K (see figure 4.16a) in agreement with previous data on Se-free samples with comparable amounts of iron excess [Li09], no corresponding anomaly could be resolved in the magnetization of the two superconducting samples 30 and 42 in magnetic fields up to 1.5 T[3]. The absence of magnetic anomalies can be attributed to very small magnetization changes at the transitions to short-range magnetic fluctuations. For future characterization studies on FST Mößbauer spectroscopy might be a better technique. In order to give an estimate for the onset temperatures of the magnetic short-range fluctuations in the superconducting FST samples one can refer to literature. In $Fe_{1.07}Se_{0.25}Te_{0.75}$, which is close to the chemical composition of sample 30, the magnetic transition was found at $T_{IC} \sim 40$ K by neutron diffraction [Wen09]. On the other hand, measurements of the Hall coefficient on samples with Se concentration of $x \sim 0.4$, which is close to the Se content of sample 42, indicate an onset temperature of the magnetic short-range fluctuations of $T_{IC} \sim 75$ K with an enhanced correlation increase at $T \sim 40$ K [Fan08].

In order to use fresh surfaces for the Raman experiments all samples were cleaved by removing the first top layers with a simple scotch tape. The effects of cleaving and aging will be discussed in chapter 5.3. Straight edges along the in-plane crystal axes provided ideal lines for sample orientation.

[3]The magnetization was measured by a QuantumDesign S-VSM SQUID.

Chapter 5

Results and discussion

5.1 $La_{2-x}Ce_xCuO_4$

5.1.1 Microstructural analysis

5.1.1.1 Raman spectra + mode assignment

For the different Raman experiments on the LCCO films both Raman setups were used. Figure 5.1 shows the Raman spectrum of the slightly underdoped LCCO film at temperature $T = 30$ K in the z(xx)z polarization configuration for $\lambda = 514.5$ nm laser excitation, while figure 5.2 shows the corresponding Raman spectra of the slightly overdoped LCCO film at the same temperature $T = 30$ K in the z(xx)z polarization configuration for $\lambda = 514.5$ nm and $\lambda = 488.0$ nm laser excitations. Due to a much weaker Raman signal obtained from the slightly overdoped LCCO film for $\lambda = 514.5$ nm, for this sample the $\lambda = 488.0$ nm line was used in addition for laser excitation in order to gain more Raman intensity. Both the slightly underdoped and the slightly overdoped LCCO films show comparable Raman spectra with four main modes (A,B,C,D) and a strong tail towards zero energy, i.e. the energy of the exciting laser line. In the slightly underdoped LCCO film, the four main modes appear at 153.5 cm^{-1} (mode A), 213.5 cm^{-1} (mode B), 308.5 cm^{-1} (mode C), and $\sim$ 640–670 cm^{-1} as a double mode (mode D). In the slightly overdoped LCCO film, the four main modes appear at 152.0 cm^{-1} (mode A), 213.5 cm^{-1} (mode B), 305.5 cm^{-1} (mode C), and $\sim$ 640–670 cm^{-1} (mode D). Modes at $\sim$ 429 cm^{-1}

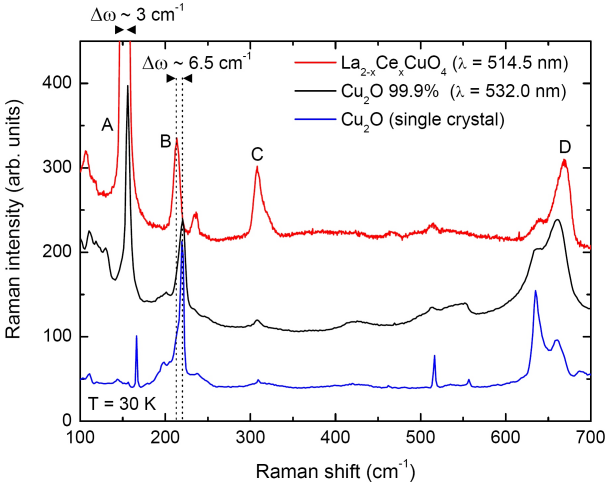

Figure 5.1: Raman spectra at 30 K of (top) the slightly underdoped LCCO film ($T_c \sim 29$ K, $x \sim 0.08$) in z(xx)z polarization configuration for 514.5 nm laser excitation, (middle) the Cu_2O powder sample (99.9 % purity), and (bottom) the Cu_2O single crystal each for 532.0 nm laser excitation. (Cu_2O spectra scaled and shifted vertically for clarity.)

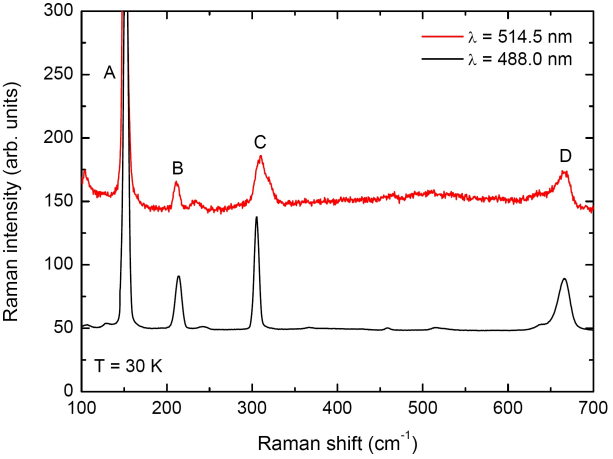

Figure 5.2: Raman spectra at 30 K of the slightly overdoped LCCO film ($T_c \sim 27$ K, $x \sim 0.1$) in z(xx)z polarization configuration for 514.5 nm and 488.0 nm laser excitation.(Spectra scaled and shifted vertically for clarity.)

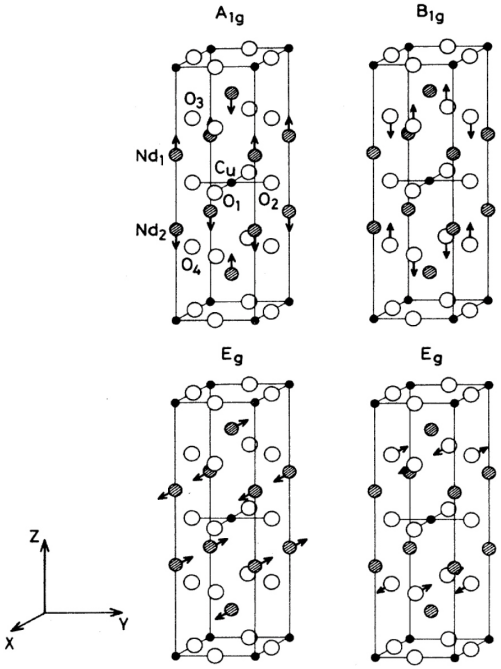

Figure 5.3: Displacement patterns of the Raman-active optical modes in T'-Nd_2CuO_4, as obtained from shell model calculations [Sug89].

and ~ 580 cm^{-1}, which would correspond to or were associated to apical oxygen vibrations in the T-structure of La_2CuO_4 [Tho91, Hey91], respectively, are not observed, indicating the absence of apical oxygen residuals.

A group theoretical analysis of the phonon modes of the T'-structure (tetragonal space group $I4/mmm$ (D_{4h}^{17})) [Had89] yields A_{1g}+B_{1g}+2E_g Raman-active modes. Due to a lack of Raman data on T'-LCCO, data on related T'-lanthanide cuprates such as NCCO have to be used for comparison [Tho91, Sug89, Hey91]. Figure 5.3 shows the displacement patterns of the four Raman-active optical modes in T'-Nd_2CuO_4, as obtained from shell model calculations [Sug89]. The energies of modes B and C are close to, but somewhat lower than those of the A_{1g} (~ 223 cm^{-1}) and B_{1g} (~ 327 cm^{-1}) vibrations of the Nd and out-of-plane oxygen atoms in T'-NCCO, respectively [Hey91]. Due to the higher mass of Nd compared to La, this downward shift goes against the intuition with respect to the mass

dependence of phonons. However, a downward shift of this size would be in line with a continuous frequency evolution previously observed in the series of T'-lanthanide cuprates [Hey91], probably induced by the increasing lanthanide radii due to the inverse lanthanide contraction [Hey91], e.g. the B_{1g} mode in PCCO is shifted compared to the B_{1g} mode in NCCO to lower energies by ~ 29 cm^{-1} [Hey91]. Furthermore, a checking of the Raman selection rules in the LCCO films has been tried (not shown). Modes B and C follow approximately the selection rules of the A_{1g} and B_{1g} modes in T'-LCCO [Tho91]. A total distinction of the different modes by this technique was not possible due to an experimental polarization leakage.

The assignment of modes A and D is more difficult, because Raman spectra of other cuprates with the T'-structure do not exhibit modes with similar energies. Therefore, possible contamination by impurity phases has been investigated, including Cu_2O which has been previously observed as a contaminant in NCCO [Had89]. For comparison, one platelet-like Cu_2O single crystal with the *c*-axis perpendicular to the plane surface and two commercial Cu_2O powder samples were used[1]. Figure 5.1 shows a comparison to reference spectra of compressed Cu_2O powder sample I (99.9 % purity) and the Cu_2O single crystal for 532.0 nm laser excitation. Based on this comparison and on earlier data on Cu_2O [Pet75, Pet72], modes A and D can be identified with the infrared-allowed $\Gamma_{15}^{(1)}$ and $\Gamma_{15}^{(2)}$ modes of Cu_2O [Hua63]. Due to resonant Raman light scattering in the vicinity of excitonic bands ("blue exciton"), these modes can become Raman-active with high intensity [Pet74, Yu73]. The much stronger intensity of the $\Gamma_{15}^{(1)}$ mode in the Cu_2O powder compared to the Cu_2O single crystal can be attributed to powder averaging over all possible polarization geometries. Mode A in the LCCO films also shows high intensity, suggesting an isotropic orientation of the Cu_2O impurity phase. The shift of ~ 3 cm^{-1} of mode A with respect to the $\Gamma_{15}^{(1)}$ mode of Cu_2O may be a consequence of stress imposed by the LCCO matrix. Note that modes with energies roughly comparable to those of modes B and C are also present in the Cu_2O reference spectra, but the former mode is shifted by ~ 6.5 cm^{-1} with respect to mode B, and the latter mode is extremely weak. It will be shown below that the modes B and C likely originate from LCCO.

[1] Cu_2O powder (I) had a purity of 99.9% with maximal impurity content of 0.006% Fe, 0.004% Si, 0.003% Pb, 0.002% Mn, and 3 ppm Sb (as indicated by the supplier). Cu_2O powder (II) had a purity of 99.5%, and the supplier did not provide information about the nature of the impurities.

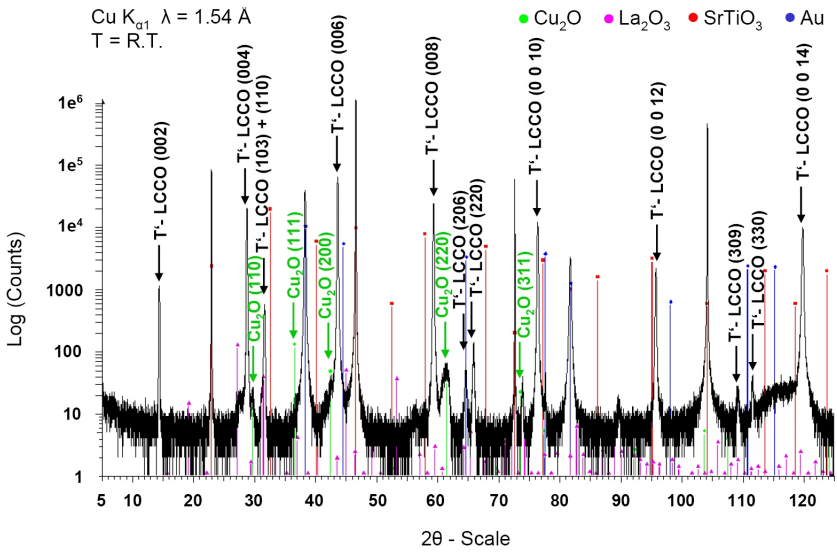

Figure 5.4: XRD Θ-2Θ-scan of the slightly underdoped LCCO film at room temperature (Cu $K_{\alpha1}$, $\lambda = 1.54$ Å). The Bragg reflections of $SrTiO_3$ and gold are due to the substrate and gold contacts on top of the film.

5.1.1.2 XRD

In order to directly characterize the chemical composition of the LCCO films, high-intensity X-ray diffraction (XRD) was used. Figure 5.4 shows a Θ-2Θ scan of the slightly underdoped LCCO film at room temperature, plotted on a logarithmic intensity scale. Based on a comparison with the calculated Bragg angles for the T'-structure [Nai00], the expected [001]-oriented T'-structure can be clearly identified as the main phase. Figure 5.5 shows additional XRD pole figure measurements of the same sample at room temperature along the (103) and (114) directions. Both measurement techniques reveal peaks that can be attributed to the Bragg peaks (103) and (110) of the T'-structure, indicating two T'-LCCO minority phases with different growth directions, which are probably stabilized by a well-known, accidental match between the in-plane and out-of-plane lattice parameters ($c/a \approx 3$). No indication for the presence of any T-structure inclusions was found. The XRD measurements also confirm the presence of a Cu_2O impurity phase, as well as a trace amount of La_2O_3 (Fig. 5.4).

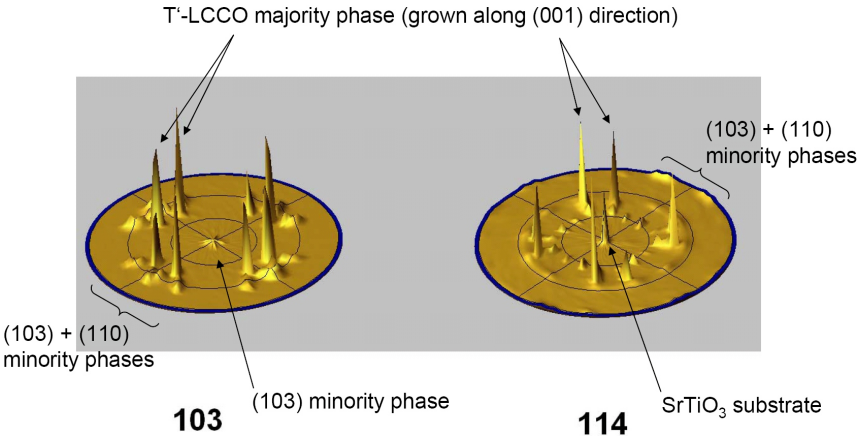

Figure 5.5: XRD pole figures of the slightly underdoped LCCO film along the (103) and (114) directions at room temperature (Cu $K_{\alpha 1}$, $\lambda = 1.54$ Å). The Bragg reflections from the T'-LCCO majority phase (grown along the (001) direction) are doubled because of the bicrystal film geometry.

The intensities of the main Cu_2O Bragg reflections are about four orders of magnitude below those of LCCO, but their ratios indicate random orientation of the Cu_2O crystallites, in contrast to the epitaxially oriented LCCO matrix. Taking powder averaging of the Cu_2O Bragg reflections into account, the XRD data imply that the volume fraction of Cu_2O is only about an order of magnitude below the one of LCCO. Note that the determination of the Cu_2O inclusions in the LCCO film required an experimental setup with a ratio of LCCO Bragg intensities to the noise floor of $\sim 10^4$ (Fig. 5.4), which goes beyond the typical diagnostics run on thin films, together with a logarithmic plotting of the experimental data.

In order to provide information about possible structural distortions in the LCCO films, which could be intrinsic or induced by a structural phase transition in the $SrTiO_3$ substrate, temperature-dependent XRD measurements were performed. Figure 5.6 shows the lattice parameters of the crystallographic a, b- and c-axes of the slightly underdoped LCCO film as a function of temperature. The lattice parameters were calculated using the Bragg angles of the (0 0 14) and (1 0 11) Bragg peaks at these temper-

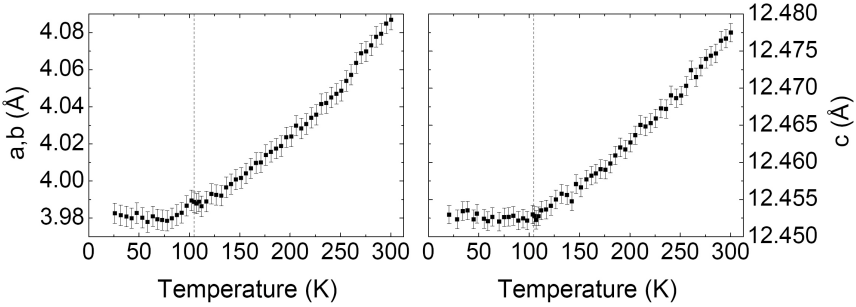

Figure 5.6: Lattice parameters of the crystallographic a, b- and c-axes of the slightly underdoped LCCO film as a function of temperature, calculated using the Bragg angles of the (0 0 14) and (1 0 11) Bragg peaks at these temperatures (see text for details) (Mo $K_{\alpha 1}$, $\lambda = 0.7093$ Å). The vertical lines indicate the transition temperature of a weak structural phase transition from cubic to tetragonal at ~ 105 K in the $SrTiO_3$ substrate.

atures[2]. The room-temperature values of the experimentally determined lattice parameters of the LCCO film are close to the reported parameters for the T'-structure of LCCO ($a = 4.015$ Å, $c = 12.46$Å [Nai00]). The lattice parameters follow nearly perfectly the typical temperature dependence as expected from elastic stiffness [Hel84]. Both the a, b- and c-axis lattice parameters show no indication for anomalous behavior outside the error bars in the examined temperature range. Furthermore, no additional Bragg peaks between high and low temperatures were found. These observations suggest that T'-LCCO exhibits no structural transition between 300 K and the lowest temperature accessible in the XRD experiment ($T \approx 20$ K). The vertical lines in figure 5.6 indicate the transition temperature of a weak structural phase transition from cubic to tetragonal at ~ 105 K in the $SrTiO_3$ substrate [Hei73]. Due to the non-anomalous behavior of the LCCO film at this temperature, the structural transition in the substrate seems not to affect the epitaxially grown LCCO film.

[2]The lattice parameters of the a, b- and c-axes were calculated via Bragg's law $n\lambda = 2d\sin\theta$ and the relation $d = 1/\sqrt{\frac{h^2}{a^2} + \frac{k^2}{b^2} + \frac{l^2}{c^2}}$, where n is the order of diffraction, d is the interplanar spacing, θ is the Bragg angle, and $h\ k\ l$ are the Miller indices.

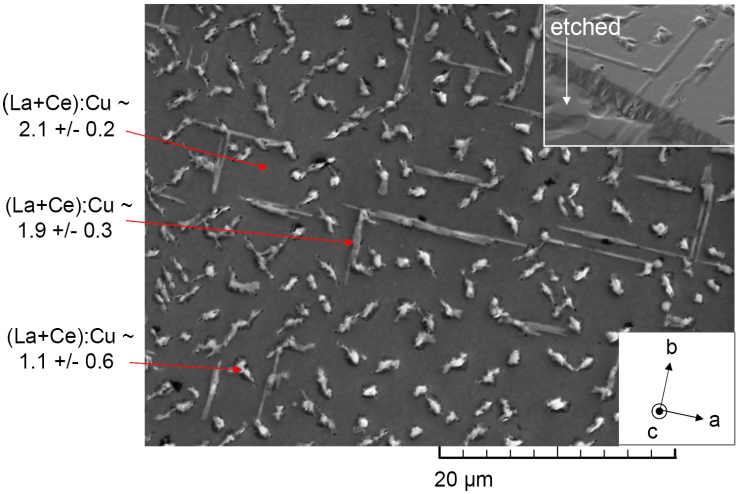

Figure 5.7: SEM image of the slightly underdoped LCCO film. The upper inset shows a partly etched surface area (see chapter 4.1.2 for details).

5.1.1.3 SEM + EDX

The microstructure and the local variation of the chemical composition of the LCCO films were further analyzed by scanning electron microscopy (SEM) and energy dispersive X-ray (EDX) analysis. The microstructure of both films appeared comparable. Figure 5.7 and 5.8 show SEM images of the slightly underdoped ($x \sim 0.08$) and the slightly overdoped ($x \sim 0.1$) LCCO films, respectively. More SEM images of the slightly underdoped LCCO film with focus on the grain boundary are shown in appendix B. In both films the surface area is uniformly flecked with particles of ~ 3 μm diameter. In particular, in the slightly overdoped LCCO film the particles have a preferred orientation along the diagonal of the *ab* crystal axes. In the LCCO ($x \sim 0.08$) film the surface coverage is about 18%, while in the LCCO ($x \sim 0.1$) film it is slightly smaller. While in the slightly underdoped LCCO film the surface background exhibits the composition ratio (La+Ce):Cu $\sim 2.1 \pm 0.2$ characteristic of T'-LCCO, the particles are centers of strongly enhanced Cu content, with the statistically averaged ratio (La+Ce):Cu $\sim 1.1 \pm 0.6$. They are thus good candidates for the Cu_2O impurity phase. The high and uniform surface coverage with particles supports the picture of an isotropically oriented Cu_2O impurity phase of

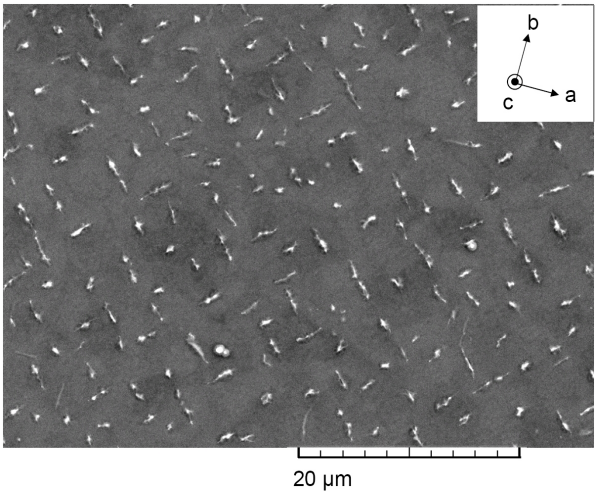

Figure 5.8: SEM image of the slightly overdoped LCCO film.

$\sim 10\%$ in the LCCO films consistent with powder averaging in XRD.

In addition, line structures oriented along the *ab* crystal axes were observed. As determined from the slightly underdoped LCCO film, they exhibit only a slightly enhanced Cu content. Like the Cu_2O particles, the line structures appear stronger in the LCCO ($x \sim 0.08$) film compared to the LCCO ($x \sim 0.1$) film. These structures may originate from structural defects or from the T'-LCCO minority phases. Both the particles and the line structures lead to inhomogeneous film surfaces, probably accounting for the strong tail in the Raman spectra at zero energy via stray light production. In the inset of figure 5.7 a surface area of the slightly underdoped LCCO film is shown, which was partly etched by Ar ion bombardment during the optical lithography procedure. Both the particles and the line structures reach deeply into the film, suggesting their formation during the crystal growth. A possible reason for the formation of the Cu_2O impurities in the LCCO films is the copper excess used during film growth (see chapter 4.1.2). The higher surface coverage in the LCCO ($x \sim 0.08$) film, which was grown with higher copper excess, compared to the LCCO ($x \sim 0.1$) film would be in agreement with this scenario. The different inclusions, i.e. the particles and line structures, seem to be not spatially connected with each other. Therefore, it can be assumed that possible

supercurrents trough the LCCO films can flow around the inclusions without influence on the transport properties. A precise examination of the Ce concentrations in the LCCO films by EDX was not possible due to experimental error bars $> 50\%$. The concentrations of impurity atoms beyond the constituent elements of LCCO were below the EDX detection limit.

5.1.1.4 Raman linescan

In order to relate the Raman spectra of figure 5.1 to the microscopic observations of figure 5.7, the "micro"-Raman setup was employed. Figure 5.9a shows a line scan of the intensity of mode A in the slightly underdoped LCCO film. The intensity varies strongly on a length scale of ~ 3 μm, which is comparable to the size of the particles in figure 5.7. This underscores the assignment of this mode to the Cu_2O impurity phase. The intensities of modes B and C, on the other hand, depend only weakly on the measuring position (Fig. 5.9a), supporting the conclusion that they do not originate from Cu_2O, but from the T'-LCCO host material. In order to attempt a removal of the Cu_2O particles from the LCCO film surface, argon ion sputtering under vacuum was applied. Table 5.1 lists the used parameters for sputtering. A comparison of SEM images of the surface before and after removal of ~ 250 nm (Fig. 5.9c) confirms that the particles are stuck deeply inside the LCCO matrix. While it is thus not possible to remove the particles, sputtering still reduces both the volume fraction of Cu_2O and the intensity of mode A (Fig. 5.9b). Modes B and C, on the other hand, are nearly unaffected by sputtering. The broad feature at ~ 550 cm^{-1} in the Raman spectrum of the underdoped LCCO film after sputtering is due to an activation of second order Raman processes, because of broken translation symmetry induced by the sputtering process.

Beam energy	1 kV
Ion current	1 μA
Beam size	~ 2 μm
Scaning rate	~ 100 Hz
Tilt angle	30°
Sputtering time	150 min

Table 5.1: Sputtering parameters.

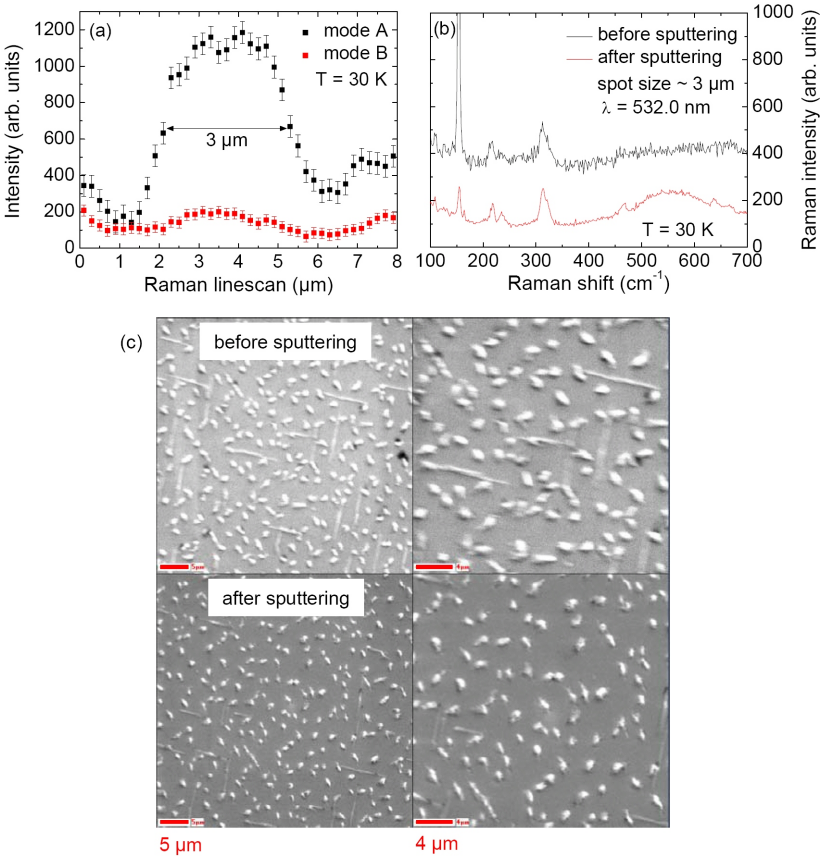

Figure 5.9: (a) Line scan of the intensities of modes A and B in the underdoped LCCO film taken with the "micro"-Raman setup (50× microscope objective, $\lambda = 532.0$ nm); (b) Raman spectra at $T = 30$ K before and after sputtering of ~ 250 nm; (c) SEM images before and after sputtering.

5.1.2 Phonon anomalies at T_c

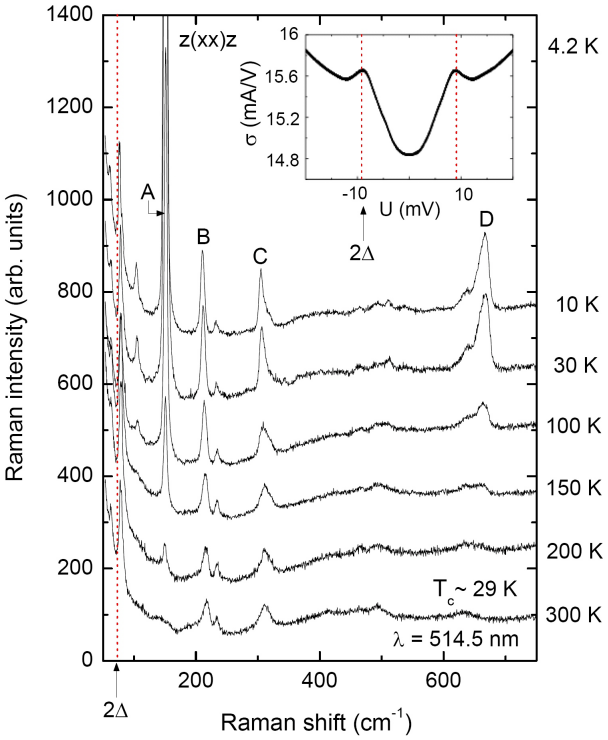

Figure 5.10: Raman spectra of the slightly underdoped LCCO film at temperatures 10 K $\leq T \leq$ 300 K in z(xx)z polarization configuration for 514.5 nm laser excitation (spectra shifted vertically for clarity). $2\Delta \sim 9$ meV denotes the energy of the superconducting gap. The inset shows the corresponding quasiparticle conductance at 4.2 K measured over the grain boundary (for experimental details see [Mül06, Wag08a]).

Having obtained a thorough understanding of the microstructure and phase composition of the LCCO films, the focus is now put on anomalies in the temperature dependence of the Raman spectra and the different optical modes at the superconducting transition temperature T_c. Figure 5.10 shows the Raman spectra of the slightly underdoped LCCO film from 10 K to 300 K in z(xx)z polarization configuration for 514.5 nm laser excitation.

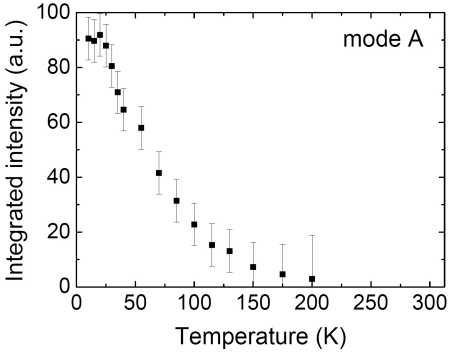

Figure 5.11: Temperature dependence of the integrated intensity (a.u. = arbitrary units) of mode A in the slightly underdoped LCCO film. (The integrated intensity above 200 K was too small for a reliable analysis.)

Due to the large tail induced by stray light in the Raman spectra towards zero energy, overshadowing the low energy part $E < 150$ cm^{-1}, the study of electronic Raman scattering in this energy region was difficult. Between the Raman spectra at temperatures above and below T_c no anomalous redistribution of the electronic background due to the opening of the superconducting gap was observed. On the other hand, the single phonons A, B, and C show very symmetric phonon lineshapes without indications of Fano-like asymmetry, indicating a weak product of the electron-phonon coupling with the number of electronic decay channels at the energies monitored by the phonons. The integrated intensities of modes A and D show a strong temperature dependence with a significant increase below $T \sim 150$ K (Fig. 5.11a). A similar activation was also observed in the corresponding $\Gamma_{15}^{(1)}$ mode in the Cu_2O powder reference samples, as shown in figures 5.14a and b, confirming their common origin from Cu_2O. In contrast, the intensities of modes B and C exhibit a much weaker temperature dependence.

Figure 5.12a shows the temperature dependence of the frequency and FWHM of mode A. The solid lines are the result of fits to the data above T_c, using an expression based on phonon-phonon interactions, i.e., the anharmonic decay of phonons [Kle66, Men84, Had98]. For simplicity a symmetric decay into two product modes was assumed (see chapter 2.2.2). While mode A follows nearly perfectly the expression for anharmonic decay in the normal state, significant deviations from this behavior are observed

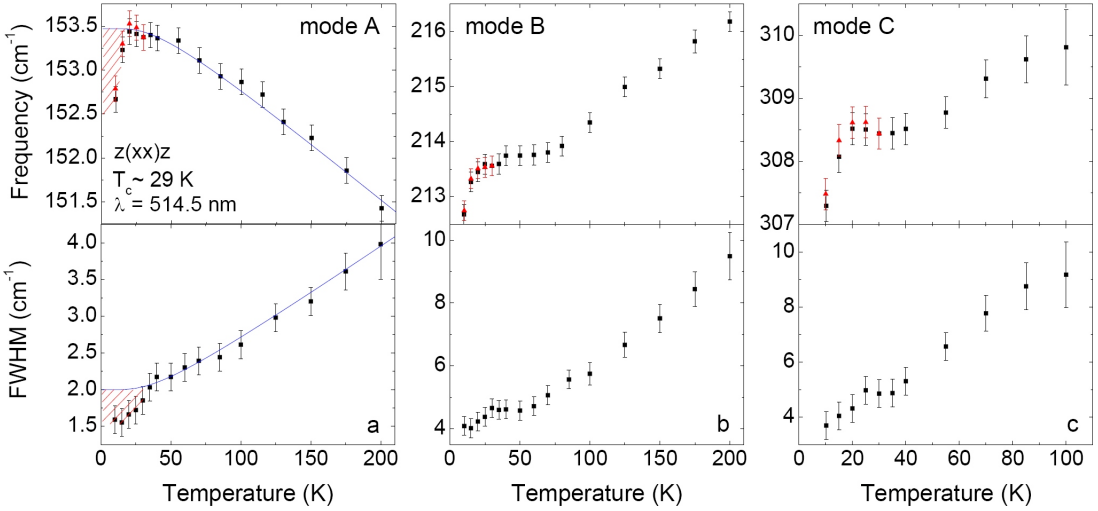

Figure 5.12: Temperature dependence of the frequency and FWHM of modes A, B, and C in the slightly underdoped LCCO film (see Fig. 5.1). The triangular points represent a second independent data set at low temperatures. The solid lines are the result of fits to the data points above T_c according to the theory of anharmonic phonon decay [Kle66, Men84, Had98] (see text for details). The shaded areas indicate deviations from the anharmonic temperature dependence below $\sim T_c$.

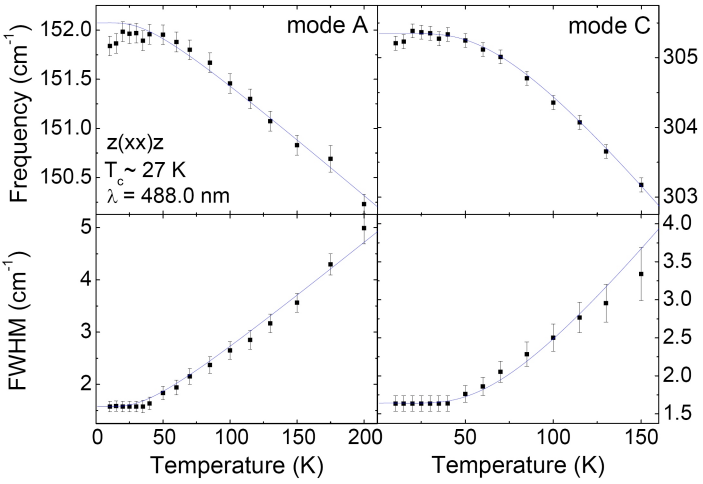

Figure 5.13: Temperature dependence of the frequency and FWHM of modes A and C in the slightly overdoped LCCO film. The 487.986 nm laser line was used for excitation. (For solid lines see caption of figure 5.12.)

below $T \sim T_c$. The frequency softens by ~ 0.7 cm^{-1} upon cooling below T_c, and the temperature dependence of the linewidth exhibits a change in slope in the same temperature range, which corresponds to a narrowing of ~ 0.5 cm^{-1}. The deviations from the anharmonic behavior are illustrated by the shaded areas in figure 5.12a. In addition, the integrated intensity of mode A also shows an anomalous change in slope in its temperature dependence at approximately the same temperature to a saturation for decreasing temperature (Fig. 5.11). In contrast to mode A, the temperature dependence of the parameters characterizing modes B and C differs substantially from the standard anharmonic behavior (Figs. 5.12b and c). In particular, their frequencies increase continuously with increasing temperature, opposite to the behavior expected from anharmonicity. Below T_c, however, they exhibit softening and narrowing of the same magnitude as the one observed for mode A. Mode D also hints at a softening of similar size at the same temperature, but its broad double-peak structure does not allow a precise analysis. Remarkably, both the anomalous normal-state behavior of mode C and the renormalization of the phonon frequencies below T_c are absent in the slightly overdoped LCCO film (Fig. 5.13), suggesting that these features are controlled by the doping level of LCCO.

5.1.3 Control measurements on Cu_2O powders

For comparison measurements of the temperature dependence of the magnetic susceptibility and the phonon frequencies, linewidths, and integrated intensities of the two commercial Cu_2O powders were performed. Although pure Cu_2O is nonmagnetic [Sch69], the susceptibilities of both powders exhibit pronounced low-temperature Curie tails due to magnetic impurities (Fig. 5.14). The susceptibility of one of the two samples even exhibits a small anomaly at low magnetic fields and $T \sim 6$ K, and some field hysteresis over a wider temperature range (Fig. 5.14b). These observations agree qualitatively with a recent report of a substantial influence of cation vacancies and small amounts of magnetic impurities on the magnetic properties of Cu_2O [Che09a]. The overall temperature dependence of the frequency of the intense $\Gamma_{15}^{(1)}$ mode shown in Fig. 5.14 is consistent with the one expected for anharmonic decay. In powder sample I, however, the mode abruptly hardens by ~ 0.5 cm^{-1} between $T \sim 15$ K and the base temperature of 5 K (Fig. 5.14a), while powder sample II shows a small hint of a softening (Fig. 5.14b). In addition, the integrated intensity of the same mode in powder sample I shows a saturation at ~ 15 K and an enhanced increase between 15 K and the base temperature (Fig. 5.14a), while powder sample II shows the opposite trend with a decrease of the integrated intensity after a saturation for further cooling to the lowest temperature (Fig. 5.14b). The corresponding linewidths do not show anomalous behavior outside the error bars in this temperature range.

All these phonon anomalies are surprising, because low-temperature structural instabilities have not been reported for Cu_2O [Wer82]. Moreover, they are apparently uncorrelated with features in the magnetic susceptibility. The phonon anomalies therefore likely arise from sample-specific defects or impurities. Note that the anomaly of the Cu_2O vibration in powder sample I with higher purity level is smaller in magnitude and of opposite sign than the one exhibited by mode A in the underdoped LCCO film (which was fabricated from ultrapure metal sources and is therefore much less affected by magnetic impurities than the commercial powders), and that it occurs at a lower temperature. Nonetheless, the Raman data on Cu_2O do indicate that the low-temperature behavior of the $\Gamma_{15}^{(1)}$ mode is quite sensitive to microstructural details. This may provide clues to the origin of the anomalous low-temperature behavior of mode A in the LCCO film, which had been identified with the $\Gamma_{15}^{(1)}$ mode of the Cu_2O inclusions.

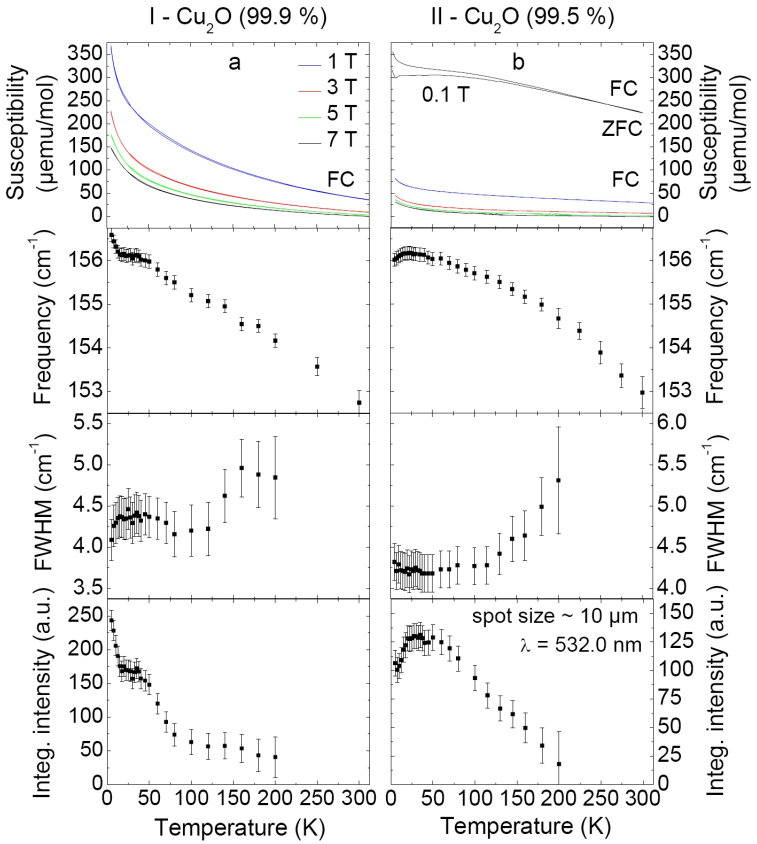

Figure 5.14: Temperature dependence of the magnetic susceptibility for different magnetic fields (FC = field cooled, ZFC = zero field cooled), and frequency, FWHM, and integrated intensity of the $\Gamma_{15}^{(1)}$ mode of the two compressed Cu_2O powder samples with different purity levels (for compositional details see footnote 2). (The phonon amplitude above 200 K was too small for a reliable analysis of the linewidth and integrated intensity.)

5.1.4 Discussion

All of the Raman-active phonons observed in the underdoped LCCO film (including modes B and C that are likely due to the LCCO host material as well as mode A, which likely arises from Cu_2O inclusions) exhibit anomalies in their temperature dependence that are reproducible and clearly outside the experimental error bars at a temperature that is consistent with T_c. In discussing these observations, the Cu_2O inclusions shall be firstly ignored.

In the standard picture of superconductivity-induced phonon self-energy anomalies [Zey90, Tho91, Dev94] (see chapter 2.2.2), optical phonons with energies higher than twice the superconducting gap, 2Δ, harden below T_c, and their linewidths increase due to an enhanced density of states above the gap. Conversely, phonons with energies below 2Δ are expected to soften. In the "clean limit" deviations from this behavior are predicted only close to 2Δ [Zey90]. Experimental observations on the hole-doped cuprate high-temperature superconductors, like e.g. on $YBa_2Cu_3O_{7-x}$, are largely consistent with this theory [Bak09]. The superconducting energy gap of LCCO is known from prior transport measurements on the same films that were investigated by Raman light scattering [Wag08b]. Tunneling characteristics (one of which is reproduced in the inset of Fig. 5.10) show coherence peaks at an energy of 9 meV, which implies $2\Delta \sim 75$ cm^{-1}. Since the energies of all of the Raman-active phonons discussed are far above 75 cm^{-1}, the standard model predicts a weak hardening and broadening below T_c, in complete contrast to the observations. A very high scattering probability in the "dirty limit" can in principle shift the real part of the phonon self-energy in the superconducting state below the corresponding energy of the normal state for energies above 2Δ (Fig. 5.15), which could provide an explanation for a phonon softening at energies above 2Δ. However, in this case the coupling via Kramers-Kronig relation would lead to a shift of the imaginary part of the phonon self-energy to lower energies, corresponding to an enhanced phonon broadening below T_c, what is not observed.

Since the standard theory of superconductivity-induced phonon renormalization fails to account for the observations displayed in figure 5.12, more unconventional scenarios have to be considered. A possible explanation of the softening and narrowing of the optical modes below T_c would be a second gap with magnitude in excess of $2\Delta^* \sim 100$ meV that opens at a temperature close to T_c or is at least affected by the superconducting phase transition. In this case, all of the Raman-active optical modes would be located below this threshold energy, and the observed softening could be ex-

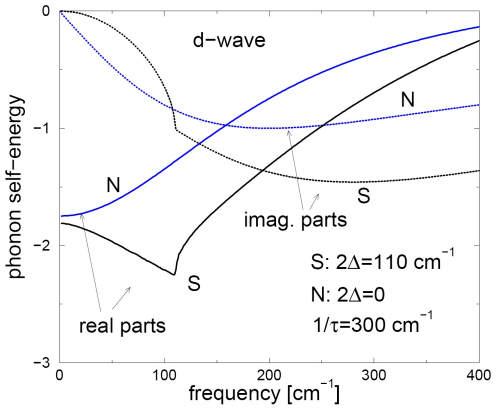

Figure 5.15: Real and imaginary part of the phonon self-energy of a d-wave superconductor in the normal (N) and superconducting (S) state calculated for superconducting gap maxima of $2\Delta = 110$ cm^{-1} in the dirty limit ($1/\tau = 300$ cm^{-1}, where τ is the scattering time) [Zey].

plained by a straightforward application of the theory of phonon self-energy to this high-energy gap. The narrowing of the phonon linewidths would then be a direct consequence of the reduced number of relaxation channels due to the loss of spectral weight below $2\Delta^*$. Angle-resolved photoemission spectroscopy [Arm01, Mat07] and optical spectroscopy [Ono01, Zim05] experiments on underdoped NCCO have indeed yielded evidence of a high-energy "pseudogap" that opens up below a temperature $T^* > T_c$. Both T^* and the magnitude of Δ^* were found to decrease with increasing doping level [Mat07, Dag05], so that T^* cuts the superconducting phase boundary at optimal doping (figure 5.16) [Zim05]. In the superconducting regime of NCCO, $\Delta^* \sim 100$ meV $\gg \Delta$ [Mat07]. However, tunneling characteristics of the slightly underdoped LCCO film up to 250 meV in the superconducting state (Fig. 5.17) show no indication for coherence peaks at high energies that could be indicative for a high energy "pseudogap" [Wag].

Although no evidence has yet been reported of a similar phenomenon in LCCO, it is thus conceivable that interplay between superconductivity and the pseudogap (which may in turn be related to the presence of antiferromagnetic order [Mat07]) could explain the observed unusual superconductivity-induced phonon self-energy anomalies. However, the nearly identical anomalies exhibited by mode A (which, as has been ar-

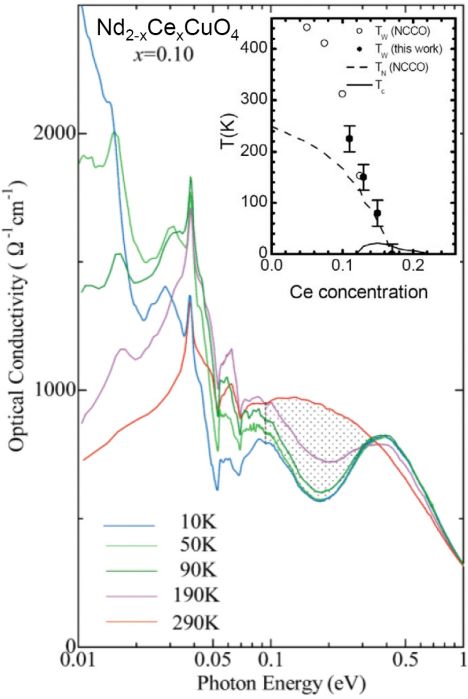

Figure 5.16: Temperature dependence of the optical conductivity in underdoped NCCO ($x = 0.1$) on a logarithmic scale of photon energy [Ono01]. The mesh region indicates the spectral-weight loss due to the formation of the high-energy "pseudogap". The inset shows the corresponding onset temperature of the "pseudogap" as a function of doping [Zim05].

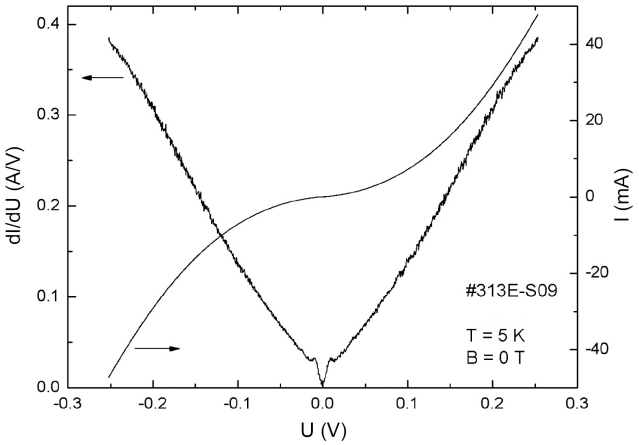

Figure 5.17: Quasiparticle conductance and transport characteristic of the slightly underdoped LCCO film up to 250 meV at 5 K measured over the grain boundary [Wag] (for experimental details see [Mül06, Wag08a]).

gued, probably originates in the Cu_2O inclusions) point to a more complex picture in which proximity and/or inverse proximity effects at the LCCO/Cu_2O interface are involved. It is possible, for instance, that charge transfer across the interface leads to the formation of magnetic Cu^{2+} ions and induces cooperative magnetism at the boundaries of the Cu_2O inclusions, which in turn enhances antiferromagnetic order and the pseudogap in LCCO. An investigation of phonon anomalies close to the interface by Raman spectroscopy with spatial resolution comparable to the superconducting coherence length is well beyond the current experimental capabilities, but may become possible in the future based on advances in near-field optics. Based on the observations in LCCO films, it appears worthwhile to study such effects systematically using other experimental methods.

In addition to its scientific interest, the technical aspects of the presented Raman study on LCCO are of general relevance for the investigation of electron-doped cuprate high-temperature superconductors. Inclusions of impurity phases such as lanthanide oxides [Man04, Rob09] and Cu_2O are hard to avoid during synthesis and continue to be present in state-of-the-art crystals and films. They are also difficult to detect based on standard X-ray diffraction, either because epitaxial intergrowth leads to Bragg peak positions that are similar to those of the host phase [Man04, Rob09] or be-

cause powder averaging greatly reduces the intensity of the impurity Bragg reflections. Note, in particular, that the Cu_2O inclusions in the studied LCCO films required an experimental setup with a ratio of LCCO Bragg intensities to the noise floor of $\sim 10^4$ (Fig. 5.4), which goes beyond the typical diagnostics run on thin films. It has been shown that both electron microscopy and micro-Raman spectroscopy are powerful, complementary diagnostic tools (Fig. 5.9). A thorough understanding of the local microstructure and impurity inclusions is important for many experimental techniques, such as optical spectroscopy and transport measurements.

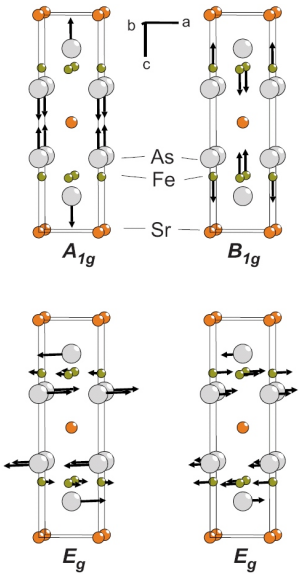

Figure 5.18: Displacement patterns of the Raman-active optical modes in the ternary iron arsenides as obtained from shell model calculations [Lit08].

5.2 $R_{1-x}K_xFe_2As_2$ (R = Ba, Sr) and $BaFe_{2-x}Co_xAs_2$

5.2.1 Mode assignment

From the tetragonal $ThCr_2Si_2$-type crystal structure of the ternary iron arsenides [space group I4/mmm (D_{4h}^{17})] (see chapter 4.2) one expects four Raman-active optical modes with symmetries A_{1g}+B_{1g}+2E_g. Figure 5.18 shows the displacement patterns of the four Raman-active optical modes, as obtained from shell model calculations [Lit08]. Table 5.2 lists the four different modes together with their corresponding selection rules.

A_{1g}	B_{1g}	E_g	E_g
(xx), (yy), (zz)	(xx), (yy), (x'y')	(xz), (yz)	(xz), (yz)

Table 5.2: (*upper line*) Raman-active optical modes in the ternary iron arsenides with (*lower line*) corresponding selection rules [Lit08].

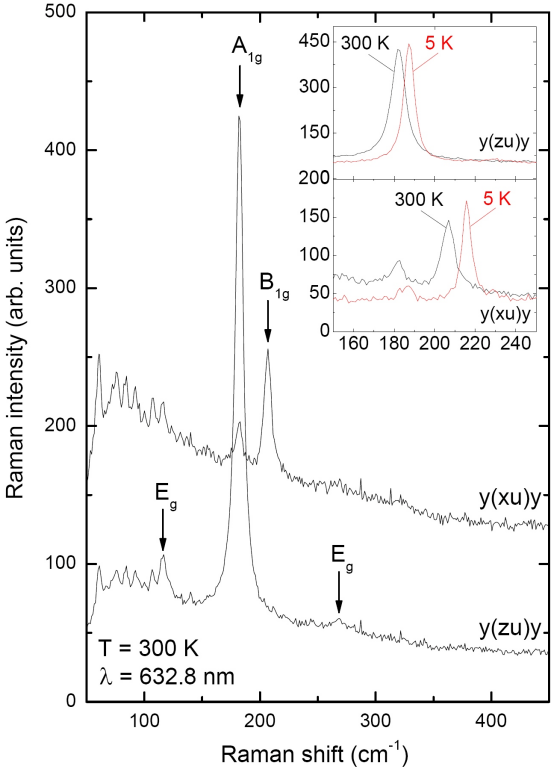

Figure 5.19: Raman spectra of underdoped BKFA (G07) at 300 K in y(xu)y and y(zu)y polarization configurations for $\lambda = 632.8$ nm laser excitation. The additional peaks below ~ 150 cm^{-1} are artifacts of the optical setup. The insets show a comparison of the Raman spectra at 5 and 300 K.

The Raman measurements on the ternary iron arsenides were exclusively performed with the "micro" setup using the 50x microscope objective. In order to maximize the Raman intensity, a polarization analyzer was not used (u = unpolarized). Figure 5.19 shows the Raman spectra of the underdoped BKFA (x $\sim$ 0.28) single crystal at 300 K for the y(xu)y and y(zu)y polarization configurations for $\lambda = 632.8$ nm laser excitation. According to the mode assignment in [Lit08] and the selection rules, the peaks at 182 and 206 cm^{-1} can be identified with the A_{1g} and B_{1g} vibrations of the As and Fe atoms, respectively. The A_{1g} mode is strong

for y(zu)y and weak for y(xu)y polarization, respectively. The B_{1g} mode cannot be observed for y(zu)y polarization in accordance with the selection rules (see table 5.2). The two in-plane E_g modes, involving Fe and As atoms, are weak and are observed at 116 and 268 cm^{-1} in the y(zu)y polarization configuration. All modes show very symmetric phonon lineshapes without Fano-like asymmetry. The insets show the corresponding Raman spectra at 5 and 300 K. All modes show a clear shift to lower energies upon heating from 5 to 300 K, as expected from phonon anharmonicity (see below). Note that the additional peaks below ~ 150 cm^{-1} are temperature independent and reference measurements on standard samples show that they are experimental artifacts (possibly due to scattering from air).

The Raman spectra of the different ternary iron arsenide samples appeared very similar. Table 5.3 lists the experimentally determined frequencies of the corresponding four Raman-active modes at room temperature. The A_{1g} mode in the samples with Sr is shifted by $\sim 1-2$ cm^{-1} to higher energies compared to the samples with Ba, while the B_{1g} mode shows a shift of similar size to lower energies. From the phonon mass dependence one expects larger hardenings ($> 20\%$). This indicates that the shifts are rather dominated by modifications of the crystal structure. For increasing doping with K or Co the A_{1g} mode shifts to higher energies, while the B_{1g} mode shows the opposite trend for underdoping with K. The low-energy E_g mode tends to shift to lower (higher) energies for K-(Co-)doping. Since the Fermi surfaces change differently for hole-/K- [Zab09] and electron-/Co-doping [Liu10], the different kinds of shifts may be induced by the electron-phonon coupling. Additional contribution comes from modifications of the crystal structure by the different-weighted doping atoms.

Batch	**Sample**	**x**	A_{1g}	B_{1g}	E_g	E_g
G12	SFA	-	182.9	206.4	119.9	268.4
G30	BFA	-	180.9	208.7	123.6	266.4
G23	BFA	-	180.2	209.0	121.9	264.4
G15	SKFA	~ 0.15	183.3	204.8	118.9	270.6
G07	BKFA	~ 0.28	182.1	206.3	116.2	268.3
G41	BKFA	~ 0.32	182.7	209.9	117.3	268.2
G64	BFCoA	~ 0.08	181.7	210.9	125.0	266.4
G33	BFCoA	~ 0.13	182.4	207.5	125.6	265.6

Table 5.3: Experimentally determined frequencies (cm^{-1}) of the Raman-active modes in the ternary iron arsenide samples at room temperature.

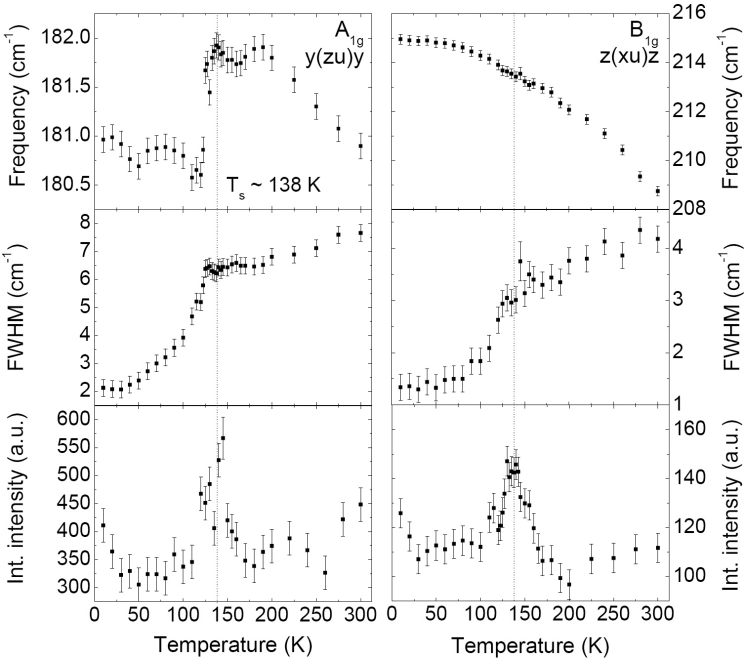

Figure 5.20: Temperature dependence of the frequency, FWHM, and integrated intensity (a.u. = arbitrary units) of the A_{1g} and B_{1g} modes in undoped BFA (G30) (grown in self-flux). The vertical lines indicate the combined structural-SDW phase transition temperature $T_s \sim 138$ K.

5.2.2 Phonon anomalies

5.2.2.1 Undoped $BaFe_2As_2$ and $SrFe_2As_2$

Figure 5.20 and 5.21 show the frequency, FWHM, and integrated intensity of the A_{1g} and B_{1g} modes of undoped BFA (self-flux grown) and undoped BFA (tin flux grown) in the y(zu)y and z(xu)z and in the y(zu)y and y(xu)y polarization configurations as a function of temperature, respectively. Figure 5.22 shows corresponding data of the frequency and FWHM of undoped SFA (tin flux grown) in the y(zu)y and y(xu)y polarization configurations. The vertical lines in figure 5.20 and 5.22 correspond to the critical temperatures T_s for the combined structural-SDW phase transitions, while the vertical lines in figure 5.21 are guides to the eye for T_s.

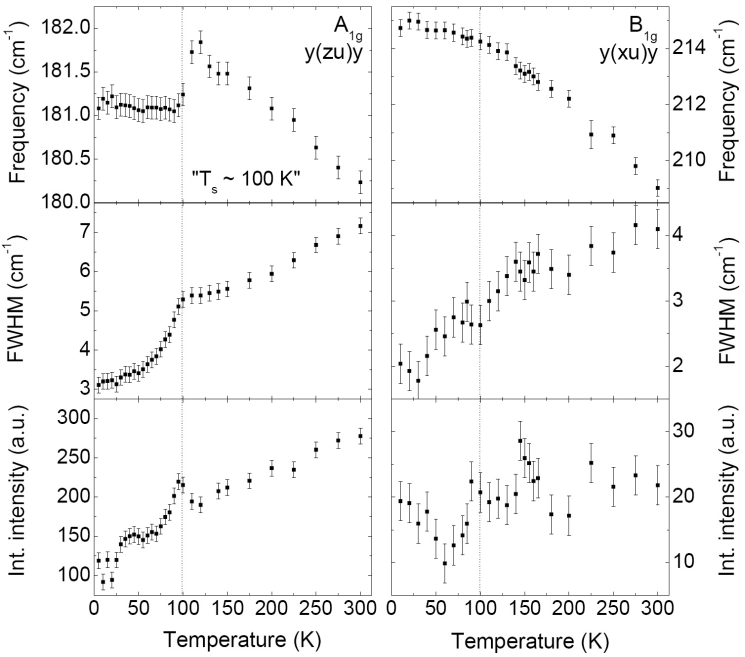

Figure 5.21: Temperature dependence of the frequency, FWHM, and integrated intensity of the A_{1g} and B_{1g} modes in undoped BFA (G23) (grown in tin flux). The vertical lines are guides to the eye, suggesting a possible structural-SDW phase transition temperature of $T_s \sim 100$ K.

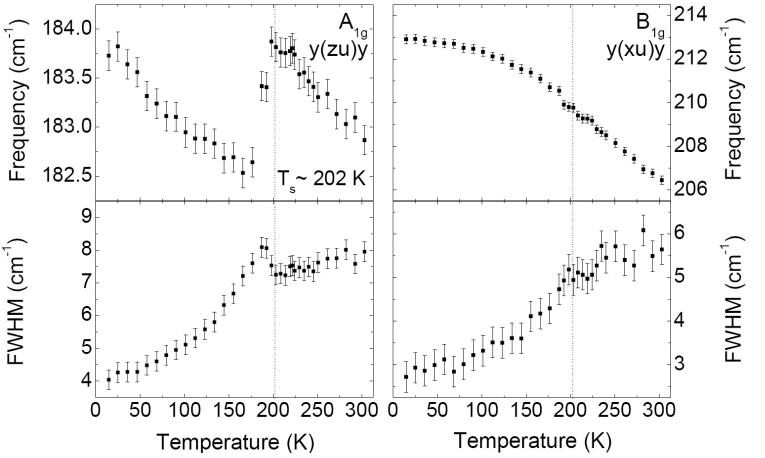

Figure 5.22: Temperature dependence of the frequency and FWHM of the A_{1g} and B_{1g} modes in undoped SFA (G12). The vertical lines indicate the combined structural-SDW phase transition temperature $T_s \sim 202$ K.

The temperature evolution of the phonon parameters of the A_{1g} and B_{1g} modes in undoped BFA (self-flux grown) and SFA (tin flux grown) are closely similar, showing pronounced singularities in the frequency and linewidth at the combined structural-SDW phase transition temperatures T_s. The A_{1g} modes show a discontinuous softening by ~ 1 cm^{-1} at T_s together with a change in slope in their corresponding linewidths, followed by a continuous narrowing upon cooling. In particular, the A_{1g} mode of undoped BFA (self-flux grown) narrows by more than ~ 4 cm^{-1} between T_s and the lowest temperature. In undoped SFA the A_{1g} mode linewidth shows a slight increase at T_s ahead of the narrowing for lower temperatures. On the other hand, the B_{1g} mode frequencies in undoped BFA and SFA show a small break in their temperature dependence to a weak hardening at T_s, as well as a continuous narrowing by ~ 2 cm^{-1} between T_s and base temperature. Similar behavior was reported before for $CaFe_2As_2$ [Cho08]. In undoped BFA (self-flux grown) the integrated intensity of the A_{1g} and B_{1g} modes is locally enhanced by $\sim 50\%$ around T_s, while in undoped SFA no intensity anomaly is observed at the corresponding T_s (not shown).

The two undoped BFA samples (self-flux and tin flux grown) show comparable phonon anomalies. However, the phonon anomalies in the BFA

(tin flux grown) sample are shifted to lower temperature with respect to BFA (self-flux grown). This observation is in agreement with previous experiments on undoped BFA, where the combined structural-SDW phase transition temperature T_s was found to shift to lower temperatures for tin contamination during crystal growth [Sun09]. The transition temperature T_s apparently depends on the local tin concentration. The phonon anomalies in the BFA (tin flux grown) sample suggest a local transition temperature of $T_s \sim 100$ K. On the other hand, the corresponding phonon anomalies in undoped SFA (tin flux grown) appear exactly at the reported temperature for T_s [Teg08] in agreement with previous results, where no shift of T_s was found in SFA between self-flux and tin flux growth [Sun09].

5.2.2.2 $Ba_{1-x}K_xFe_2As_2$ and $Sr_{1-x}K_xFe_2As_2$

Figure 5.23 shows the frequency and FWHM of the A_{1g} and B_{1g} modes of underdoped SKFA ($x \sim 0.15$) in the y(zu)y and z(xu)z polarization configurations as a function of temperature. Figure 5.24 and 5.25 show corresponding data of the frequency, FWHM, integrated intensity, and amplitude of underdoped BKFA ($x \sim 0.28$) and optimally doped BKFA ($x \sim 0.32$) in the y(zu)y and y(xu)y and in the y(zu)y and z(xu)z polarization configurations, respectively. The vertical lines indicate the critical temperatures T_c and T_s of the superconducting and the SDW phase transitions, respectively. After a discussion of the stronger phonon anomalies at T_s, the relatively subtle line-shape anomalies at T_c will be discussed.

In the underdoped SKFA sample (Fig. 5.23), which exhibits the lowest doping level among the BKFA and SKFA samples, the A_{1g} mode frequency shows a softening by ~ 0.5 cm^{-1} around T_s, which reminds strongly on the discontinuous softening at T_s in the undoped samples. However, in the underdoped case this anomaly is reduced and smeared out in temperature. In underdoped BKFA (Fig. 5.24) no corresponding anomaly is observed at T_s. Both the underdoped BKFA and SKFA samples show similar temperature dependencies of the A_{1g} and B_{1g} mode linewidths, as observed in the undoped samples, with strong singularities at T_s, followed by a continuous narrowing upon cooling. In particular, the A_{1g} mode of underdoped SKFA narrows by ~ 3 cm^{-1} between T_s and the lowest temperature. In underdoped BKFA the integrated intensity of the A_{1g} and B_{1g} modes breaks in by $\sim 15\%$ at T_s and recovers at T_c. In the underdoped SKFA sample no intensity anomaly is observed at the corresponding T_s (not shown). In optimally doped BKFA (Fig. 5.25) the SDW transition is suppressed.

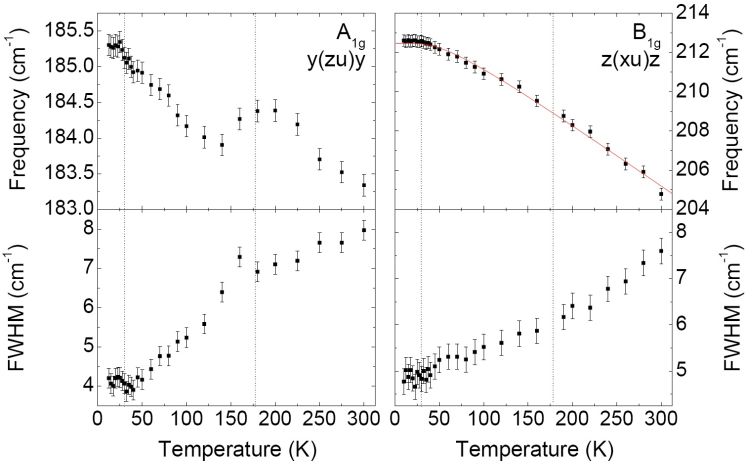

Figure 5.23: Temperature dependence of the frequency and FWHM of the A_{1g} and B_{1g} modes in underdoped SKFA ($x \sim 0.15$) (G15). The vertical lines indicate the critical temperatures $T_c \sim 29$ K and $T_s \sim 178$ K of the superconducting and the SDW phase transition, respectively.

In order to highlight the weaker phonon anomalies in the three different superconducting BKFA and SKFA samples at T_c, the B_{1g} data were fitted to an expression based on phonon-phonon interactions, i.e. the anharmonic decay of phonons, using the data points above T_c (red solid lines) [Men84]. For simplicity a symmetric phonon decay was assumed (see chapter 2.2.1). While the frequencies of the B_{1g} modes in the three samples follow nearly perfectly the expression for anharmonic decay, significant deviations from this behavior are observed for the corresponding A_{1g} modes at T_c. In contrast to the low-temperature saturation of the frequencies of the B_{1g} modes, the A_{1g} modes of the two underdoped BKFA and SKFA samples exhibit a distinct hardening by ~ 0.3 cm^{-1} upon cooling below T_c. Moreover, the linewidth of the A_{1g} mode in SKFA (Fig. 5.23) shows a kink in its temperature dependence at T_c, which can be described as a slight superconductivity-induced broadening superposed on the continuous decrease upon cooling below T_s. While the latter trend is already nearly saturated at $T = T_c$ in SKFA ($x \sim 0.15$), it is much more pronounced in BKFA ($x \sim 0.28$), where T_s is considerably lower and overshadows the superconductivity-induced linewidth anomaly at T_c (Fig. 5.24).

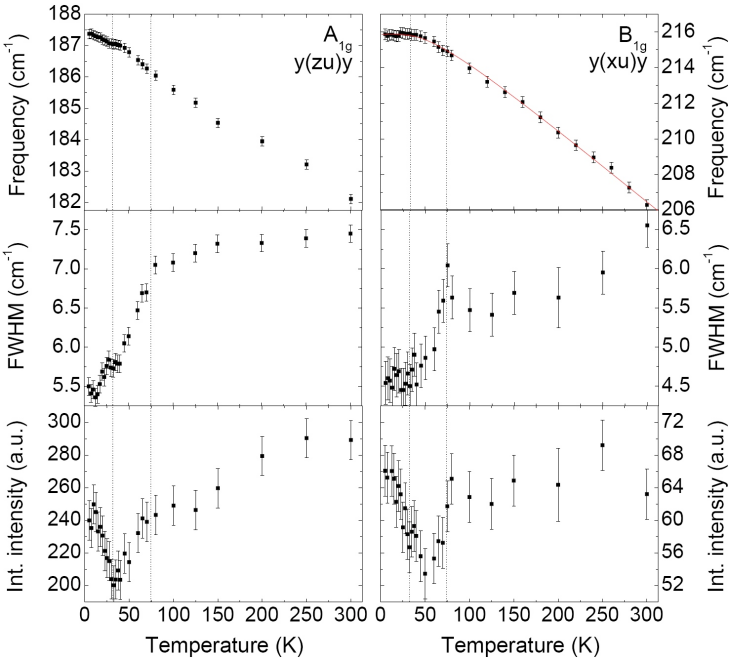

Figure 5.24: Temperature dependence of the frequency, FWHM, and integrated intensity of the A_{1g} and B_{1g} modes in underdoped BKFA ($x \sim 0.28$) (G07). The vertical lines indicate the critical temperatures $T_c \sim 29$ K and $T_s \sim 75$ K of the superconducting and the SDW phase transition, respectively. The red solid line is the result of a fit to the normal-state data, according to anharmonic phonon decay processes (see text for details).

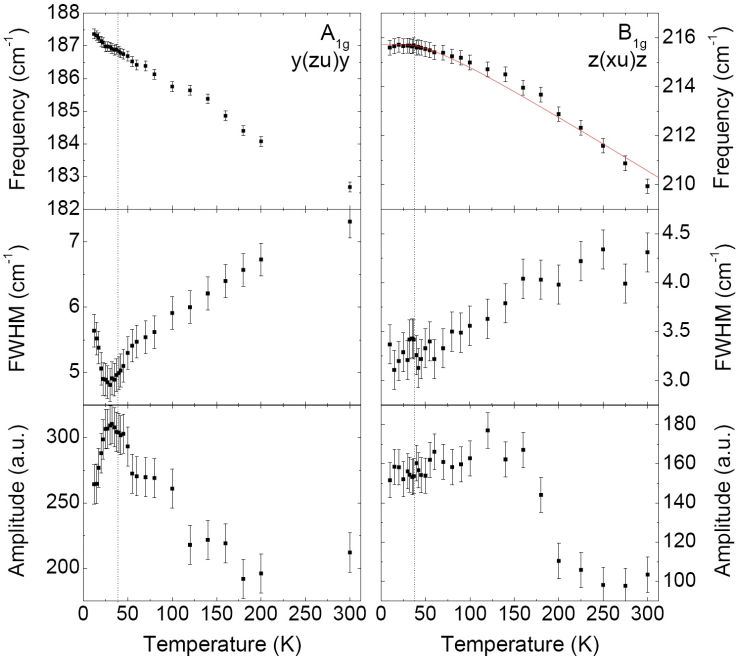

Figure 5.25: Temperature dependence of the frequency, FWHM, and amplitude of the A_{1g} and B_{1g} modes in optimally doped BKFA ($x \sim 0.32$) (G41). The vertical lines indicate the superconducting $T_c \sim 38.5$ K.

In optimally doped BKFA ($x \sim 0.32$), both the frequency and linewidth anomalies at T_c are even more pronounced compared to the underdoped BKFA and SKFA samples (Fig. 5.25). While the A_{1g} mode frequency of optimally doped BKFA hardens by more than ~ 0.5 cm^{-1} upon cooling below T_c, the corresponding linewidth shows a broadening of more than ~ 0.6 cm^{-1}. In figure 5.25 the temperature dependencies of the A_{1g} and B_{1g} mode amplitudes are shown in addition. While the B_{1g} mode shows no amplitude anomaly at T_c, the A_{1g} mode shows a sharp intensity drop at T_c for further cooling. This amplitude anomaly just compensates the linewidth broadening at T_c in agreement with the sum rule. In the integrated intensities of the A_{1g} and B_{1g} modes no anomaly is observed at T_c. On the other hand, the B_{1g} mode amplitude shows a significant decrease of $> 50\%$ between ~ 160 K and ~ 200 K that is not compensated by the linewidth. This amplitude anomaly will be discussed in appendix C.

5.2.2.3 $BaFe_{2-x}Co_xAs_2$

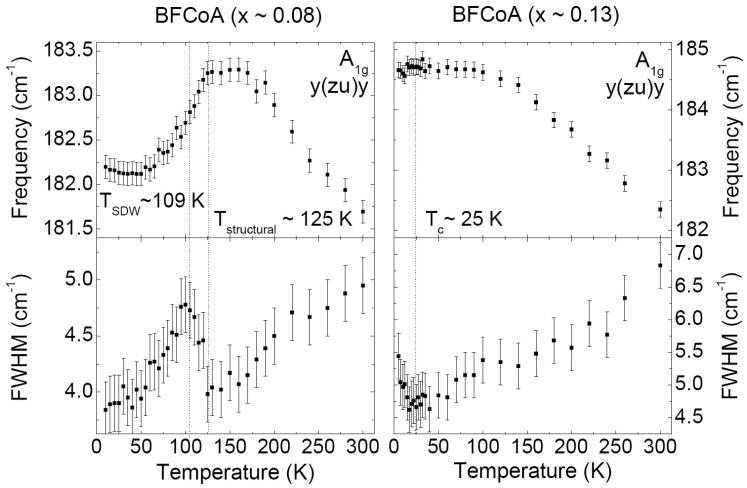

Figure 5.26: Temperature dependence of the frequency and FWHM of the A_{1g} mode in underdoped BFCoA ($x \sim 0.08$) (G64) and optimally doped BFCoA ($x \sim 0.13$) (G33). The vertical lines in underdoped and optimally doped BFCoA indicate the SDW transition $T_{\mathrm{SDW}} \sim 109$ K and the possible onset temperature of the structural transition $T_{\mathrm{structural}} \sim 125$ K, as a guide to the eye, and the superconducting $T_c \sim 25$ K, respectively.

Figure 5.26 shows the frequency and FWHM of the A_{1g} mode in underdoped BFCoA ($x \sim 0.08$) and optimally doped BFCoA ($x \sim 0.13$) in the y(zu)y polarization configuration as a function of temperature. In BFCoA ($x \sim 0.08$) the A_{1g} mode frequency and linewidth show pronounced anomalies at the SDW transition T_{SDW} and at $T_{\mathrm{structural}} \sim 125$ K (indicated by the two vertical lines), which will be attributed below to the possible onset temperature of the structural transition. While the FWHM narrows by more than ~ 0.8 cm^{-1} between T_{SDW} and base temperature, a broadening of similar size is observed between $T_{\mathrm{structural}}$ and T_{SDW}. Concomitantly, the frequency shows a continuous softening by ~ 1 cm^{-1} at $T_{\mathrm{structural}}$ for cooling. In BFCoA ($x \sim 0.13$) the SDW transition is suppressed. In BFCoA ($x \sim 0.08$) the superconducting $T_c \sim 5$ K was at the lower limit of the detection range. While in optimally doped BFCoA no frequency anomaly is observed at $T_c \sim 25$ K, the FWHM shows a small broadening at T_c.

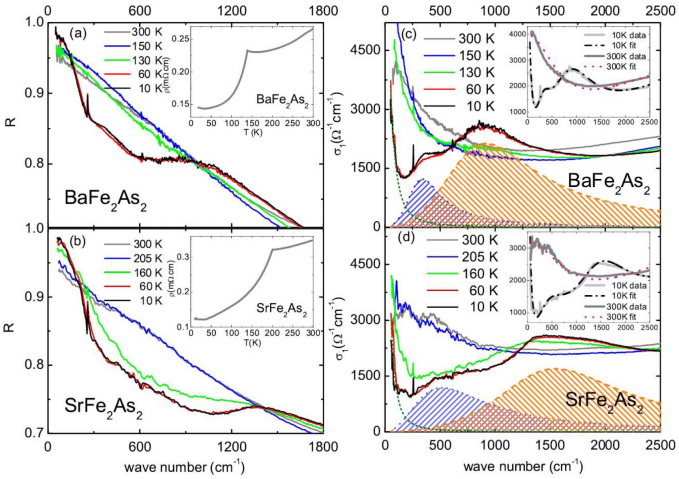

Figure 5.27: Suppression of spectroscopic weight due to opening of SDW gap in undoped BFA and SFA, obtained from optical spectroscopy [Hu08].

5.2.3 Discussion - Phonon anomalies at T_s

In assessing the physical origin of the phonon anomalies at T_s, both the modification of the lattice structure and the opening of the SDW gap at this transition have to be taken into account. The discontinuous jumps in the frequency of the A_{1g} modes in undoped BFA and SFA at T_s are consistent with a first-order structural transition, as suggested by several authors for the ternary iron arsenides [Hua08, Ni08, Kre08], and can be attributed to the contraction of the lattice [Ino09]. While for underdoped SKFA ($x \sim 0.15$) the discontinuity is reduced, it is absent in the underdoped BKFA sample with the higher doping level ($x \sim 0.28$) in agreement with earlier experiments on BKFA samples from the same batch [Ino09], where the structural transition was found to be macroscopically suppressed.

On the other hand, the pronounced and continuous narrowing of both A_{1g} and B_{1g} modes in the pure and hole-doped samples below T_s cannot be understood as a consequence of the modification of the lattice structure and associated phonon-phonon interactions alone. It can, however, be understood if the difference between the linewidths above and below T_s is attributed to the electron-phonon interaction, which becomes inoperative at low temperatures due to the opening of the SDW gap [Hu08], increasing

the phonon lifetime caused by the decrease of the possible scattering channels, i.e. narrowing of the linewidth. This scenario is further supported by infrared experiments on $EuFe_2As_2$ single crystals [Wu09a], where the interaction of the Fe-As vibration E_u with the electronic background was found to be reduced below the SDW transition. The suppression of spectroscopic weight due to the opening of the SDW gap in undoped BFA and SFA, obtained from optical spectroscopy [Hu08], is shown in figure 5.27. The continuous, second-order-like behavior of the linewidth in the pure and hole-doped samples can be reconciled with the abrupt jump in the phonon frequency either if separate first-order structural and second-order SDW transitions take place at slightly different temperatures that are not resolved in the experiment, or if the single, combined transition is weakly first order so that the jump in linewidth is below the detection limit.

In any case, the strong reduction in the linewidths of both A_{1g} and B_{1g} modes below T_s points to a substantial influence of the electron-phonon interaction on the lattice dynamics in the iron arsenides. *Ab initio* density-functional calculations predict that the A_{1g} mode, corresponding to the vibration of the arsenic ions along the c-axis, shows the strongest electron-phonon coupling [Boe08, Yil09b, Yil09a] (see chapter 4.2), in qualitative agreement with the observations. However, calculations without spin polarization fail to account quantitatively for the experimentally observed linewidths above T_s. Using Allen's formula [All72], the predicted density of states at the Fermi level, $N(0) \sim 4.42$/eV [Boe], and total electron-phonon coupling parameter (summed over the phonon branches and averaged on the Brillouin zone), $\lambda = 0.21$ [Boe08, Boe][3], yields a rough estimation of

$$\mathrm{FWHM} = \frac{1}{2}\pi N(0)\frac{\lambda}{15}\omega^2 \sim 0.4\ \mathrm{cm}^{-1}.$$

Note that the factor of 15 reflects the number of phonon branches in BFA. The calculated FWHM is about an order-of-magnitude smaller than observed for the A_{1g} mode above the SDW transition. Due to the large linewidth differences between T_s and base temperature, a temperature-independent offset cannot reconcile this discrepancy. Moreover, it is in

[3]The electron-phonon coupling parameter varies strongly between the different phonon branches, e.g. the vibrations involving Ba or Sr atoms exhibit no electron-phonon coupling [Boe]. In particular, the electron-phonon coupling parameter around the zone center might be considerably larger than the averaged value as suggested from calculations on LaFeAsO [Boe08], resulting in larger corresponding phonon linewidths. Note that a calculation of the electron-phonon coupling parameter directly at the zone center is not possible at the present time due to technical reasons [Boe].

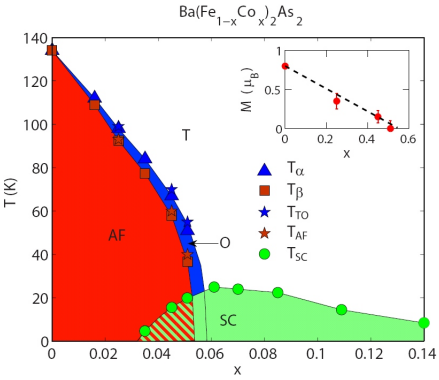

Figure 5.28: Proposed phase diagram of BFCoA [Les09]. T_{TO} (T_α) and T_{AF} (T_β) indicate the structural and SDW phase transitions, respectively.

line with earlier reports of differences between the calculated and observed phonon density of states around the A_{1g} mode energy [Fuk08, Rez09, Mit08, Zbi09]. Since the *ab initio* calculations also show that the electron-phonon coupling greatly increases in the SDW state [Yil09b, Yil09a, Boe09], this may be a manifestation of local Fe moments that survive well above the SDW transition. This scenario is further supported by a report of a quasi-elastic Raman response in undoped SFA [Cho10]. Recent *ab initio* calculations show, indeed, that magnetism enhances the total electron-phonon coupling ($\sim 50\%$) [Boe10] and, therefore, the phonon linewidths, but not enough to fully explain the linewidth discrepancy.

Due to the separation of the structural and SDW phase transitions in electron-doped BFCoA [Les09, Chu09] (see figure 5.28), interesting differences in the temperature dependence of the optical modes in BFCoA are expected compared to the undoped and hole-doped ternary iron arsenides. In BFCoA ($x \sim 0.08$) the softening of the A_{1g} mode frequency at ~ 125 K reminds strongly on the softening in the undoped and hole-doped samples at T_s, which was attributed to the structural phase transition. Note that the size of the softening in BFCoA ($x \sim 0.08$) is comparable to the one in undoped BFA and SFA. Therefore, the onset temperature of the softening in BFCoA ($x \sim 0.08$) can be attributed to the critical temperature of the structural phase transition $T_{\mathrm{structural}} \sim 125$ K, which is slightly above the SDW transition temperature $T_{\mathrm{SDW}} \sim 109$ K. The pronounced continuous softening of the A_{1g} mode frequency at $T_{\mathrm{structural}}$ suggests that the

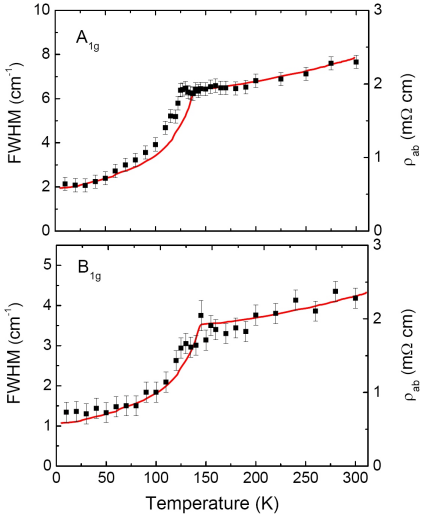

Figure 5.29: Temperature dependence of the FWHM of the A_{1g} and B_{1g} modes and electrical resistivity in undoped BFA (self-flux grown) (G30).

structural phase transition in BFCoA ($x \sim 0.08$) is of second order.

The narrowing of the A_{1g} mode linewidth in BFCoA ($x \sim 0.08$) at T_{SDW} is in line with the corresponding phonon anomalies in the undoped and hole-doped samples at T_s, which were attributed to the opening of the SDW gap. However, the narrowing in BFCoA ($x \sim 0.08$) is considerably smaller and the broadening between $T_{\mathrm{structural}}$ and T_{SDW} emphasizes the existence of two separated threshold temperatures, $T_{\mathrm{structural}} > T_{\mathrm{SDW}}$. The smaller narrowing in BFCoA ($x \sim 0.08$) at T_{SDW} indicates that the amplitude of the SDW gap might be reduced or the electron-phonon interactions are weaker. The linewidth increase (Fig. 5.26) ahead of the narrowing at T_{SDW} is reminiscent of the linewidth behavior in undoped SFA at T_s (Fig. 5.22), which might be indicative for a slight separation of the structural and SDW transitions in temperature also in undoped SFA.

In figure 5.29 the temperature dependencies of both the FWHM of the A_{1g} and B_{1g} modes in undoped BFA (self-flux grown) and the corresponding electrical resistivity $\rho(T)$ are plotted together in the same diagrams. The FWHM data strongly resemble the temperature dependence of the electrical resistivity between 300 K and the lowest temperature over the

SDW transition at $T_s \sim 138$ K. The small shift between the FWHM data and $\rho(T)$ in temperature can be attributed, e.g., to a small sample heating through the laser beam outside the estimated error bar of 5 K. Due to the metallic behavior of the ternary iron arsenides, the Drude model gives a first plausible explanation of this observation. Due to the Heisenberg uncertainty principle, FWHM $\sim 1/$(lifetime of phonon). In case of a constant electronic density of states at the Fermi level n and if one identifies the lifetime of a phonon with the electronic relaxation time τ, one has

$$\rho(T) = \frac{m}{ne^2\tau} \sim \text{FWHM},$$

where m is the mass of a free electron at the Fermi level and e is the elementary charge of an electron. The parallel temperature dependence of the FWHM and $\rho(T)$ over the SDW transition at T_s seems surprising, because one naively expects the electronic density of states n to decrease for cooling below T_s due to the opening of the SDW gap, what would lead to an resistivity increase instead of the observed decrease. Therefore, the experimental data suggest that n does not change considerably at T_s, indicative for a not fully opened SDW gap on the Fermi surface, as proposed recently in [Cho10]. Furthermore, the SDW order might lead to a decrease of inter-electronic scattering compensating for a small decrease in n. Note that additional contributions might come from the structural transition.

5.2.4 Discussion - Phonon anomalies at T_c

According to the standard description of superconductivity-induced self-energy anomalies of optical phonons [Zey90, Tho91, Dev94] (see chapter 2.2.2), the rearrangement of the electronic density of states below T_c is expected to induce hardening (softening) and broadening for phonons with energies above (below) the pair-breaking energy 2Δ. Experimental observations on the hole-doped cuprate high-temperature superconductors, like e.g. on $YBa_2Cu_3O_{7-x}$, are largely consistent with this theory [Bak09].

Angle-resolved photoemission spectroscopy (ARPES) on underdoped BKFA ($x \sim 0.28$) samples from the same batch as used for the Raman experiments found two superconducting gap energies at $\Delta_1 \sim 9$ meV and $\Delta_2 \sim 4$ meV [Evt09], yielding pair-breaking energies of $2\Delta_1 \sim 150$ cm^{-1} and $2\Delta_2 \sim 65$ cm^{-1}. For nearly optimally doped BKFA ($T_c = 37$ K) gap energies of $\Delta_1 \sim 12$ meV and $\Delta_2 \sim 6$ meV were determined [Din08]. Figure 5.30 shows the intensity and momentum dependence of the superconducting gap in underdoped BKFA ($x \sim 0.28$) together with a Fermi surface

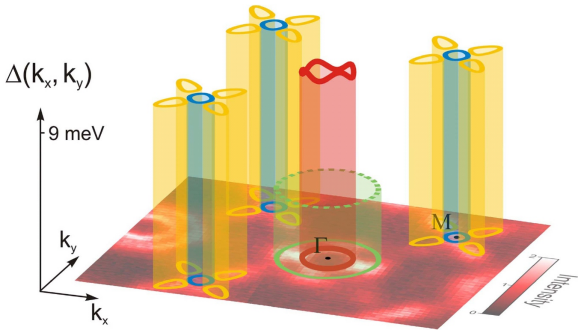

Figure 5.30: Amplitude and momentum dependence of the superconducting gaps in underdoped BKFA ($x \sim 0.28$) with underlying Fermi surface map in the basal plane, obtained from ARPES measurements [Evt09].

map, obtained from the ARPES measurements [Evt09]. The Fermi surface consists of different bands with two hole-like pockets centered at the Γ point and an electron pocket with hole-like "propellers" centered at the M points in the Brillouin zone [Zab09]. The superconducting gap opens on the different Fermi pockets with different amplitudes. Note that the macroscopic wave function of the superconducting state has different signs on the different pockets centered at the Γ and M points ($s^{\pm}$-symmetry).

Assuming comparable gap values for the two underdoped BKFA ($x \sim 0.28$) and SKFA ($x \sim 0.15$) samples, both the A_{1g} and B_{1g} mode energies are well above the upper $2\Delta_1$ gap. The experimental observations of a hardening and broadening in the phonon frequency and linewidth at T_c are therefore in agreement with the theoretical expectations. Note that a similar hardening in the B_{1g} mode frequency was recently found in underdoped SKFA ($T_c \sim 28$ K) [Cho10]. The observation of stronger phonon anomalies for the A_{1g} mode compared to the B_{1g} mode at T_c might be due to the closer distance of the A_{1g} mode energy to the expected coherence peak in the electronic density of states at 2Δ (see chapter 2.1.3). On the other hand, due to symmetry reasons, the B_{1g} mode only hardly interacts with the Fermi surface in the iron pnictides (see chapter 2.1.4). In case of an upper gap energy of $\Delta_1 \sim 12$ meV for optimally doped BKFA, the A_{1g} mode is sited very close to the upper $2\Delta_1$ gap, expecting larger phonon self-energy renormalizations due to larger redistributions in the electronic density of states compared to the underdoped samples (see chapter 2.2.2).

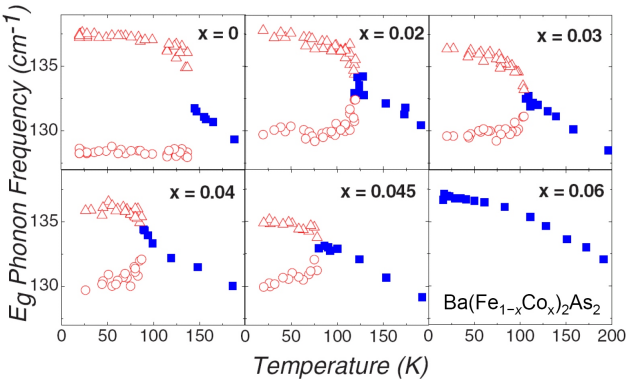

Figure 5.31: Temperature evolution of low-frequency E_g mode in BFCoA for different doping levels, obtained from Raman light scattering [Cha09].

The larger phonon anomalies found in the A_{1g} mode in optimally doped BKFA ($x \sim 0.32$) at T_c are in agreement with this expectation. However, more subtle phonon self-energy renormalizations around the 2Δ gap, due to competing superconducting instabilities, as proposed recently from electronic Raman scattering on optimally doped BFCoA single crystals [Mus09], have also to be taken into account. Nonetheless, the observed phonon self-energy renormalizations in the different ternary iron arsenide samples at T_c are very small compared to typical phonon anomalies in the cuprate high-temperature superconductors at T_c [Bak09]. This indicates that the superconductivity-induced modification of the electronic density of states in the ternary iron arsenides is small at the phonon energies monitored experimentally. Moreover, the symmetric phonon line shapes without indications of Fano-like asymmetry indicate a weak product of the electron-phonon coupling with the number of electronic decay channels.

5.2.5 Splitting of in-plane E_g modes

At the structural phase transition from tetragonal to orthorhombic the symmetry between the a- and b-axis of the tetragonal high temperature phase is broken. As a consequence, the doubly degenerate in-plane E_g modes, corresponding to lattice vibrations along the a- and b-directions, are expected to split in energy. This splitting was recently observed in BFCoA single crystals by Raman light scattering [Cha09] (see figure 5.31).

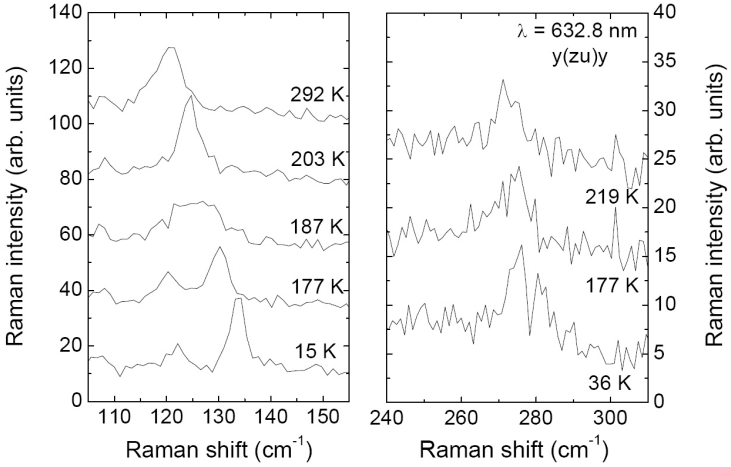

Figure 5.32: Raman spectra of undoped SFA (G12) with focus on the low-energy and high-energy E_g modes for different temperatures ($T_s \sim 202$ K).

Figure 5.32 shows the Raman spectra of undoped SFA with focus on the two E_g modes for different temperatures. Both E_g modes also show a clear splitting upon cooling below the structural phase transition. In figure 5.33 the temperature evolution of the low-frequency E_g mode in undoped SFA and BFA (self-flux grown + tin flux grown) and underdoped SKFA ($x \sim 0.15$) and BKFA ($x \sim 0.28$) are shown. For undoped SFA the corresponding integrated intensity is added. A reliable analysis of the high-frequency E_g modes was not possible, due to very weak intensities. While undoped SFA and BFA (self-flux grown), and underdoped SKFA show pronounced splittings at T_s, underdoped BKFA ($x \sim 0.28$) shows only the standard temperature dependence of phonon anharmonicity without splitting, in agreement with the suppression of the macroscopical change of the lattice symmetry for this doping level [Ino09]. The splitting in the undoped BFA (tin flux grow) sample appears comparable to the one in BFA (self-flux grown), but is shifted to ~ 100 K in-line with the shifted anomalies of the other modes due to tin contamination (see chapter 5.2.2.1).

In [Cha09] a splitting amplitude of the low-frequency E_g mode in undoped BFA of ~ 9 cm^{-1} at low temperatures was observed, which fits well to the observations in the two BFA samples grown in different flux. Compared to this, the splitting amplitude in undoped SFA ~ 12 cm^{-1} ($> 9\%$

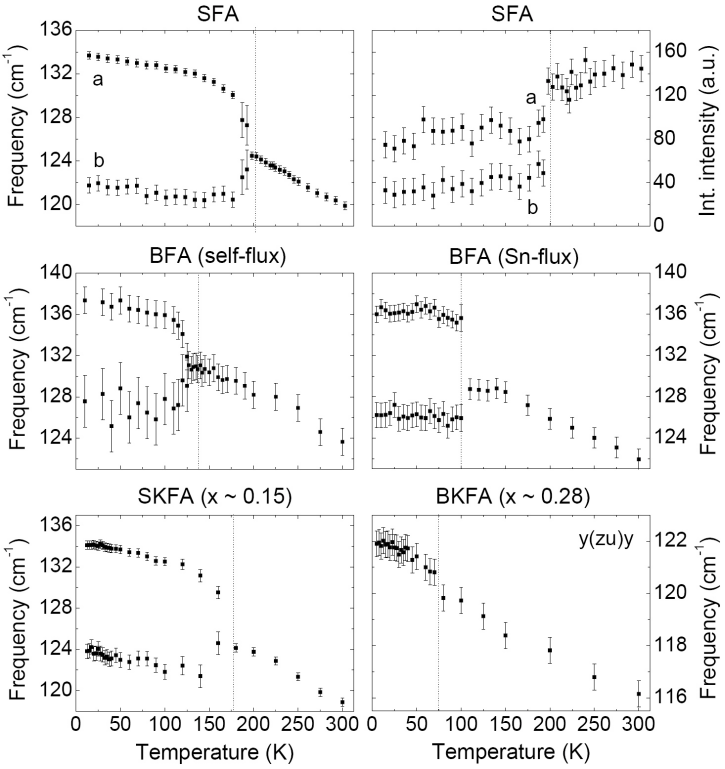

Figure 5.33: Temperature dependence of low-frequency E_g mode in undoped SFA (G12), undoped BFA (self-flux grown (G30) + tin flux grown (G23)), underdoped SKFA ($x \sim 0.15$) (G15), and underdoped BKFA ($x \sim 0.28$) (G07). For undoped SFA the integrated intensity is added. (The vertical lines indicate the critical temperatures of the structural phase transition. **a** and **b** indicate the split E_g branches below the transition.)

of the mode energy) is even more pronounced. As shown in [Cha09], the splitting amplitude is anomalously large and cannot be explained by the orthorhombic distortion alone. As a possible explanation, strong spin-phonon coupling was proposed [Cha09]. If this was the case, the effective coupling in SFA would still be $> 25\%$ larger than in BFA. In underdoped SKFA ($x \sim 0.15$) the splitting amplitude is ~ 10 cm^{-1}, reflecting the suppression of the structural transition at T_s for increasing doping.

In undoped SFA the integrated intensity of the low-frequency E_g mode (Fig. 5.33) is non-symmetrically distributed among the split E_g branches below the structural phase transition at T_s. The integrated intensity of the branch with the higher energy (a) compared to the branch with the lower energy (b) shows a ratio of $\sim 2:1$, which sum up to approximately the integrated intensity above T_s. This intensity difference may arise from differences in the electronic and phononic Raman efficiencies, e.g. due to anisotropic electron-phonon interactions between the a- and b-axis. On the other hand, a nonsymmetric distribution of the Raman integration area to twinned orthorhombic domains could provide another possible origin.

5.2.6 Electronic background anomalies

In the metallic iron-based superconductors electronic Raman scattering is difficult, because charge density variations are screened by the itinerant electrons [Dev07]. In accordance with these difficulties, no electronic background anomalies could be resolved at the superconducting and SDW phase transitions in the undoped and underdoped ternary iron arsenide samples with the used setup. A possible origin for very weak electronic background anomalies at T_s, while the optical modes show strong anomalies, could be a not fully opened SDW gap on the Fermi surface [Cho10].

In figure 5.34 the Raman response of optimally doped BKFA ($x \sim 0.32$) (batch (G41) and (G53)) is shown for the z(xu)z polarization configuration (A_{1g}+B_{1g}+B_{2g} symmetry) above and below T_c. In order to highlight possible redistributions in the electronic background at T_c, the high-temperature Raman spectra are subtracted from their analogs below T_c. In the subtraction plots, significant humps in both optimally doped BKFA samples centered slightly above ~ 200 cm^{-1} are observed. These humps might be interpreted as "coherence peaks", due to redistributions of the electronic states below T_c (see chapter 2.1.3), which would be in agreement with the expected energy for the upper superconducting gap $\Delta_1 \sim 12$ meV [Din08]. However, despite of the similar observations in both optimally

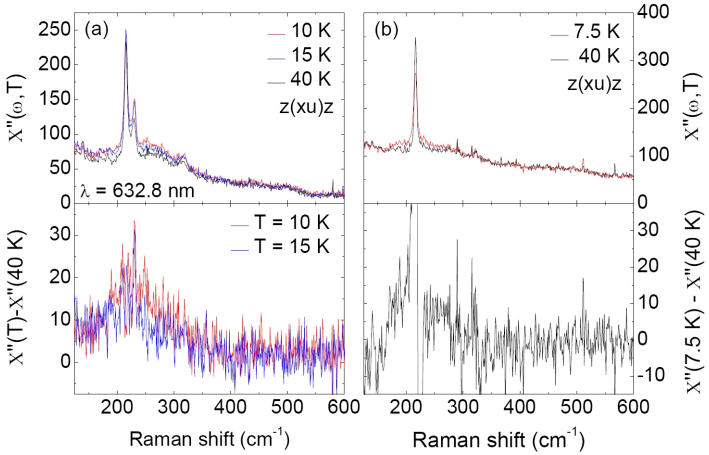

Figure 5.34: (*top*) Raman response of optimally doped BKFA ((a) batch (G41) and (b) batch (G53)) above and below $T_c \sim 38.5$ K for z(xu)z polarization configuration (A_{1g}+B_{1g}+B_{2g} symmetry); (*bottom*) Raman response below T_c subtracted from Raman response above T_c at 40 K.

doped BKFA samples, the humps were not fully reproducible. It could not be clarified, if the humps are artifacts, accidentally centered at the energy of the superconducting 2Δ gap, or are due to aging effects induced by the laser. Note that in Co-doped samples of $BaFe_2As_2$ close to optimal doping a coherence peak due to the opening of the superconducting gap was observed slightly below $\sim$ 100 cm^{-1} [Mus09, Cha10]. For further studies on the electronic background a modified Raman setup with flat angles between incident laser light and sample surface might be more helpful.

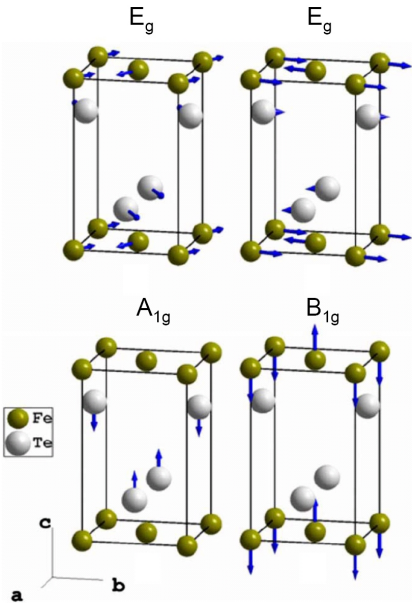

Figure 5.35: Displacement patterns of the Raman-active optical modes in the iron chalcogenides, as obtained from LDA calculations [Xia09].

5.3 $Fe_{1+y}Se_xTe_{1-x}$

5.3.1 Mode assignment

From the tetragonal PbO-type crystal structure of the iron chalcogenides [space group P4/nmm] (see chapter 4.3) one expects four Raman-active optical modes with symmetries A_{1g}+B_{1g}+2E_g [Xia09]. Figure 5.35 shows the displacement patterns of the four Raman-active optical modes, as obtained from local density approximation (LDA) calculations [Xia09]. The four modes are very similar to the corresponding ones in the ternary iron arsenides (see figure 5.18), except a replacement of As by Te as the main difference. Note that due to symmetry reasons, the unit cell in the iron chalcogenides is shifted by half a unit cell along the *a*- or *b*-direction with respect to the one in the ternary iron arsenides. The selection rules of the four Raman-active modes in the iron chalcogenides are the same as for the corresponding modes in the ternary iron arsenides, listed in table 5.2.

The Raman measurements on the iron chalcogenides were exclusively performed with the "micro" setup using the 50x microscope objective. In order to maximize the Raman intensity, a polarization analyzer was not used. Figure 5.36 shows the Raman spectrum of the $Fe_{1.05}Se_{0.42}Te_{0.58}$ single crystal at 300 K in the z(xu)z polarization configuration for $\lambda =$ 632.8 nm laser excitation. According to the mode assignment in [Xia09], the peaks at ~ 156.6 and ~ 198.8 cm^{-1} can be identified with the A_{1g} and B_{1g} vibrations of the Te and Fe atoms, respectively. The two in-plane E_g modes cannot be observed for z(xu)z polarization in accordance with the Raman-selection rules (see table 5.2). The inset shows a comparison of corresponding Raman spectra at 5, 70, and 300 K. In particular, the B_{1g} mode shows significant shifts in energy for the different temperatures.

The Raman spectra of the $Fe_{1.05}Se_{0.42}Te_{0.58}$ and $Fe_{1.08}Se_{0.28}Te_{0.72}$ single crystals appeared very similar. In contrary to previous Raman measurements on $Fe_{1.03}Se_{0.3}Te_{0.7}$ [Xia09], where the A_{1g} mode was not observed and where it was stated that 30% Se substitution for Te suppresses the Te vibration [Xia09], the A_{1g} mode is clearly observed in the present Raman study for both 28% and 42% Se-doping concentrations. Moreover, the B_{1g} mode of Fe appears approximately at the same energy in the undoped $Fe_{1.08}Te$ and the two doped FST samples. The A_{1g} and B_{1g} modes in the two FST samples are shifted to lower energies compared to the corresponding modes in the ternary iron arsenides, in agreement with previous observations [Xia09]. In particular, the B_{1g} mode of $Fe_{1.05}Se_{0.42}Te_{0.58}$ is shifted by ~ 10 cm^{-1} compared to the corresponding mode in $BaFe_2As_2$. Since Te/Se is heavier than As, this shift can be partly attributed to the mass difference. In addition, the different atomic sizes of Te/Se compared to As and the missing Ba layers in FST modify the crystal structure.

Inset (a) of figure 5.37 shows a comparison of typical Raman spectra of FST, obtained from a freshly cleaved surface and an aged surface after several hours in air at 300 K, respectively. While the B_{1g} mode experiences only an intensity decrease with aging, the A_{1g} mode shows more dramatic changes. The aged "A_{1g} peak" is strongly broadened, much more intense, and seems to consist of two modes at ~ 143 cm^{-1} and ~ 130 cm^{-1}, i.e. the "A_{1g} peak" is centered at significantly lower energies compared to the A_{1g} mode obtained from the freshly cleaved surface. Similar effects were previously reported in [Xia09]. Figure 5.37 shows the Raman spectrum of the freshly cleaved plane surface of the undoped $Fe_{1.08}Te$ sample at 100 K. While the B_{1g} mode appears comparable to the one in the FST samples, the "A_{1g} peak" in the $Fe_{1.08}Te$ sample shows the typical features of aging.

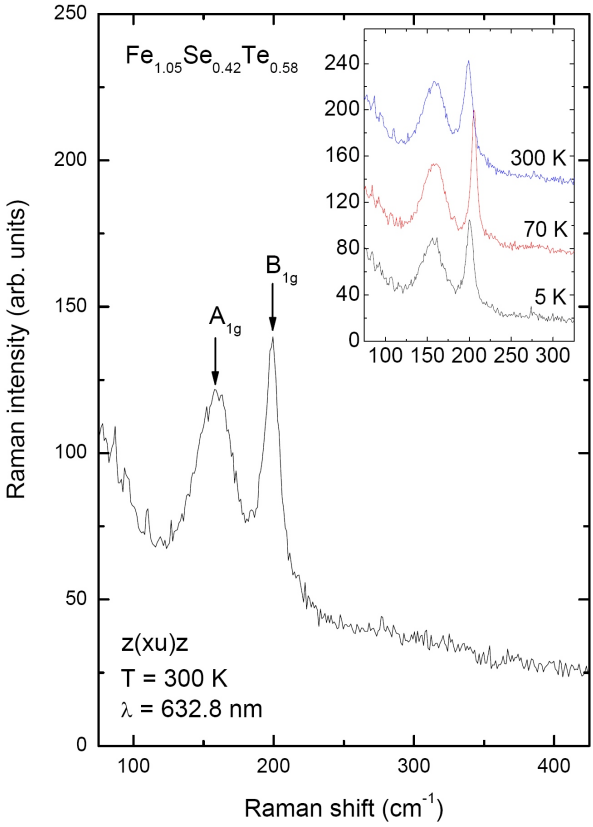

Figure 5.36: Raman spectrum of $Fe_{1.05}Se_{0.42}Te_{0.58}$ (batch 42) at 300 K in z(xu)z polarization configuration for $\lambda = 632.8$ nm laser excitation. The inset shows the corresponding Raman spectra at different temperatures.

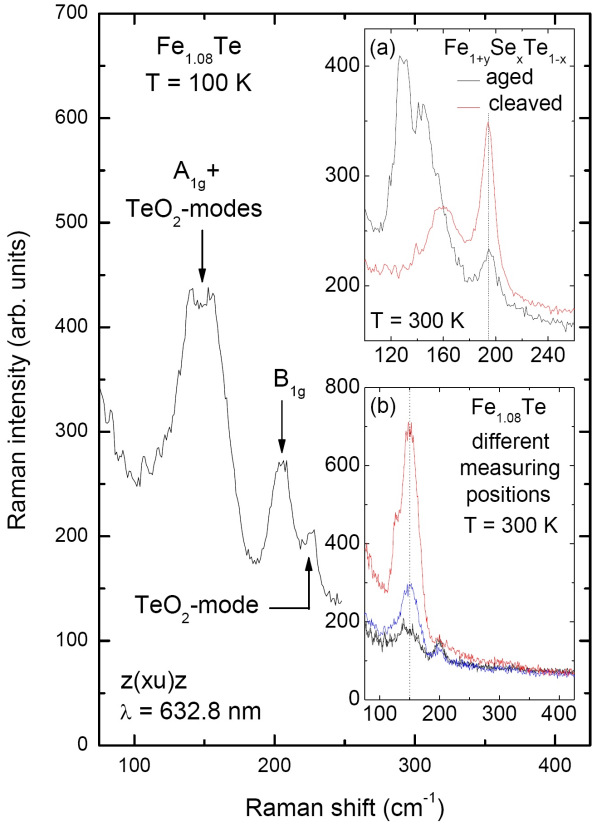

Figure 5.37: Raman spectrum of the undoped $Fe_{1.08}Te$ (batch 21) sample at 100 K in z(xu)z polarization configuration for $\lambda = 632.8$ nm laser excitation. Inset (a): Typical Raman spectra of doped FST samples, obtained from a freshly cleaved surface and an aged surface after several hours in air at 300 K, respectively; inset (b): Raman spectra of the $Fe_{1.08}Te$ (batch 21) sample at different measuring positions on the sample surface at 300 K.

Furthermore, a small additional mode is observed on the right shoulder of the B_{1g} mode at ~ 227 cm^{-1}. Cleaving the $Fe_{1.08}Te$ sample again could not remove the aging effects. Inset (b) of figure 5.37 shows corresponding Raman spectra of the $Fe_{1.08}Te$ sample at different measuring positions on the sample surface at 300 K. The aging features appear similarly at all different measuring positions, however, with different magnitude. In particular, the amplitude of the "A_{1g} peak" varies by more than a factor of 4.

The aging effects in the different iron chalcogenide samples suggest that the FST system is not stable in air. In [Xia09] it was stated that the aging features in the Raman spectrum of FST are due to a decomposition effect, most likely into amorphous Te rather than TeO_2. In order to assign the aging features in FST to amorphous Te, an old Raman reference spectrum, which shows very similar features, was used [Pin71]. However, the report about this reference spectrum [Pin71] contains a correction added after the proof, saying that the spectrum attributed to amorphous Te has actually to be attributed to tetragonal TeO_2. According to this, the aging features in the studied FST samples should be attributed to TeO_2. In agreement with this assignment, the additional mode in the undoped $Fe_{1.08}Te$ sample at ~ 227 cm^{-1} can be attributed to a B_1 Raman-active optical mode of TeO_2 [Pin72]. Because of the overall presence of the aging features in the undoped $Fe_{1.08}Te$ sample, the Se-free sample seems to be uniformly contaminated with TeO_2, probably formed during crystal growth. On the other hand, the FST samples including Se show no indication for a uniform contamination with TeO_2, but show a decomposition into TeO_2 under exposure to air. Other decomposition products cannot be excluded.

5.3.2 Phonon anomalies

Figure 5.38 shows the frequency and FWHM of the B_{1g} mode of the undoped $Fe_{1.08}Te$ and the doped $Fe_{1.05}Se_{0.42}Te_{0.58}$ and $Fe_{1.08}Se_{0.28}Te_{0.72}$ samples as a function of temperature. The vertical lines correspond to the combined transition temperature T_N to long-range commensurate magnetic order with monoclinic structural distortion in the Se-free and the temperatures T_{IC} below which short-range incommensurate spin fluctuations have been reported for Se-doping (see chapter 4.3). The upper vertical line in the sample with 42% Se concentration indicates the onset temperature of the short-range magnetic fluctuations, while the lower one indicates the temperature, where the magnetic fluctuations increase more rapidly. The B_{1g} frequency data were fitted by an expression based on

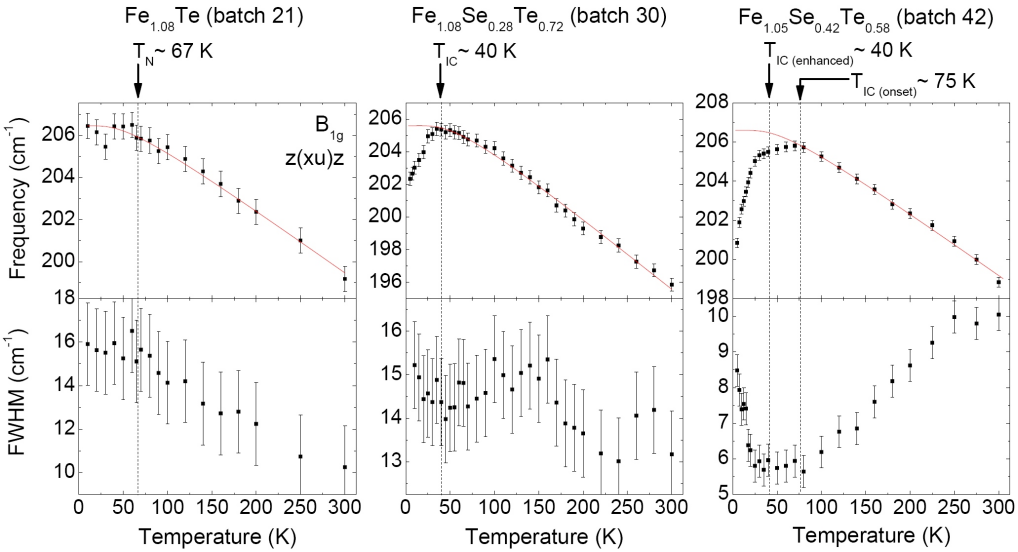

Figure 5.38: Temperature dependence of the frequency and FWHM of the three iron chalcogenide samples. The vertical lines correspond to the combined transition temperature to long-range commensurate magnetic order with monoclinic structural distortion T_N (batch 21) and the transition temperatures to short-range incommensurate spin fluctuations T_{IC} (batch 30 and 42). The red solid lines are the result of fits to the data above the magnetic transitions according to anharmonic phonon decay processes (see text for details).

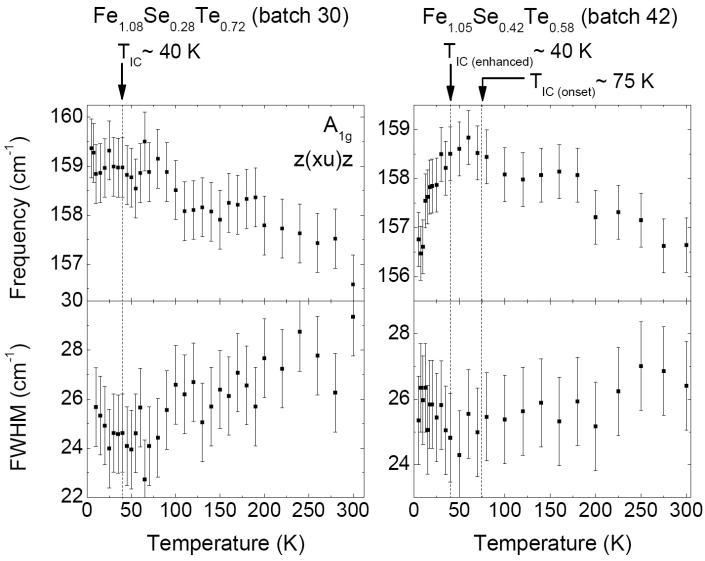

Figure 5.39: Temperature dependence of the frequency and FWHM of the two Se-doped iron chalcogenide samples. The vertical lines indicate the corresponding magnetic transition temperatures (see text for details).

phonon-phonon interactions, i.e. the anharmonic decay of phonons, using the data points above the magnetic transitions (red solid lines) [Men84]. For simplicity a symmetric phonon decay was assumed (see chapter 2.2.1).

While the B_{1g} mode frequency of the undoped $Fe_{1.08}Te$ sample follows nearly perfectly the expression for anharmonic decay, the doped samples with 28% and 42% Se concentrations show significant deviations from this behavior at the corresponding transition temperatures T_{IC} to short-range incommensurate spin fluctuations. Both Se-doped samples exhibit a pronounced continuous softening upon cooling below T_{IC} with respect to the standard anharmonic lines. In particular, the B_{1g} mode frequency in the $Fe_{1.05}Se_{0.42}Te_{0.58}$ sample starts to soften at the onset temperature of the short-range incommensurate spin fluctuations $\sim$ 75 K with a strongly enhanced softening at $\sim$ 40 K, where a rapid correlation increase of the magnetic fluctuations was observed (see chapter 4.3), yielding an overall softening of ~ 5 cm^{-1} between 75 K and the lowest temperature. On the other hand, the B_{1g} mode frequency in the $Fe_{1.05}Se_{0.42}Te_{0.58}$ sample starts

to soften at $T_{IC} \sim 40$ K with an overall softening of ~ 3 cm^{-1}. While the B_{1g} mode FWHM in the Se-free and the sample with 28% Se concentration shows no anomaly at T_N and T_{IC}, respectively, the corresponding FWHM of the sample with 42% Se concentration shows a strong increase of nearly 3 cm^{-1} between $T_{IC} \sim 40$ K and base temperature. While the overall temperature dependence of the FWHM in the sample with 42% Se concentration shows the standard behavior above T_{IC}, as expected for phonon anharmonicity, the Se-free sample shows an anomalous opposite trend with a linewidth change of comparable amplitude. In the sample with 28% Se the temperature dependence of the FWHM is somewhere in between.

Figure 5.39 shows the frequency and FWHM of the A_{1g} mode of the two Se-doped samples as a function of temperature. In the undoped $Fe_{1.08}Te$ sample the A_{1g} mode is overshadowed by the "aging effects" and cannot be analyzed. While the A_{1g} mode in the sample with 28% Se shows no anomalous behavior outside the error bars in the temperature dependence at $T_{IC} \sim 40$ K, the A_{1g} mode frequency of the sample with 42% Se shows a softening of ~ 2 cm^{-1} between ~ 40 K and the lowest temperature.

The superconducting transition temperatures of the two Se-doped samples were close to the lower temperature limit of the experimental detection range of the used setup. In both samples no anomalous behavior in the temperature dependence of the optical modes was observed at T_c.

5.3.3 Discussion

The phonon anomalies in the iron chalcogenide samples exhibit a fundamentally different behavior compared to the ternary iron arsenides. The undoped parent compound FeTe (here $Fe_{1.08}Te$) shows no phonon anomaly at the combined structural-SDW phase transition T_N with no indication for the opening of a SDW gap in the electronic continuum in agreement with previous investigations [Xia09, Che09b]. On the other hand, the Se-doped FST samples show very strong phonon anomalies at the onset temperatures to short-range incommensurate spin fluctuations T_{IC}. In contrast to this, in the ternary iron arsenides the strongest phonon anomalies are observed at the combined structural-SDW phase transition T_s in the undoped parent compounds $BaFe_2As_2$ or $SrFe_2As_2$ that are increasingly suppressed with doping. Moreover, the softening in the B_{1g} mode frequency in the Se-doped FST samples at T_{IC} is much stronger compared to the corresponding phonon anomalies in $BaFe_2As_2$ or $SrFe_2As_2$ at T_s.

The pronounced phonon softening in FST indicates a strong spin-

phonon coupling [Lav06, Gra99]. The experimental results, obtained from the FST samples, suggest the following picture. In undoped $Fe_{1+y}Te$ the spin-phonon interaction is weak for long-range commensurate AFM order, but becomes strongly enhanced in the presence of short-range incommensurate spin-fluctuations in Se-doped samples, inducing anomalously large shifts in the phonon frequencies. The continuous softening of the B_{1g} mode at T_{IC} points to a significant cross-over at this temperature. According to the differences in the softening between the $Fe_{1.05}Se_{0.42}Te_{0.58}$ and $Fe_{1.08}Se_{0.28}Te_{0.72}$ samples, the softening amplitude might depend on the exact amount of iron excess like the transition temperature T_{IC}. On the other hand, the change of the temperature dependence of the B_{1g} mode linewidth from anomalous to standard behavior for increasing Se concentrations underlines a drastic change of the physical properties of FST with doping. Note that both the Se-free and the $Fe_{1.08}Se_{0.28}Te_{0.72}$ sample, containing similar amounts of iron excess, show an anomalous temperature dependence of the phonon linewidth, while the $Fe_{1.05}Se_{0.42}Te_{0.58}$ sample with the lower amount of iron excess shows a standard behavior. This separation might also indicate an influence of the iron excess concentration on the linewidth behavior in FST. The broad phonon linewidths in the Se-free sample at low temperature indicate the presence of crystallographic inhomogeneities in this sample, while the considerably smaller linewidths in the $Fe_{1.08}Se_{0.28}Te_{0.72}$ sample indicate a higher crystal quality.

The experimental results on the iron chalcogenide samples indicate the presence of interesting physical phenomena observable in the phononic system. However, more experiments with different concentrations of iron excess and Se-doping are necessary to study these effects in detail.

Chapter 6

Summary

All materials studied in this work can be characterized by a strong interplay between antiferromagnetic ordering phenomena and superconductivity. The strategy to study this interplay was Raman light scattering with focus on phonon anomalies in the temperature dependence of optical phonons. The Raman scattering technique was used to resolve phonon anomalies that are difficult to observe by other experimental techniques and as very sensitive tool to study the crystallographic microstructure.

In the first project, two molecular-beam-epitaxy-grown films of the electron-doped superconductor $La_{2-x}Ce_xCuO_4$ (LCCO) close to optimal doping (slightly underdoped and slightly overdoped), which had been the basis of prior transport measurements [Wag08a, Wag08b, Mül06], were characterized in detail by various experimental techniques with focus on a microstructural analysis. The very complex materials physics of electron-doped cuprates often leads to contradicting experimental results, but detailed information about the corresponding crystal quality is rare. The presented results revealed hidden micron-sized inclusions (Cu_2O and others) in both films, providing detailed information about the microstructure in typical state-of-the-art LCCO films. The different inclusions motivate to consider and maybe reconsider contradicting experimental results in related compounds in view of possible impurity phases, e.g. in transport measurements. Furthermore, this work can be used as a reference, when improving the sample quality in crystal growth. The Raman light scattering data on LCCO, shown in this work, are the first reported so far. In the temperature dependence of both the Cu_2O modes and oth-

ers that can be assigned to the LCCO matrix in the slightly underdoped LCCO film completely unexpected phonon anomalies were found upon cooling below $T \sim T_c$ that are not explained by the standard theory of phonon self-energy renormalization. Control measurements on commercial Cu_2O powders and a comparison to prior Raman light scattering studies on other high-temperature superconductors motivated the speculation that proximity effects at the LCCO/Cu_2O interface may be responsible for these anomalies. Experiments on the slightly overdoped LCCO film did not reveal comparable phonon anomalies. A systematic study of phonon anomalies, like observed in LCCO, appears worthwhile using related materials with different doping levels and other experimental methods. An interesting candidate for further studies are $Nd_{2-x}Ce_xCuO_4$ films.

In the second project, different superconducting and non-superconducting single crystals of the ternary iron arsenides $BaFe_2As_2$ (BFA), $SrFe_2As_2$ (SFA), $Ba_{1-x}K_xFe_2As_2$ (BKFA) and $Sr_{1-x}K_xFe_2As_2$ (SKFA) (hole-doped), and $BaFe_{2-x}Co_xAs_2$ (BFCoA) (electron-doped) with different doping concentrations were studied. The presented Raman study on these samples is one of the first systematic analyses of Raman spectra of the iron pnictides. It was shown that the electron-phonon coupling results in significant phonon anomalies in the temperature dependence of the optical modes at both the structural and spin-density wave (SDW) phase transitions and the superconducting phase transition, respectively. The Raman data provide fundamental information about the character of these phase transitions with high resolution. In the undoped and hole-doped samples a pronounced continuous narrowing of the Raman-active Fe and As vibrations upon cooling below the SDW phase transition at T_s was observed. This effect is qualitatively consistent with a second-order-like opening of the SDW gap. A quantitative description of these anomalies requires theoretical work beyond the density-functional calculations thus far reported. The presented experimental results imply that local magnetic moments may survive well above T_s and have to be included in the calculations. Discontinuous jumps in the phonon frequencies and anomalously large splittings of the in-plane modes at T_s are consistent with a first-order structural phase transition accompanying the SDW transition. These anomalies are continuously suppressed for increasing doping concentrations. In the hole-doped samples the structural and SDW phase transitions are supposed to appear at the same temperature T_s. Therefore, the second-order-like SDW transition is reconciled with the first-order structural transition either, if both transitions take place at slightly dif-

ferent temperatures that are not resolved in the experiment, or if both transitions are combined weakly first order. The corresponding phonon anomalies in the electron-doped samples are in agreement with a splitting of the structural and SDW phase transitions in temperature. The phonon anomalies at the superconducting phase transition T_c are small, but consistent with the theory of superconductivity-induced phonon self-energy modifications for the cuprate high-temperature superconductors.

In the third project, three different superconducting and non-superconducting single crystals of the iron chalcogenide systems $Fe_{1+y}Te$ and $Fe_{1+y}Se_xTe_{1-x}$ (FST) with different concentrations of Se-doping and Fe excess were studied. The presented Raman study on these samples is the first temperature-dependent analysis of Raman spectra of the iron chalcogenides. Despite a similar crystal structure compared to the iron pnictides, the experimental results on the iron chalcogenides suggest that this class of materials exhibits a fundamentally different behavior. In undoped $Fe_{1+y}Te$ no phonon anomaly was observed at the transition temperature to long-range antiferromagnetic order T_N that is accompanied with a structural phase transition. On the other hand, for Se-doping pronounced phonon anomalies were observed at the onset temperature of short-range incommensurate spin-fluctuations T_{IC}. These phonon anomalies are surprisingly large and exceed the phonon anomalies at the structural and SDW phase transitions in the iron pnictides, suggesting a strong spin-phonon coupling in the Se-doped iron chalcogenides induced by the short-range incommensurate spin-fluctuations. The magnitude of the phonon anomalies in these materials was found to increase for increasing Se-doping and decreasing concentrations of iron excess. At the moment it is not decided, if the phonon anomalies at T_{IC} are intrinsic or induced by the Fe excess. More measurements on iron chalcogenide samples with different concentrations of iron excess and Se-doping are necessary to study these effects in detail.

Appendix A

Details on DILOR XY triple grating spectrometer

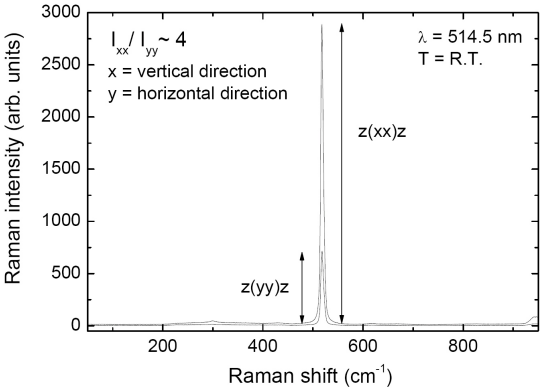

Figure A.1: Raman spectra of silicon-(100) at room temperature in z(xx)z and z(yy)z polarization configurations for 514.5 nm laser excitation.

1. The triple grating spectrometer acts as an analyzer with the pass direction along the vertical direction. This polarizing property is due to the orientation of the spectrometer gratings. In order to yield highest Raman intensity, the scattered light has to enter the spectrometer in vertical direction. For illustration, figure A.1 shows the Raman

spectra of silicon-(100) for the z(xx)z and z(yy)z polarization configurations. Due to crystal symmetry between a- and b-axis, the intensity of the mode at 518 cm^{-1} has to be equal for both cases. However, z(xx)z yields a ~ 4 times higher intensity compared to z(yy)z.

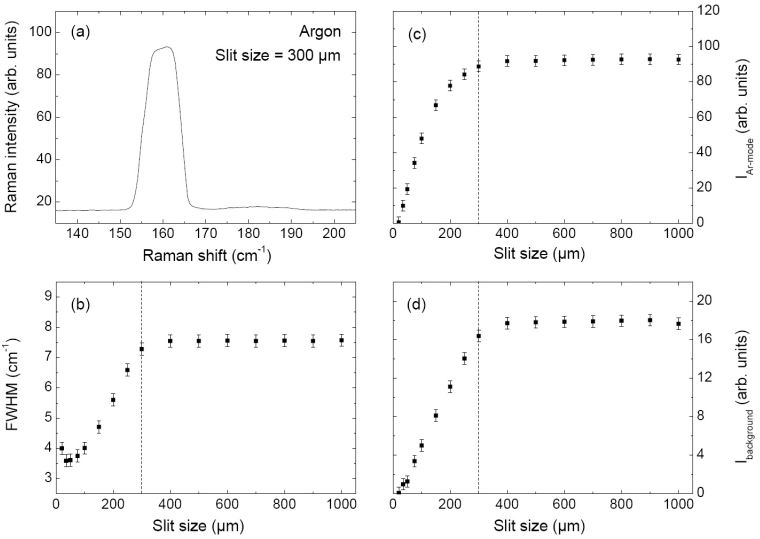

Figure A.2: (a) Raman spectrum of an argon calibration lamp with focus on a discrete line for slit sizes $S_1 = S_3 = 300$ μm; (b) FWHM of the argon line in (a), (c) intensity of the argon line in (a), and (d) background intensity of the Raman spectrum in (a) each as a function of the slit size. (The argon line was fitted to a pure Gaussian profile with linear background. The deviation from the linewidth decrease at very low slit sizes has to be attributed to a non-perfect alignment of the spectrometer gratings.)

2. In general, in the triple grating spectrometer, the size of the slits S_1 and S_3 determines the resolution of the spectrometer. In order to give an example, an argon calibration lamp was positioned in the focus of the entrance lens (in front of slit S_1) of the spectrometer. Due to the very sharp intrinsic linewidths of the argon lines, the experimentally determined linewidths are a measure of the Gaussian broadening due to the spectrometer resolution. Figure A.2 shows the FWHM and intensity of an argon line together with the intensity of the corresponding background as a function of the slit size $S_1 = S_3$.

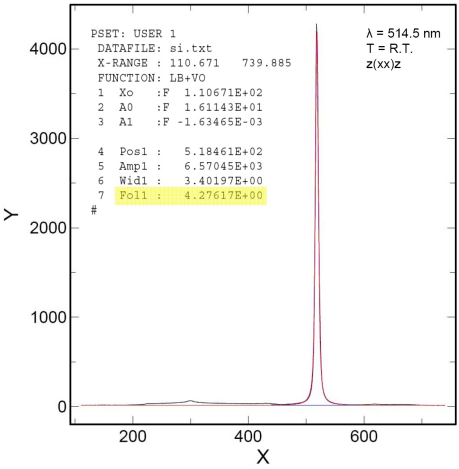

Figure A.3: Raman spectrum of Si-(100) for slit sizes $S_1 = S_3 = 300$ μm at room temperature. The optical mode at 518 cm^{-1} is fitted to a Voigt profile (X = Raman shift (cm^{-1}), Y = Raman intensity (arb. units). FOL1 indicates the Gaussian folding width due to the spectrometer resolution.)

Closing the slits increases the instrumental resolution with intensity loss. For a slit size of ~ 300 μm the Raman intensity starts to saturate, indicating that the slit diameter S_1 approximately covers the focussed incoming argon light. Note that the exact resolution of the spectrometer can only be obtained by a point source in the focus. Due to the large extension of the argon lamp compared to the size of the laser beam on the sample surface during Raman scattering, the argon lines cannot yield the correct precise linewidth broadening.

In order to give a better reference for the instrumental resolution during Raman scattering, a silicon single crystal was used. Since silicon modes exhibit symmetric Lorentzian lineshapes with small linewidths, fitting these modes to Voigt profiles yields a characteristic value for the Gaussian broadening due to the spectrometer resolution. Figure A.3 shows a Voigt fit of a silicon mode at room temperature (same as in figure A.1) with slit sizes $S_1 = S_3 = 300$ μm. The fit yields an instrumental resolution of ~ 4 cm^{-1} (FWHM).

Appendix B

SEM images of the slightly underdoped LCCO film

Figures B.1–B.4 show a collection of SEM images of the slightly underdoped LCCO film with focus on the grain boundary. Figure B.1 gives a large-scale overview of the film around the grain boundary, while figure B.2 focusses microscopically on the grain boundary area. The line structures are perfectly aligned along the in-plane crystal axes, imaging the symmetric tilt angle between the crystal axes on both sides of the grain boundary. The SEM images show no indication for a crossing of the line structures over the grain boundary. Furthermore, the spatial distribution of the line structures and particles is not changed at the grain boundary. Reflecting this result, the Raman spectrum at the grain boundary is not changed compared to the Raman spectrum away from the grain boundary. This indicates that the crystal structure of LCCO films stays "homogeneous" up to very close distances to the grain boundary. The partly etched area in figure B.1 shows a part of the LCCO film, which was etched a second time during the procedure of optical lithography. Similar partly etched areas are shown in figures B.3 and B.4. The corresponding etching edges represent vertical cuts, showing that the particles and line structures reach deeply into the LCCO matrix. On the lower and left part of figures B.3 and B.4 the film is etched completely down to the $SrTiO_2$ substrate. The round structures in the $SrTiO_2$ substrate reflect dips, which are probably due to knock outs of the particles during etching, leaving dips in the film, which are transmitted to the $SrTiO_3$ substrate by further etching.

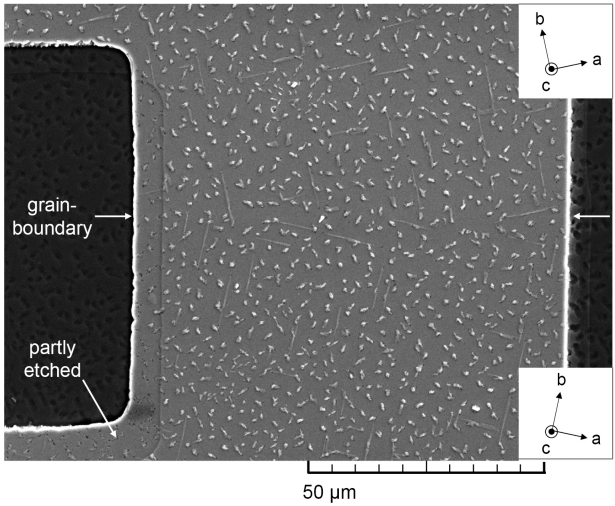

Figure B.1

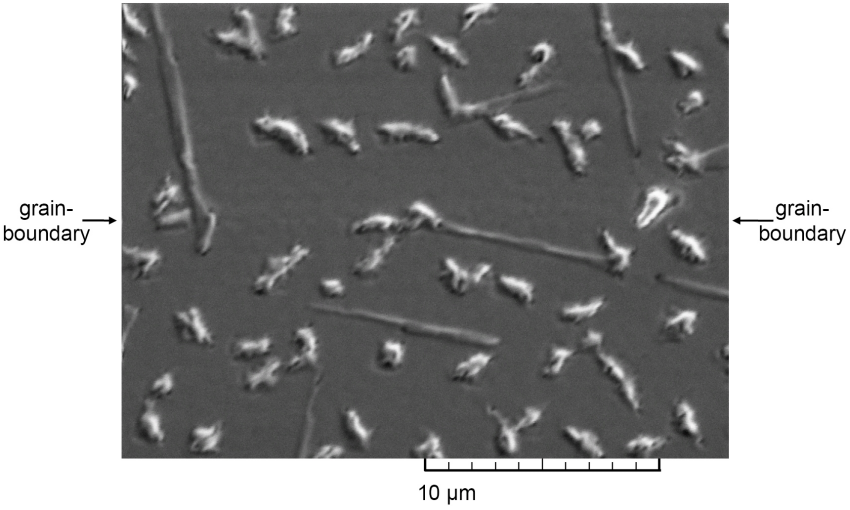

Figure B.2

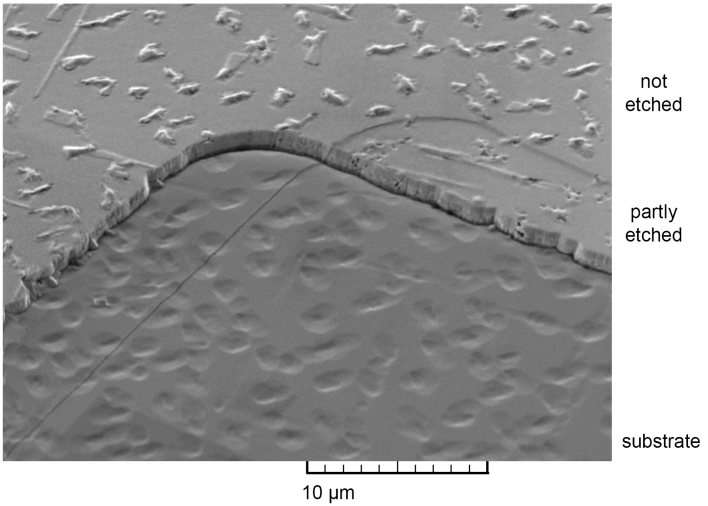

Figure B.3

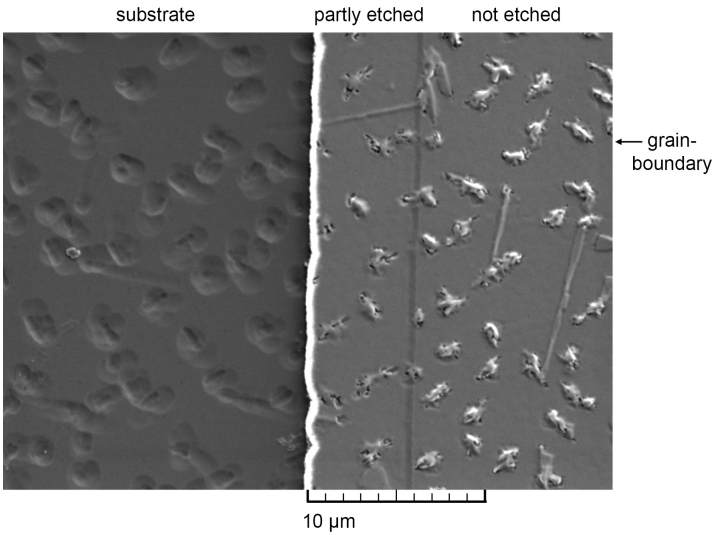

Figure B.4

Appendix C

Surface anomalies at $\sim$ 180 K in iron pnictides

Finally, an interesting observation, which was noticed similarly in nearly all of the studied ternary iron arsenide samples for (xu) polarization configurations at approximately the same temperature, should be mentioned. Figure C.1 shows optical images of the plane surface of the underdoped SKFA ($x \sim 0.15$) sample taken after Raman light scattering for blocked incident laser beam together with corresponding Raman spectra of z(xu)z polarization configuration for different temperatures. Between the taking of the optical images and the Raman measurements there was a delay time of $\sim$ 5 minutes. For increasing temperature a small bright speck appears at $\sim$ 160 K close to the point, where the incident laser beam was focussed on the sample surface. The bright speck becomes larger at higher temperatures. Above $\sim$ 180 K it disappears totally without any residual on the sample surface. Concomitantly, an additional Raman mode at $\sim$ 243 cm^{-1} develops between $\sim$ 160 K and $\sim$ 180 K that is not observed at 200 K and higher temperatures. In optimally doped BKFA ($x \sim 0.32$) (G41), the corresponding additional mode is observed at $\sim$ 226 cm^{-1}, developing at $\sim$ 160 K and disappearing at $\sim$ 200 K. The strong decrease of the B_{1g} mode amplitude in optimally doped BKFA ($x \sim 0.32$) coincides with this temperature interval (Fig. 5.25). On the other hand, in the underdoped SKFA ($x \sim 0.15$) sample the integrated intensity recovers at $\sim$ 200 K after a similar intensity decrease in the same temperature range (Fig. C.2).

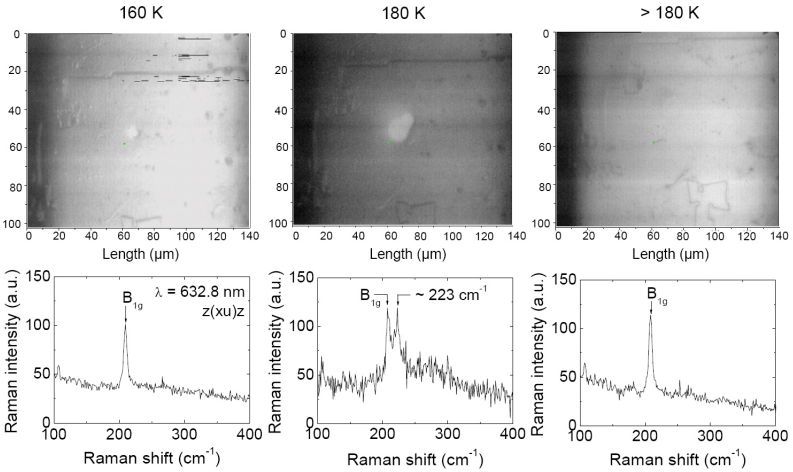

Figure C.1: (*top)* Optical images of the plane surface of the underdoped SKFA ($x \sim 0.15$) (G15) sample taken after Raman light scattering for blocked incident laser beam (the bright specks are close to the points, where the laser beam was focussed on the sample surface) and (*bottom)* corresponding Raman spectra in z(xu)z polarization configuration for different temperatures each for approximately the same measuring position.

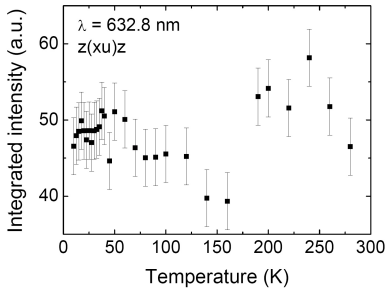

Figure C.2: Temperature dependence of the integrated intensity of the B_{1g} mode in underdoped SKFA ($x \sim 0.15$) (G15).

Because of its total reversibility, the bright speck on the sample surface cannot be explained by surface damaging due to the laser beam. Moreover, the observation of similar effects in the different samples in a comparable temperature range points to an intrinsic physical origin. The different intensities of the bright speck at different temperatures suggest a luminescence effect, where the active electronic band is continuously shifted with the thermal expansion of the crystal for heating. The possibility of luminescence-induced intensity anomalies at $T \sim 180$ K has to be kept in mind, when the temperature dependence of optical modes is studied.

Bibliography

[Alf03] L. Alff, Y. Krockenberger, B. Welter, M. Schonecke, R. Gross, D. Manske, and M. Naito. Nature **422**, 698 (**2003**).

[All72] P. B. Allen. Phys. Rev. B **6**, 2577 (**1972**).

[Alv96] A. D. Alvarenga, D. Rao, J. A. Sanjurjo, E. Granado, I. Torriani, and C. Rettori. Phys. Rev. B **53**, 837 (**1996**).

[And87] P. W. Anderson. Science **235**, 1196 (**1987**).

[Arm01] N. P. Armitage, D. H. Lu, C. Kim, A. Damascelli, K. M. Shen, F. Ronning, D. L. Feng, P. Bogdanov, Z.-X. Shen, Y. Onose, Y. Taguchi, Y. Tokura, P. K. Mang, N. Kaneko, and M. Greven. Phys. Rev. Lett. **87**, 147003 (**2001**).

[Arm09] N. P. Armitage, P. Fournier, and R. L. Greene. arXiv:0906.2931 (**2009**).

[Bak09] M. Bakr, A. P. Schnyder, L. Klam, D. Manske, C. T. Lin, B. Keimer, M. Cardona, and C. Ulrich. Phys. Rev. B **80**, 064505 (**2009**).

[Bao09] W. Bao, Y. Qiu, Q. Huang, M. A. Green, P. Zajdel, M. R. Fitzsimmons, M. Zhernenkov, S. Chang, M. Fang, B. Qian, E. K. Vehstedt, J. Yang, H. M. Pham, L. Spinu, and Z. Q. Mao. Phys. Rev. Lett. **102**, 247001 (**2009**).

[Bar57] J. Bardeen, L. N. Cooper, and J. R. Schriefer. Phys. Rev. **108**, 1175 (**1957**).

[Bed86] J. G. Bednorz and K. A. Müller. Cond. Mat. **64**, 189 (**1986**).

[Blu02] G. Blumberg, A. Koitzsch, A. Gozar, B. S. Dennis, C. S. Kendziora, P. Fournier, and R. L. Green. Phys. Rev. Lett. **88**, 107002 (**2002**).

[Boe] L. Boeri. *private communications.*

[Boe08] L. Boeri, O. V. Dolgov, and A. A. Golubov. Phys. Rev. Lett. **101**, 026403 (**2008**).

[Boe09] L. Boeri, O. V. Dolgov, and A. A. Golubov. Physica C **469**, 628 (**2009**).

[Boe10] L. Boeri, M. Calandra, I. I. Mazin, O. V. Dolgov, and F. Mauri. Phys. Rev. B **82**, 020506(R) (**2010**).

[Bro10] P. J. Brown, T. Chatterji, A. Stunault, Y. Su, Y. Xiao, R. Mittal, T. Brückel, T. Wolf, and P. Adelmann. Phys. Rev. B **82**, 024421 (**2010**).

[Buc04] W. Buckel and R. Kleiner. *Supraleitung.* Wiley-VCH (**2004**).

[Car82] M. Cardona (ed.). *Light Scattering in Solids II, Topics Appl. Phys., Vol 50.* Springer (**1982**).

[Car83] M. Cardona (ed.). *Light Scattering in Solids I, Topics Appl. Phys., Vol. 8.* Springer, Berlin Heidelberg (**1983**).

[Car00] M. Cardona. *in Raman Scattering in Materials Science.* ed. by W. H. Weber and R. Merlin, Springer, Berlin, p. 151 (**2000**).

[Cha09] L. Chauvière, Y. Gallais, M. Cazayous, A. Sacuto, M. A. Mèasson, D. Colson, and A. Forget. Phys. Rev. B **80**, 094504 (**2009**).

[Cha10] L. Chauvière, Y. Gallais, M. Cazayous, M. A. Méasson, A. Sacuto, D. Colson, and A. Forget. arXiv: 1007.0720 (**2010**).

[Che03] B. Chesca, K. Ehrhardt, M. Mößle, R. Straub, D. Koelle, R. Kleiner, and A. Tsukada. Phys. Rev. Lett. **90**, 057004 (**2003**).

[Che08] G. F. Chen, Z. Li, G. Li, W.-Z. Hu, J. Dong, J. Zhou, X.-D. Zhang, P. Zheng, N.-L. Wang, and J.-L. Luo. Chin. Phys. Lett. **25**, 3403 (**2008**).

[Che09a] C. Chen, L. He, L. Lai, H. Zhang, J. Lu, L. Guo, and Y. Li. J. Phys.: Condens. Matter **21**, 145 601 (**2009**).

[Che09b] G. F. Chen, Z. G. Chen, J. Dong, W. Z. Hu, G. Li, X. D. Zhang, P. Zheng, J. L. Luo, and N. L. Wang. Phys. Rev. B **79**, 140 509(R) (**2009**).

[Che09c] H. Chen, Y. Ren, Y. Qiu, W. Bao, R. H. Liu, G. Wu, T. Wu, Y. L. Xie, X. F. Wang, Q. Huang, and X. H. Chen. Europhys. Lett. **85**, 17 006 (**2009**).

[Cho08] K.-Y. Choi, D. Wulferding, P. Lemmens, N. Ni, S. L. Bud'ko, and P. C. Canfield. Phys. Rev. B **78**, 212 503 (**2008**).

[Cho10] K.-Y. Choi, P. Lemmens, I. Eremin, G. Zwicknagl, H. Berger, G. L. Sun, D. L. Sun, and C. T. Lin. J. Phys.: Condens. Matter **22**, 115 802 (**2010**).

[Chr08] A. D. Christianson, E. A. Goremychkin, R. Osborn, S. Rosenkranz, M. D. Lumsden, C. D. Malliakas, I. S. Todorov, H. Claus, D. Y. Chung, M. G. Kanatzidis, R. I. Bewley, and T. Guidi. Nature **456**, 930 (**2008**).

[Chu09] J.-H. Chu, J. G. Analytis, C. Kucharczyk, and I. R. Fisher. Phys. Rev. B **79**, 014 506 (**2009**).

[Cow68] R. A. Cowley. Rep. Prog. Phys. **31**, 123 (**1968**).

[Cro72] H. M. Crosswhite and G. H. Dieke. *American Institute of Physics Handbook*. ed. by D. E. Gray, McGraw-Hill Book Company, p. 7e-29 (**1972**).

[Dag05] Y. Dagan, M. M. Qazilbash, and R. L. Greene. Phys. Rev. Lett. **94**, 187 003 (**2005**).

[Dag07] Y. Dagan, R. Beck, and R. L. Greene. Phys. Rev. Lett. **99**, 147 004 (**2007**).

[Dem08] W. Demtröder. *Experimentalphysik 1: Mechanik und Wärme*. Spektrum, Berlin (**2008**).

[Dev94] T. P. Devereaux. Phys. Rev. B **50**, 10 287 (**1994**).

[Dev07] T. P. Devereaux and R. Hackl. Rev. Mod. Phys. **79**, 175 (**2007**).

[Dil] Dilor. *User Manual - XY Modular Laser Raman Spectrometer.*

[Din08] H. Ding, P. Richard, K. Nakayama, K. Sugawara, T. Arakane, Y. Sekiba, A. Takayama, S. Souma, T. Sato, T. Takahashi, Z. Wang, X. Dai, Z. Fang, G. F. Chen, J. L. Luo, and N. L. Wang. Europhys. Lett. **83**, 47001 (**2008**).

[dlC08] C. de la Cruz, Q. Huang, J. W. Lynn, J. Li, W. Ratcliff, J. L. Zarestky, H. A. Mook, G. F. Chen, J. L. Luo, N. L. Wang, and P. Dai. Nature **453**, 899 (**2008**).

[Don08] J. Dong, H. J. Zhang, G. Xu, Z. Li, G. Li, W. Z. Hu, D. Wu, G. F. Chen, X. Dai, J. L. Luo, Z. Fang, and N. L. Wang. Europhys. Lett. **83**, 27006 (**2008**).

[Dre08] M. Dressel. *Lecture Notes* (**2008**).

[Ein96] D. Einzel and R. Hackl. J. Raman Spectrs. **27**, 307 (**1996**).

[Evt09] D. V. Evtushinsky, D. S. Inosov, V. B. Zabolotnyy, A. Koitzsch, M. Knupfer, B. Büchner, M. S. Viazovska, G. L. Sun, V. Hinkov, A. V. Boris, C. T. Lin, B. Keimer, A. Varykhalov, A. A. Kordyuk, and S. V. Borisenko. Phys. Rev. B **79**, 054517 (**2009**).

[Fan61] U. Fano. Phys. Rev. **124**, 1866 (**1961**).

[Fan08] M. H. Fang, H. M. Pham, B. Qian, T. J. Liu, E. K. Vehstedt, Y. Liu, L. Spinu, and Z. Q. Mao. Phys. Rev. B **78**, 224503 (**2008**).

[Fuk08] T. Fukuda, A. Q. R. Baron, S.-I. Shamoto, M. Ishikado, H. Nakamura, M. Machida, H. Uchiyama, S. Tsutsui, A. Iyo, H. Kito, J. Mizuki, M. Arai, H. Eisaki, and H. Hosono. J. Phys. Soc. Jpn. **77**, 103715 (**2008**).

[Gra99] E. Granado, A. García, J. A. Sanjurjo, C. Rettori, I. Torriani, F. Prado, R. D. Sánchez, A. Caneiro, and S. B. Oseroff. Phys. Rev. B **60**, 11879 (**1999**).

[Gre01] T. Greibe. *MBE growth of superconducting thin films.* Technical report, NTT Basic Research Laboratories (**2001**).

[Gre09] N. C. Gresty, Y. Takabayashi, A. Y. Ganin, M. T. McDonald, J. B. Claridge, D. Giap, Y. Mizuguchi, Y. Takano, T. Kagayama, Y. Ohishi, M. Takata, M. J. Rosseinsky, S. Margadonna, and K. Prassides. J. Am. Chem. Soc. **131**, 16 944 (**2009**).

[Hac89] R. Hackl, P. Müller, D. Einzel, and W. Gläser. Physica C **162-164**, 1241 (**1989**).

[Had89] V. G. Hadjiev, I. Z. Kostadinov, L. Bozukov, E. Dinolova, and D. M. Mateev. Solid State Commun. **71**, 1093 (**1989**).

[Had98] V. G. Hadjiev, X. Zhou, T. Strohm, and M. Cardona. Phys. Rev. B **58**, 1043 (**1998**).

[Had99] V. G. Hadjiev, A. A. Martin, T. Ruf, and M. Cardona. Phys. stat. sol. (b) **215**, 483 (**1999**).

[Hay78] W. Hayes and R. Loudon. *Scattering of Light by Crystals.* Wiley, New York (**1978**).

[Hei73] A. Heidemann and H. Wettengel. Z. Phys. **258**, 429 (**1973**).

[Hel84] K.-H. Hellwege and A. M. Hellwege (eds.). *Landolt-Börnstein III/18.* Springer, p. 63 (**1984**).

[Hey91] E. T. Heyen, R. Liu, M. Cardona, S. Piñol, R. J. Melville, D. McK. Paul, E. Morán, and M. A. Alario-Franco. Phys. Rev. B **43**, 2857 (**1991**).

[Hor] Horiba - Jobin Yvon. *T64000 User's Training Course.*

[Hos08] H. Hosono. J. Phys. Soc. Jpn. **77**, Suppl. C, 1 (**2008**).

[Hsu08] F.-C. Hsu, J.-Y. Luo, K.-W. Yeh, T.-K. Chen, T.-W. Huang, P. M. Wu, Y.-C. Lee, Y.-L. Huang, Y.-Y. Chu, D.-C. Yan, and M.-K. Wu. Proc. Natl. Acad. Sci. U.S.A. **105**, 14 262 (**2008**).

[Hu08] W. Z. Hu, J. Dong, G. Li, Z. Li, P. Zheng, G. F. Chen, J. L. Luo, and N. L. Wang. Phys. Rev. Lett. **101**, 257 005 (**2008**).

[Hua63] K. Huang. Z. Phys. **171**, 213 (**1963**).

[Hua08] Q. Huang, Y. Qiu, W. Bao, M. A. Green, J. W. Lynn, J. C. Gasparovic, T. Wu, G. Wu, and X. H. Chen. Phys. Rev. Lett. **101**, 257 003 (**2008**).

[Ino09] D. S. Inosov, A. Leineweber, X. Yang, J. T. Park, N. B. Christensen, R. Dinnebier, G. L. Sun, C. Niedermayer, D. Haug, P. W. Stephens, J. Stahn, O. Khvostikova, C. T. Lin, O. K. Andersen, B. Keimer, and V. Hinkov. Phys. Rev. B **79**, 224 503 (**2009**).

[Jay89] A. Jayaraman. *C.V. Raman.* Affiliated East-West Press, Madras (**1989**).

[Jee08] H. S. Jeevan, Z. Hossain, D. Kasinathan, H. Rosner, C. Geibel, and P. Gegenwart. Phys. Rev. B **78**, 092 406 (**2008**).

[Jia09] S. Jiang, H. Xing, G. Xuan, C. Wang, Z. Ren, C. Feng, J. Dai, Z. Xu, and G. Cao. J. Phys.: Condens. Matter **21**, 382 203 (**2009**).

[Kam08] Y. Kamihara, T. Watanabe, M. Hirano, and H. Hosono. J. Am. Chem. Soc. **130**, 3296 (**2008**).

[Kha09] R. Khasanov, M. Bendele, A. Amato, P. Babkevich, A. T. Boothroyd, A. Cervellino, K. Conder, S. N. Gvasaliya, H. Keller, H.-H. Klauss, H. Luetkens, V. Pomjakushin, E. Pomjakushina, and B. Roessli. Phys. Rev. B **80**, 140 511(R) (**2009**).

[Kir96] J. R. Kirtley and C. C. Tsuei. Spektrum der Wissenschaft, **Oktober**, 86 (**1996**).

[Kle66] P. G. Klemens. Phys. Rev. **148**, 845 (**1966**).

[Kle83] M. V. Klein. *in Light Scattering in Solids I, Topics Appl. Phys., Vol. 8.* ed. by M. Cardona, Springer, Berlin Heidelberg (**1983**).

[Kle84] M. V. Klein and S. B. Dierker. Phys. Rev. B **29**, 4976 (**1984**).

[Koe04] D. Koelle. *lecture notes* (**2004**).

[Kre08] C. Krellner, N. Caroca-Canales, A. Jesche, H. Rosner, A. Ormeci, and C. Geibel. Phys. Rev. B **78**, 100 504(R) (**2008**).

[Kro08] Y. Krockenberger, J. Kurian, A. Winkler, A. Tsukada, M. Naito, and L. Alff. Phys. Rev. B **77**, 060 505(R) (**2008**).

[Lav06] J. Laverdiére, S. Jandl, A. A. Mukhin, V. Y. Ivanov, V. G. Ivanov, and M. N. Iliev. Phys. Rev. B **73**, 214 301 (**2006**).

[Lee10] Y. Lee, D. Vaknin, H. Li, W. Tian, J. L. Zarestky, N. Ni, S. L. Bud'ko, P. C. Canfield, R. J. McQueeney, and B. N. Harmon. Phys. Rev. B **81**, 060 406(R) (**2010**).

[Les09] C. Lester, J.-H. Chu, J. G. Analytis, S. C. Capelli, A. S. Erickson, C. L. Condron, M. F. Toney, I. R. Fisher, and S. M. Hayden. Phys. Rev. B **79**, 144 523 (**2009**).

[LeT06] M. LeTacon, A. Sacuto, A. Georges, G. Kotliar, Y. Gallais, D. Colson, and A. Forget. Nature **2**, 537 (**2006**).

[Li09] S. Li, C. de la Cruz, Q. Huang, Y. Chen, J. W. Lynn, J. Hu, Y.-L. Huang, F.-C. Hsu, K.-K. Yeh, M.-K. Wu, and P. Dai. Phys. Rev. B **79**, 054 503 (**2009**).

[Lit08] A. P. Litvinchuk, V. G. Hadjiev, M. N. Iliev, B. Lv, A. M. Guloy, and C. W. Chu. Phys. Rev. B **78**, 060 503(R) (**2008**).

[Liu] Y. Liu. *private communications.*

[Liu09] T. J. Liu, X. Ke, B. Qian, J. Hu, D. Fobes, E. K. Vehstedt, H. Pham, J. H. Yang, M. H. Fang, L. Spinu, P. Schiffer, Y. Liu, and Z. Q. Mao. Phys. Rev. B **80**, 174 509 (**2009**).

[Liu10] C. Liu, T. Kondo, R. M. Fernandes, A. D. Palczewski, E. D. Mun, N. Ni, A. N. Thaler, A. Bostwick, E. Rotenberg, J. Schmalian, S. L. Bud'ko, P. C. Canfield, and A. Kaminski. Nature Phys. **6**, 419 (**2010**).

[Lue] H. Luetkens. *private communications.*

[Lue09] H. Luetkens, H.-H. Klauss, M. Kraken, F. J. Litterst, T. Dellmann, R. Klingeler, C. Hess, R. Khasanov, A. Amato, C. Baines, M. Kosmala, O. J. Schumann, M. Braden, J. Hamann-Borrero, N. Leps, A. Kondrat, G. Behr, J. Werner, and B. Büchner. Nature Materials **8**, 305 (**2009**).

[Lyn09] J. W. Lynn and P. Dai. Physica C **469**, 469 (**2009**).

[Man] D. Manske. *private communications.*

[Man04] P. K. Mang, S. Larochelle, A. Mehta, O. P. Vajk, A. S. Erickson, L. Lu, W. J. L. Buyers, A. F. Marshall, K. Prokes, and M. Greven. Phys. Rev. B **70**, 094 507 (**2004**).

[Mar62] A. A. Maradudin, A. E. Fein, and G. H. Vineyard. Phys. stat. sol. **2**, 1479 (**1962**).

[Mar71] A. A. Maradudin and R. F. Wallis. Phys. Rev. B **3**, 2063 (**1971**).

[Mar08] S. Margadonna, Y. Takabayashi, M. T. McDonald, K. Kasperkiewicz, Y. Mizuguchi, Y. Takano, A. N. Fitch, E. Suarde, and K. Prassides. Chem. Commun. 5607 (**2008**).

[Mat05] H. Matsui, K. Terashima, T. Sato, T. Takahashi, M. Fujita, and K. Yamada. Phys. Rev. Lett. **95**, 017 003 (**2005**).

[Mat07] H. Matsui, T. Takahashi, T. Sato, K. Terashima, H. Ding, T. Uefuji, and K. Yamada. Phys. Rev. B **75**, 224 514 (**2007**).

[Maz09] I. I. Mazin and J. Schmalian. Physica C **469**, 614 (**2009**).

[McQ09] T. M. McQueen, Q. Huang, V. Ksenofontov, C. Felser, Q. Xu, H. Zandbergen, Y. S. Hor, J. Allred, A. J. Williams, D. Qu, J. Checkelsky, N. P. Ong, and R. J. Cava. Phys. Rev. B **79**, 014 522 (**2009**).

[Men84] J. Menéndez and M. Cardona. Phys. Rev. B **29**, 2051 (**1984**).

[Mer00] R. Merlin, A. Pinczuk, and W. H. Weber. *in Raman Scattering in Materials Science*. ed. by W. H. Weber and R. Merlin, Springer, Berlin, p. 1 (**2000**).

[Mis99] O. V. Misochko, E. Y. Sherman, N. Umesaki, K. Sakai, and S. Nakashima. Phys. Rev. B **59**, 11 495 (**1999**).

[Mit08] R. Mittal, Y. Su, S. Rols, T. Chatterji, S. L. Chaplot, H. Schober, M. Rotter, D. Johrendt, and T. Brueckel. Phys. Rev. B **78**, 104 514 (**2008**).

[Mit09] R. Mittal, L. Pintschovius, D. Lamago, R. Heid, K.-P. Bohnen, D. Reznik, S. L. Chaplot, Y. Su, N. Kumar, S. K. Dhar, A. Thamizhavel, and T. Brueckel. Phys. Rev. Lett. **102**, 217 001 (**2009**).

[Miz08] Y. Mizuguchi, F. Tomioka, S. Tsuda, T. Yamaguchi, and Y. Takano. Appl. Phys. Lett. **93**, 152 505 (**2008**).

[Mül06] M. Müller (Rahlenbeck). *Transportmessungen an Korngrenz-Josephson-Kontakten zur Untersuchung der Ordnungsparametersymmetrie im elektronendotierten Kupratsupraleiter* $La_{2-x}Ce_xCuO_4$. diploma thesis, Tübingen University (**2006**).

[Mon90] H. Monien and A. Zawadowski. Phys. Rev. B **41**, 8798 (**1990**).

[Mus09] B. Muschler, W. Prestel, R. Hackl, T. P. Devereaux, J. G. Analytis, J.-H. Chu, and I. R. Fisher. Phys. Rev. B **80**, 180510(R) (**2009**).

[Nag01] J. Nagamatsu, N. Nakagawa, T. Muranaka, Y. Zenitani, and J. Akimitsu. Nature **410**, 63 (**2001**).

[Nai00] M. Naito and M. Hepp. Jpn. J. Appl. Phys. **39**, L485 (**2000**).

[Nai02] M. Naito, A. Tsukada, T. Greibe, and H. Sato. Proc. SPIE **4811**, 140 (**2002**).

[Ni08] N. Ni, S. Nandi, A. Kreyssig, A. I. Goldman, E. D. Mun, S. L. Bud'ko, and P. C. Canfield. Phys. Rev. B **78**, 014523 (**2008**).

[Nic93] E. J. Nicol, C. Jiang, and J. P. Carbotte. Phys. Rev. B **47**, 8131 (**1993**).

[Nor05] M. R. Norman, D. Pines, and C. Kallin. Adv. Phys. **54**, 715 (**2005**).

[Onn11] H. K. Onnes. Comm. Leiden **120b** (**1911**).

[Ono01] Y. Onose, Y. Taguchi, K. Ishizaka, and Y. Tokura. Phys. Rev. Lett. **87**, 217001 (**2001**).

[Par] J.-T. Park. *private communications.*

[Par09] J. T. Park, D. S. Inosov, C. Niedermayer, G. L. Sun, D. Haug, N. B. Christensen, R. Dinnebier, A. V. Boris, A. J. Drew, L. Schulz, T. Shapoval, U. Wolff, V. Neu, X. Yang, C. T. Lin, B. Keimer, and V. Hinkov. Phys. Rev. Lett. **102**, 117006 (**2009**).

[Pet72] Y. Petroff, P. Y. Yu, and Y. R. Shen. Phys. Rev. Lett. **29**, 1558 (**1972**).

[Pet74] Y. Petroff. J. Phys. (Paris) Colloq. C3 **35**, 277 (**1974**).

[Pet75] Y. Petroff, P. Y. Yu, and Y. R. Shen. Phys. Rev. B **12**, 2488 (**1975**).

[Pin66] D. Pines and P. Nozieres. *The theory of Quantum Liquids.* W. A. Benjamin, New York (**1966**).

[Pin71] A. S. Pine and G. Dresselhaus. Phys. Rev. B **4**, 356 (**1971**).

[Pin72] A. S. Pine and G. Dresselhaus. Phys. Rev. B **5**, 4087 (**1972**).

[Pin83] A. Pinczuk and E. Burstein. *in Light Scattering in Solids I, Topics Appl. Phys., Vol. 8.* ed. by M. Cardona, Springer, Berlin Heidelberg, p. 23 (**1983**).

[Pom09] E. Pomjakushina, K. Conder, V. Pomjakushin, M. Bendele, and R. Khasanov. Phys. Rev. B **80**, 024517 (**2009**).

[Qaz05] M. M. Qazilbash, A. Koitzsch, B. S. Dennis, A. Gozar, H. Balci, C. A. Kendziora, R. L. Greene, and G. Blumberg. Phys. Rev. B **72**, 214510 (**2005**).

[Rez91] D. Reznik, A. Kotz, S. L. Cooper, M. V. Klein, W. C. Lee, and D. M. Ginsberg. Physica C **185-189**, 1029 (**1991**).

[Rez09] D. Reznik, K. Lokshin, D. C. Mitchell, D. Parshall, W. Dmowski, D. Lamago, R. Heid, K.-P. Bohnen, A. S. Sefat, M. A. McGuire, B. C. Sales, D. G. Mandrus, A. Subedi, D. J. Singh, A. Alatas, M. H. Upton, A. H. Said, A. Cunsolo, Y. Shvyd'ko, and T. Egami. Phys. Rev. B **80**, 214534 (**2009**).

[RM91] J. Rossat-Mignod, L. P. Regnault, C. Vettier, P. Bourges, P. Burlet, J. Bossy, J. Y. Henry, and G. Lapertot. Physica C **185**, 86 (**1991**).

[Rob09] G. Roberge, S. Charpentier, S. Godin-Proulx, P. Rauwel, K. D. Truong, and P. Fournier. J. Cryst. Growth **311**, 1340 (**2009**).

[Rot08a] M. Rotter, M. Pangerl, M. Tegel, and D. Johrendt. Angew. Chem. Int. Ed. **47**, 7949 (**2008**).

[Rot08b] M. Rotter, M. Tegel, and D. Johrendt. Phys. Rev. Lett. **101**, 107006 (**2008**).

[Rot08c] M. Rotter, M. Tegel, D. Johrendt, I. Schellenberg, W. Hermes, and R. Pöttgen. Phys. Rev. B **78**, 020503(R) (**2008**).

[Rou81] D. L. Rousseau, R. P. Baumann, and S. P. S. Porto. J. Raman Spectr. **10**, 253 (**1981**).

[Roz81] S. Rozsa and H. U. Schuster. Z. Naturforsch. B: Chem. Sci. **36**, 1668 (**1981**).

[Sal09] B. C. Sales, A. S. Sefat, M. A. McGuire, R. Y. Jin, D. Mandrus, and Y. Mozharivskyj. Phys. Rev. B **79**, 094521 (**2009**).

[Saw02] A. Sawa, M. Kawasaki, H. Takagi, and Y. Tokura. Phys. Rev. B **66**, 014531 (**2002**).

[Saw08] A. Sawa, M. Kawasaki, H. Takagi, and Y. Tokura. Phys. Rev. Lett. **101**, 107007 (**2008**).

[Sca95] D. J. Scalapino. Phys. Rep. **250**, 329 (**1995**).

[Sch69] H. L. Schlafer and G. Gliemann. *Basic principles of ligand field theory.* Wiley, New York (**1969**).

[Sef08] A. S. Sefat, R. Jin, M. A. McGuire, B. C. Sales, D. J. Singh, and D. Mandrus. Phys. Rev. Lett. **101**, 117004 (**2008**).

[Sta90] T. Staufer, R. Hackl, and P. Müller. Solid State Commun. **75**, 975 (**1990**).

[Sub08] A. Subedi, L. Zhang, D. J. Singh, and M. H. Du. Phys. Rev. B **78**, 134514 (**2008**).

[Sug89] S. Sugai, T. Kobayashi, and J. Akimitsu. Phys. Rev. B **40**, 2686 (**1989**).

[Sun] D. L. Sun. *private communications.*

[Sun09] G. L. Sun, D. L. Sun, M. Konuma, P. Popovich, A. Boris, J. B. Peng, K.-Y. Choi, P. Lemmens, and C. T. Lin. arXiv:0901.2728v2 (**2009**).

[Tak89] H. Takagi, S. Uchida, and Y. Tokura. Phys. Rev. Lett. **62**, 1197 (**1989**).

[Tak08] H. Takahashi, K. Igawa, K. Arii, Y. Kamihara, M. Hirano, and H. Hosono. Nature **453**, 376 (**2008**).

[Tam10] A. Tamai, A. Y. Ganin, E. Rozbicki, J. Bacsa, W. Meevasana, P. D. C. King, M. Caffio, R. Schaub, S. Margadonna, K. Prassides, M. J. Rosseinsky, and F. Baumberger. Phys. Rev. Lett. **104**, 097002 (**2010**).

[Teg08] M. Tegel, M. Rotter, V. Weiß, F. M. Schappacher, R. Pöttgen, and D. Johrendt. J. Phys.: Condens. Matter **20**, 452201 (**2008**).

[Tho91] C. Thomsen. *in Light Scattering in Solids VI, Topics Appl. Phys., Vol. 68.* ed. by M. Cardona and G. Güntherodt, Springer, p. 285 (**1991**).

[Tin96] M. Tinkham. *Introduction to superconductivity.* McGraw-Hill Book Co., New York (**1996**).

[Tok89] Y. Tokura, H. Takagi, and S. Uchida. Nature **337**, 345 (**1989**).

[Tsu00] C. C. Tsuei and J. R. Kirtley. Rev. Mod. Phys. **72**, 969 (**2000**).

[Tsu02] A. Tsukada, T. Greibe, and M. Naito. Phys. Rev. B **66**, 184515 (**2002**).

[Tsu05] A. Tsukada, Y. Krockenberger, M. Noda, H. Yamamoto, D. Manske, L. Alff, and M. Naito. Sol. Stat. Comm. **133**, 427 (**2005**).

[Tsu06] A. Tsukada, H. Yamamoto, and M. Naito. Phys. Rev. B **74**, 174515 (**2006**).

[Ulr] C. Ulrich. *private communications.*

[Vig97] P. Vigoureux, A. Gukasov, S. N. Barilo, and D. Zhigunov. Physica B **234**, 815 (**1997**).

[Wag] M. Wagenknecht. *private communications.*

[Wag08a] M. Wagenknecht. *Korngrenz-Tunnelspektroskopie am elektronendotierten Kupratsupraleiter* $La_{2-x}Ce_xCuO_4$. dissertation, Tübingen University (**2008**).

[Wag08b] M. Wagenknecht, D. Koelle, R. Kleiner, S. Graser, N. Schopohl, B. Chesca, A. Tsukada, S. T. B. Goennenwein, and R. Gross. Phys. Rev. Lett. **100**, 227 001 (**2008**).

[Wan08] C. Wang, L. Li, S. Chi, Z. Zhu, Z. Ren, Y. Li, Y. Wang, X. Lin, Y. Luo, S. Jiang, X. Xu, G. Cao, and Z. Xu. Europhys. Lett. **83**, 67 006 (**2008**).

[Wan09] X. F. Wang, T. Wu, G. Wu, H. Chen, Y. L. Xie, J. J. Ying, Y. J. Yan, R. H. Liu, and X. H. Chen. Phys. Rev. Lett. **102**, 117 005 (**2009**).

[Web10] C. Weber, K. Haule, and G. Kotliar. Nature Physics, DOI: 10.1038/NPHYS1706 (**2010**).

[Wen08] H.-H. Wen, G. Mu, L. Fang, H. Yang, and X. Zhu. Europhys. Lett. **82**, 17 009 (**2008**).

[Wen09] J. Wen, G. Xu, Z. Xu, Z. W. Lin, Q. Li, W. Ratcliff, G. Gu, and J. M. Tranquada. Phys. Rev. B **80**, 104 506 (**2009**).

[Wer82] A. Werner and H. D. Hochheimer. Phys. Rev. B **25**, 5929 (**1982**).

[Wil09] S. D. Wilson, Z. Yamani, C. R. Rotundu, B. Freelon, E. Bourret-Courchesne, and R. J. Birgeneau. Phys. Rev. B **79**, 184 519 (**2009**).

[Wu08] G. Wu, H. Chen, T. Wu, Y. L. Xie, Y. J. Yan, R. H. Liu, X. F. Wang, J. J. Ying, and X. H. Chen. J. Phys.: Condens. Matter **20**, 422 201 (**2008**).

[Wu09a] D. Wu, N. Barišić, N. Drichko, S. Kaiser, A. Faridian, M. Dressel, S. Jiang, Z. Ren, L. J. Li, G. H. Cao, Z. A. Xu, H. S. Jeevan, and P. Gegenwart. Phys. Rev. B **79**, 155 103 (**2009**).

[Wu09b] G. Wu, Y. L. Xie, H. Chen, M. Zhong, R. H. Liu, B. C. Shi, Q. J. Li, X. F. Wang, T. Wu, Y. J. Yan, J. J. Ying, and X. H. Chen. J. Phys.: Condens. Matter **21**, 142 203 (**2009**).

[Wys00] K. I. Wysokiński. *in New Developments in High Temperature Superconductivity.* ed. by J. Klamut, B. W. Veal, B. M. Dabrowski, P. W. Klamut, and and P. Kazimierski, Springer, p. 211 (**2000**).

[Xia09] Y. Xia, D. Qian, L. Wray, D. Hsieh, G. F. Chen, J. L. Luo, N. L. Wang, and M. Z. Hasan. Phys. Rev. Lett. **103**, 037 002 (**2009**).

[Yam94] T. Yamada, K. Kinoshita, and H. Shibata. Jpn. J. Appl. Phys. **33**, L168 (**1994**).

[Yam98] K. Yamada, C. H. Lee, K. Kurahashi, J. Wada, S. Wakimoto, S. Ueki, H. Kimura, Y. Endoh, S. Hosoya, G. Shirane, R. J. Birgeneau, M. Greven, M. A. Kastner, and Y. J. Kim. Phys. Rev. B **57**, 6165 (**1998**).

[Yeh08] K.-W. Yeh, T.-W. Huang, Y.-L. Huang, T.-K. Chen, F.-C. Hsu, P. M. Wu, Y.-C. Lee, Y.-Y. Chu, C.-L. Chen, J.-Y. Luo, D.-C. Yan, and M.-K. Wu. Europhys. Lett. **84**, 37 002 (**2008**).

[Yil09a] T. Yildirim. Physica C **469**, 425 (**2009**).

[Yil09b] T. Yildirim. Phys. Rev. Lett. **102**, 037 003 (**2009**).

[Yu73] P. Y. Yu, Y. R. Shen, and Y. Petroff. Solid State Commun. **12**, 973 (**1973**).

[Yu01] P. Y. Yu and M. Cardona. *Fundamentals of Semiconductors - Physics and Materials Properties*. Springer (**2001**).

[Zab09] V. B. Zabolotnyy, D. S. Inosov, D. V. Evtushinsky, A. Koitzsch, A. A. Kordyuk, G. L. Sun, J. T. Park, D. Haug, V. Hinkov, A. V. Boris, C. T. Lin, M. Knupfer, A. N. Yaresko, B. Büchner, A. Varykhalov, R. Follath, and S. V. Borisenko. Nature **457**, 569 (**2009**).

[Zbi09] M. Zbiri, H. Schober, M. R. Johnson, S. Rols, R. Mittal, Y. Su, M. Rotter, and D. Johrendt. Phys. Rev. B **79**, 064 511 (**2009**).

[Zey] R. Zeyher. *private communications*.

[Zey90] R. Zeyher and G. Zwicknagl. Z. Phys. B: Condens. Matter **78**, 175 (**1990**).

[Zha09] L. Zhang, D. J. Singh, and M. H. Du. Phys. Rev. B **79**, 012 506 (**2009**).

[Zim05] A. Zimmers, J. M. Tomczak, R. P. S. M. Lobo, N. Bontemps, C. P. Hill, M. C. Barr, Y. Dagan, R. L. Greene, A. J. Millis, and C. C. Homes. Europhys. Lett. **70**, 225 (**2005**).

Acknowledgement

This PhD thesis would not have been possible without the help of numerous people, which I would like to thank in the following. It seems impossible to properly express my gratitude to all the people for their various contributions. However, I will give it an honest try. If I have forgotten someone, I deeply apologize.

First, I would like to thank Prof. Dr. Bernhard Keimer for giving me the opportunity to realize my PhD thesis in his group and for supporting me during this time and beyond. In particular, I am grateful for his ever open door and his friendly, competent, and helpful hand. Furthermore, I am grateful for the possibility to participate in several international workshops and for the faith in me when sending me to Japan for a scientific project. Finally, special thanks for his prompt help towards the end of my PhD time, which allowed the smooth conclusion of my thesis.

In the same way, I would like to thank Prof. Dr. Reinhold Kleiner for accepting me as an external PhD student in his group. In particular, I am grateful for his warm-hearted handling and for the good collaboration.

Next, I would like to thank my first direct supervisor, Prof. Dr. Clemens Ulrich, who left the institute after my second year to take a professorship in Australia, for teaching me the experimental technique of Raman light scattering in a very detailed and competent way. Moreover, I am grateful for supporting me and for introducing me to the institute. In the same manner, I would like to thank my second direct supervisor, Dr. Mathieu Le Tacon, for his patience in the discussion of various physical problems and the nice and productive working atmosphere. Furthermore, I am grateful to him for reading the first version of my thesis.

I would like to express special thanks to all of the crystal growers that provided me with nice, high-quality, single crystals and films. First, I would like to thank Dr. Chengtian Lin and his group for the cooperative

and friendly teamwork, especially when samples or characterization data were urgently needed. Particularly, I would like to thank Dr. Dunlu Sun, Dr. Guoli Sun, and Yong Liu for their active help. Likewise, I would like to thank Dr. Akio Tsukada from NTT, Dr. Michael Lambacher and Dr. Andreas Erb from the Walther-Meißner-Institute, and Dr. Alexey Ganin and Prof. Dr. Matthew Rosseinsky from the University of Liverpool.

For many fruitful discussions on theoretical questions, I would like to thank Dr. Lilia Boeri, Dr. Roland Zeyher, and Dr. Dirk Manske. Furthermore, I would like to thank Dr. Vladimir Hinkov, Dr. Alexander Boris, Dr. Dmytro Inosov, and Dr. Philippe Leininger for the open exchange of ideas concerning different experimental techniques. I am grateful for the always pleasant discussion atmosphere. Special thanks to Prof. Dr. Manuel Cardona, who always had an open door for students looking for advice in the field of Raman light scattering. Furthermore, I would like to thank Dr. Olle Gunnarsson for being member of my PhD committee.

I offer many thanks to the Tübingen University for the good collaboration. I always felt warmly welcome when I visited the place of my former studies. At this point, I would like to thank Prof. Dr. Dieter Kölle and Dr. Michael Wagenknecht, as well as many other members of the 'Department of solid state physics', for their active help with sample characterization and transport measurements. I send special thanks to Mrs. Johanna Woye from the Prüfungsamt for her social way in administrative efforts.

My stay at the University of Tokyo in Japan was certainly a highlight of my PhD time. I bow to Prof. Dr. Yoshinori Tokura for his warm welcome and his dedication to offer me a pleasant and informative time. Furthermore, I thank Prof. Dr. Yoshinori Onose, Shinichiro Seki, and all other members of Tokura's department for their scientific support, for integrating me in their group and activities, and for showing me a great time.

It is impossible to properly mention all the people who gave me support with numerous experimental or technical problems during my PhD time. Nonetheless, it's one of my greatest concerns to thank these people as much as possible. First, I would like to thank Armin Schulz for his collaborative and careful assistance during the Raman experiments. Furthermore, I thank Dr. Britta Bohnenbuck for her unresting help during the XRD measurements at low temperature, as well as Dr. Yener Kuru for the high intensity XRD support. Special thanks to Christof Busch for his very active teamwork in the fields of EDX and SEM measurements, as well as to Dr. Mitsuharu Konuma for the argon sputtering support and Ji-Tae Park for the exchange of experience in sample characterization. Thanks to Dr.

Soltan Soltan, Dr. Georg Cristiani, and Dr. Hanns-Ulrich Habermeier for the support with transport characterization and for many inspiring discussions. In the same way, I thank Prof. Dr. Reinhard Kremer, Dr. Rotraut Merkle, Dr. Manuel Schaloske, Claudia Kamella, and Eva Brücher for the assistance in various characterization measurements and chemical problems. Special thanks to Heiko Uhlig, our electronics specialist and "best boy" for everything. Without him, most of the measurements would not have been possible. Furthermore, I thank our engineers Benjamin Bruha and Manfred Ohl for their technical support, as well as Michael Schulz and Heinrich Klann for their active help during the magnetization measurements. Special thanks to the people from the low temperature service for providing me with liquid helium, even when out of sequence.

I would deeply like to thank all the people who helped me during my time as a PhD student representative. Firstly, I thank my four representatives colleagues for the good teamwork. Many thanks to Prof. Dr. Walter Metzner for his friendly openness and support and Dr. Thomas Wagner for his social feeling and the great teamwork. In the same way, I thank Dr. Michaela Asen-Palmer, Dr. Hans-Georg Libuda, and Mrs. Birgit King. I send special thanks to the workers' council for their colorful support.

Many thanks to all people from the Computer Service Group for keeping my scientific progress running. In particular, I thank André Neubauer for his great help, extending far beyond his work-related duty. In the same way, I thank Dr. Werner Marx for his professional support in the search for suitable literature and the great discussions about photography. Special thanks to our secretary Mrs. Claudia Hagemann for all the uncountable favors, like providing me the spring room in Ringberg, not once, but twice.

Finally, I would like to thank all people from Keimer's department for the high-level educational time and for the possibility to participate in their scientific work. I am thankful for having been a member of this group and for having met so many nice colleagues and friends here at the institute. In particular, I would like to thank my room mates Dr. Mohammed Bakr, Dr. Pegor Aynajian, Nadir Driza, Muhammad Khalid, and Youngje Um for many informative discussions, collegial help, and for a great time together. Special thanks to all members of the coffee club and cake foundation for teaching me the high art of culinary delights. In the same way, I thank all my friends at Tübingen University for staying close to me despite my migration to Stuttgart. Many thanks to Daniel Haug for reading the first version of my thesis and for sharing my joy and sorrow. Thanks to Alex Fraño Pereira for giving me helpful advice in English.

I thank my parents deeply for supporting me during my studies and for convincing me that I am on the right way. In the same way, I thank my parents-in-law for standing beside me and for believing in me. Thousands of thanks to my wife Christin for all the patience and encouragement.